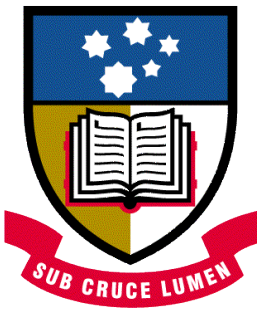

THE UNIVERSITY OF ADELAIDE

School of Electrical and Electronic Engineering

Design of Permanent Magnet Machines for Field-Weakening Operation

Chun Tang

A thesis presented for the degree of Doctor of Philosophy

2015

Dedicated to my parents

THE UNIVERSITY
OF ADELAIDE
AUSTRALIA

Design of Permanent Magnet Machines for Field-Weakening Operation

Chun Tang

Submitted for the degree of Doctor of Philosophy

2015

Abstract

This research focuses on the electromagnetic design of permanent magnet (PM) machines in terms of the iron loss, torque pulsations and field-weakening performance. It covers the investigation of the effect of stator-slot and rotor-pole number combinations for surface-mounted PM (SPM) machines, and the stator-slot and rotor-effective-slot number combinations for interior permanent magnet (IPM) machines.

The effect of changing the number of slots and poles on the performance of a particular SPM machine design is studied in detail using finite element analysis. This includes examining the back-EMF, the open-circuit/full-load power losses, the cogging/ripple torque, and the field-weakening performance. The simulation results are compared with the expected relationships to provide electric machine designers useful insights on the effect of the number of slots and poles on the performance of SPM machines.

Operation at high speed in traction drives corresponds to deep field-weakening conditions. Due to the high electrical frequencies, the iron loss of IPM machines at high speeds can significantly affect the overall efficiency. This thesis investigates the rotor-

cavity positioning and the combination of stator-slot and rotor-effective-slot number on the eddy-current loss for IPM/reluctance machines operating under deep field-weakening conditions. A new closed-form expression for the stator and rotor eddy-current loss is developed. The optimal barrier-positioning for the minimum total loss and the effect on the eddy-current loss of varying the stator-slot and rotor-effective-slot number are investigated for 1-, 2-, 3- and full-layered rotors.

FEM optimisation and experimental verification of an example IPM machine design are presented. An optimized 30 slot, 4 pole (slot/pole/phase = 2.5) three-layered IPM machine with a significantly reduced iron loss under field-weakening operation is proposed and compared to the baseline 36-slot 4-pole (slot/pole/phase = 3) three-layered IPM machine. The detailed comparison of the optimized and baseline designs using a combination of the analytical, FEM and experimental tests are presented.

.

Statement of Originality

This work contains no material which has been accepted for any other degree or diploma in any university or tertiary institution, and to the best of my knowledge and belief, contains no material previously published or written by another person, except where due reference has been made.

I give consent to this copy of the thesis, when deposited in the University Library, being made available for loan and photocopying, subject to the provisions of the copyright act 1968.

I also give permission for the digital version of my thesis to be made available on the web, via the University's digital research repository, the Library catalogue, the Australian Digital Thesis Program (ADTP) and also through web search engines, unless permission has been given by the University to restrict access for a period of time.

Signed: _____

Date: _____June-29-2015_____

List of Publications

[P1] **C. Tang**, W.L. Soong, T. M. Jahns and N. Ertugrul, "Analysis of Iron Loss in Interior PM Machines with Distributed Windings under Deep Field-Weakening", *IEEE Trans. Ind. Appl.*, 2015 (accepted).

[P2] **C. Tang**, W.L. Soong, T. M. Jahns, G.S. Liew and N. Ertugrul, "Analysis of Stator Iron Loss in Interior PM Machines under Open and Short-Circuit Conditions", *IEEE Energy Conversion Congress and Exposition (ECCE)*, 2013, Denver.

[P3] **C. Tang**, W.L. Soong, G.S. Liew and N. Ertugrul, "Modelling of a Bonded Magnet Ring Surface PM Machine using Soft Magnetic Composites", *Int. Conf. on Elect. Machines* (*ICEM*), 2012, France.

[P4] **C. Tang**, W.L. Soong, G.S. Liew and N. Ertugrul, "Effect of Pole and Slot Number Changes on the Performance of a Surface PM Machine", *Int. Conf. on Elect. Machines* (*ICEM*), 2012, France.

[P5] **C. Tang**, W.L. Soong, P. Freere, M. Pathmanathan and N. Ertugrul, "Dynamic Wind Turbine Output Power Reduction under Varying Wind Speed Conditions Due to Inertia", *Wind Energy* 2012; DOI: 10.1002/we.1507.

[P6] G.S. Liew, **C. Tang**, W.L. Soong, N. Ertugrul and D.B. Gehlert, "Finite-Element Analysis and Design of a Radial-Field Brushless PM Machine Utilizing Soft Magnetic Composites", *IEEE Int. Electric Machines and Drives Conf.* (*IEMDC*), 2011, Canada, pp. 930-935.

[P7] M. Pathmanathan, **C. Tang**, W.L. Soong and N. Ertugrul, "Detailed Investigation of Semi-Bridge Switched-Mode Rectifier for Small-Scale Wind Turbine Applications", *IEEE Int. Conf. on Sustainable Energy Technologies* (*ICSET*), 2008, Singapore, pp. 950-955.

[P8] **C. Tang**, M. Pathmanathan, W.L. Soong and N. Ertugrul, "Effects of Inertia on Dynamic Performance of Wind Turbines", *Australasian Universities Power Engineering Conference* (AUPEC), Dec. 2008, Australia.

[P9] M. Pathmanathan, **C. Tang**, W.L. Soong and N. Ertugrul, "Comparison of Power Converters for Small-Scale Wind Turbine Operation", *Australasian Universities Power Engineering Conference* (AUPEC), Dec. 2008, Australia.

Acknowledgements

I would like to thank my supervisor, Prof. Wen L. Soong for all his generous support and expert guidance over all these years both at the professional and personal level. I am also grateful for the help and assistance provided by my co-supervisors, Prof. Nesimi Ertugrul, Dr. Gene Liew and Dr. Peter Freere. I express gratitude towards the University of Adelaide and the Australian Research Council for supporting my studies through the Australian Research Council Discovery grant, DP0988255. I would sincerely like to thank the staff of the Electrical Engineering Workshop for all the time they invested in aiding my projects.

I would also like to thank Prof. Thomas M. Jahns from University of Wisconsin-Madison, for his insightful technical discussions and generous help during the period of my stay in Madison.

Finally, I would like to thank my family for the invaluable support and patience during this journey.

Table of Contents

List of Figures

List of Tables

Nomenclature

θ	Stator circumferential coordinates	elec. deg
ω_e	Synchronous angular frequency	rad/s
μ_o	Magnetic permeability of vacuum	H/m
α_j	rotor cavity angular position	elec. deg
Δ_s	Stator tooth pitch angle	elec. deg
Δ_r	Rotor channel pitch angle	elec. deg
ξ_j	Rotor channel circumferential position	elec. deg
δ	Angle between the cavity and *d*-axis	mech. deg
Ψ_m	Magnet flux linkage	Wb
Ψ_d	Stator *d*-axis flux linkage	Wb
Ψ_q	Stator *q*-axis flux linkage	Wb
Φ_{rem}	Magnet remanent flux	Wb
Φ_{lk}	Rotor-rib leakage flux	Wb
B_g	Radial airgap flux density	T
B_{gm}	Magnet created airgap flux density	T
B_{gr}	Rotor-MMF contributed airgap flux density	T
B_r	Magnet remanent flux density	T

B_t	Stator-teeth flux density	T
B_y	Stator-yoke flux density	T
B_{chl}	Rotor-channel tunnelling flux density	T
E_{ph}	Phase back-EMF voltage	V_{rms}
f_1	Synchronous frequency	Hz
f_s	Stator MMF	At
f_{sh}	Stator MMF spatial harmonics	At
f_r	Rotor MMF	At
f_{rn}	Rotor MMF spatial harmonics	At
g_e	Effective airgap length	m
h	Stator MMF spatial harmonic order	
I_m	*S*tator peak phase current	A_{pk}
I_d	Stator *d*-axis current	A_{rms}
I_q	Stator *q*-axis current	A_{rms}
I_{ch}	Characteristic current	A_{rms}
I_{sc}	Stator short-circuit current	A_{rms}
k_{sh}	Stator winding factors	
k_{w1}	Synchronous winding factor	
k_{d1}	Synchronous winding distribution factor	
k_{p1}	Synchronous winding pitch factor	
k_t	Stator tooth-pitch-at-airgap to body-width ratio	
k_y	Pole-pitch-at-airgap to stator-yoke-thickness ratio	
k_{chl}	Rotor channel pitch-at-airgap to width ratio	
k_e	Eddy-current loss coefficient	W/m^3
l_{stk}	Lamination stack length	m
l_{teeth}	Stator-teeth radial length	m
l_{chl}	Rotor-channel mean length	m
L_d	*d*-axis inductance	H
L_q	*q*-axis inductance	H
L_{end}	Stator end-winding inductance	H
n	Rotor MMF spatial harmonic order	
n_s	Number of stator slot per pole-pair	

n_r	Number of rotor slot per pole-pair	
N_t	Number of series turns per phase	
p	Number of pole-pairs	
P	Number of poles	
p_{eddy}	Eddy-current loss density	W/m^3
p_{teeth}	Stator-teeth eddy-current loss density	W/m^3
p_{yoke}	Stator-yoke eddy-current loss density	W/m^3
p_{chl}	Rotor channel eddy-current loss density	W/m^3
r_g	Average airgap radius	m
r_j	Rotor channel magnetic potential	At
R_s	Stator phase resistance	ohms
R_b	Rotor barrier magnetic reluctance	H^{-1}
R_g	Sectional airgap magnetic reluctance	H^{-1}
R_{yoke}	Stator-yoke average radius	m
R_{teeth}	Stator-teeth average radius	m
R_{rot}	Rotor outer radius	m
S	Stator slot number	
T_{ave}	Total average torque	Nm
T_{mag}	Magnet torque	Nm
T_{rel}	Reluctance torque	Nm
V_{ph}	Stator phase voltage	V_{rms}
V_{yoke}	Stator-yoke volume	m^3
V_{teeth}	Stator-teeth volume	m^3
V_{chl}	Rotor-channel volume	m^3
w_{chl}	Rotor-channel mean width	m
w_c	Cavity thickness	m
X_d	*d*-axis reactance	ohms
X_q	*q*-axis reactance	ohms

Acronyms

CPSR	Constant Power Speed Ratio
EMF	Electric-Motive Force
FEM	Finite-Element Method
FW	Field-Weakening
IPM	Interior Permanent Magnet
MMF	Magneto-Motive Force
MTPA	Maximum Torque per Ampere
PM	Permanent Magnet
SPM	Surface Permanent Magnet
SPP	Slots/Pole/Phase
THD	Total Harmonic Distortion

Chapter 1. Introduction

1.1. Background and Motivation

Permanent magnet synchronous machines are increasingly attractive in various implementations recently, including low-speed applications such as large wind generators (~20-500rpm) and high-speed applications such as electric vehicle traction (~10,000rpm).

Unlike the traditional wound-field synchronous machines with the DC excitation coils in the rotor, the PM machines use rotor permanent magnets for the excitation. Permanent magnet (PM) synchronous machines have the capability of excellent electromagnetic characteristics, such as high efficiency, high torque density and power factor.

1.2. Typical Structures of PM Synchronous Machines

Similar to traditional synchronous machines, the stator of synchronous PM machines has a multiphase AC winding, usually three phases. The rotor of PM machines consists of the permanent magnet, back-iron and shaft. The typical rotor structures include the surface-mounted PM (SPM) machines and interior PM (IPM) machines.

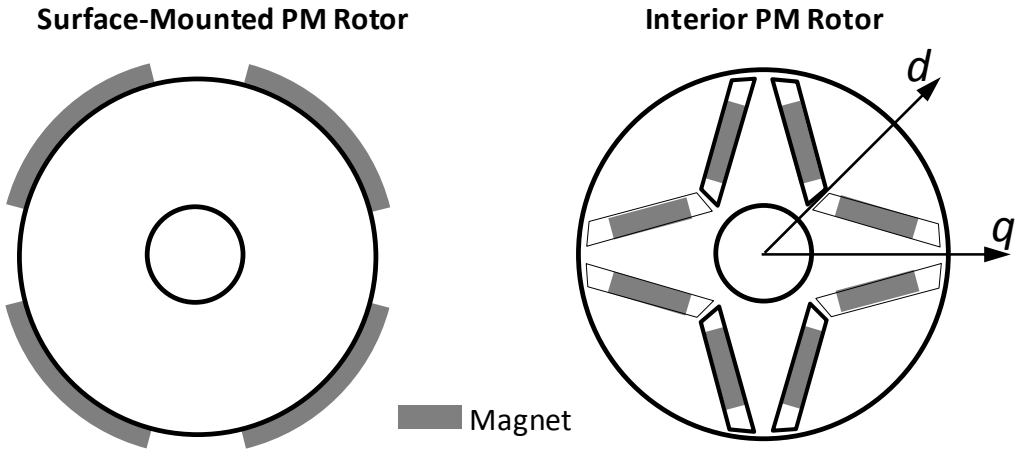

Figure 1-1: Example surface-mounted PM and interior PM rotor

As shown in Figure 1-1, in SPM machines the magnet is mounted on the surface of the rotor iron while in IPM machines the magnet is buried inside the rotor iron. As the barriers increase the rotor anisotropy, the IPM machines have different electromagnetic induction in direct (*d*) axis and quadrature (*q*) axis while the SPM machines have the same induction.

1.3. General Electromagnetic Performance Evaluations

The general electromagnetic evaluations of the PM machines contain the power losses, electromagnetic torque, field-weakening performance for high-speed operation and power factor.

1.3.1. Power Loss and Efficiency

The power loss of a rotating machine during the energy convension process includes two categories: mechanical losses and electrical losses. The mechanical loss primarily includes

the friction loss and windage loss. The electrical loss include the stator and rotor iron loss, the magnet eddy-current loss and the stator-winding copper loss. High electrical loss will reduce overall efficiency and increase the challenge of cooling the PM machines [1], [5]-[19], [23], [28]-[33], [45].

The iron loss which includes the hysteresis and eddy-current loss is frequency dependent so that it increases with the rotational speed. The copper loss is current dependent, which can be seen as constant when the current stays unchanged from low to high speed, if skin-effect issues are ignored. The copper loss dominates the iron loss at low speed while the iron loss can be increasingly larger than the copper loss at high speed.

1.3.2. Electromagnetic Torque

The interaction of the magnetic field and the stator current produces the electromagnetic torque. The electromagnetic torque includes two terms: average torque and ripple torque [36]. The average torque is the average value of the electromagnetic torque while the ripple torque is its variation with time.

The average torque for IPM machines includes two terms: reluctance torque and magnet torque, while SPM machines only have the magnet torque term. The reluctance torque resulted by the different electromagnetic induction of *dq*-axis can reduce the usage of permanent magnet for IPM machines. High torque density, i.e. the average torque produced by per unit volume, is of interest in most occasions [55]. This reduces the machine's size and weight and may reduce the machines' manufacturing cost. On the other hand, a machine with same volume can generate higher acceleration torque.

Ripple torque and acoustic noise are critical in some applications, such as electric vehicle traction [27], [35]. The ripple torque is described as the variation of magnetic coenergy during the rotor rotation [36], which can be sourced from the alignment between the rotor magnet and stator teeth (also called cogging torque), the interaction of the harmonics between the stator magnetomotive force and the reaction of a reluctance rotor, and the interaction of the harmonics between the stator magnetomotive force and the rotor magnet flux [48]-[54].

1.3.3. Field-Weakening Performance

In order to maintain the terminal voltage under the inverter voltage limit, the stator current is controlled to produce an opposing *d*-axis flux to reduce the magnet flux at high speed, which is called field-weakening. The speed range and maximum power capability are important factors for evaluations for the machines' field-weakening performance [41][42]. Maintaining a high output power over a wide speed range is critical for high-speed applications, such as electric vehicle traction [43], [44].

1.3.4. Power-Factor

High power factor is important to reduce the requested apparent power capability of the converter/inverter [43]. A high power factor can be achieved by either increasing the rotor anisotropy or the magnet flux linkage [42].

1.4. Thesis Overview

1.4.1. Research Gap

A detailed description of the prior literature is presented in each chapter. A general summary of the research gaps are given as follows,

- Though there are general guidelines for choosing the stator-slot and rotor-pole number, there is scope for more detailed case studies with the aim of showing how the general performance trade-offs apply to a practical machine design when the numbers of slots and poles are varied over a wide range.
- Presently there are no closed-form analytical expressions to quickly estimate the eddy-current loss for IPM/reluctance machines in the literature. The impact of stator-slot and rotor-effective-slot number for unevenly displaced cavities and for various numbers of rotor-cavity layers on the total eddy-current loss has not been presented yet.
- Experimental comparisons of iron loss using IPM machines with various combinations of stator-slot and rotor-effective-slot number have not been seen in the literature.

1.4.2. Original Contributions

The major research contributions of the thesis are summarised below,

- The effect of using different slot-pole combinations is studied in detail by FEM for a particular surface PM design to help machine designers gain physical insights into the effect on losses, torque ripple and field-weakening performance.
- A novel closed-form formulation is presented for calculating the stator and rotor eddy-current loss for various numbers of layers of rotor cavities for IPM/reluctance machines operating under deep field-weakening conditions.
- The optimal circumferential positions of rotor cavities to minimize total eddy-current loss for 1-, 2- and 3-layered rotors is explored for IPM/reluctance machines.
- The effect of broad changes in the stator-slot and rotor-effective-slot number on the total eddy-current loss is investigated for IPM/reluctance machines.
- The impact of changing the number of rotor-cavity layers on the total eddy-current loss is presented for IPM/reluctance machines.
- Experimental tests are conducted on four machines to obtain the iron loss under open-circuit and short-circuit conditions. These results are compared with the calculated iron loss by the FEM models and analytical expressions.

1.4.3. Thesis Outline

The outline of the thesis is as follows:

Chapter 2 presents a study on the effect of stator-slot and rotor-pole number variations on the SPM machines' performance in terms of power losses and efficiency, ripple torque and field-weakening performance.

Chapter 3 proposes closed-form analytical expressions of iron loss for IPM/reluctance machines under field-weakening conditions. The same chapter also presents the impact of stator-slot and rotor-effective-slot number for unevenly displaced cavities and for various numbers of rotor-cavity layers by using the proposed analytical iron loss expressions. The filtering effect of the stator-tooth pitch and rotor-channel pitch on airgap flux density is described in Appendix A.

Chapter 4 presents the FEM optimization of a baseline ns18nr12 IPM machine design. An optimized ns18nr18 IPM machine design with 30% lower deep-field-weakening iron loss and 40% lower ripple torque is proposed. The *dq*-axis flux linkage,

back-emf and resistance of the prototype machines were experimentally measured to predict their performance. The stator-tooth flux density and iron loss measured in the open-circuit and short-circuit test are used to verify the calculated results from the FEM and analytical expressions.

Chapter 5 summarises the major results and findings for the thesis. The suggestions for future research work are also included.

Chapter 2. Effect of Pole and Slot Number on Performance of SPM Machines

Permanent magnet (PM) machines are becoming more widely used due to their high power density and efficiency. An important machine design parameter is the number of stator slots per pole per phase (*SPP*).

Traditionally surface PM machines used distributed windings, which have values of *SPP* of unity or larger. A unity value of *SPP* offers a high winding factor to minimize stator copper losses, while higher values of *SPP* produce a more sinusoidal stator mmf distribution which minimizes rotor losses [1].

In recent years there has been considerable interest in the use of concentrated windings for surface PM machines [2]-[20]. These have values of *SPP* less than unity. Concentrated windings have shorter end-windings and hence lower stator copper loss, produce lower cogging torque, offer manufacturing advantages such as allowing a segmented stator, and have higher leakage inductance which allows a wider field-weakening speed range [2]-[4]. A significant challenge with concentrated windings is the large low-order harmonics in the stator mmf distribution, particularly for single-layer designs, which can produce high losses in the rotor magnets and back-iron [5]-[13].

For inverter-driven PM machines there is considerable freedom to select the number of poles for a given operating speed. Increasing the number of poles reduces the length of the stator end-windings and hence the copper loss, while at the same time increasing the stator frequency and hence the stator iron losses. There is thus an optimum number of poles for maximum efficiency under rated conditions [1].

For the same stator diameter, optimized concentrated winding machine designs generally have more poles and fewer slots than distributed winding machines. There has been a number of papers discussing the selection of the numbers of slots and poles for concentrated winding machines. Considerations include: a high fundamental winding factor to minimize the copper losses; a high least-common-multiple of the number of slots and poles to reduce the cogging torque, and a high even value of the greatest-common-divisor of the number of slots and poles to reduce the unbalanced radial force [21]. The optimal slot-pole combinations proposed in the previous literature include: $S = P \pm 2$ [14], [15],[18], $S = P \pm 1$ [16] and $1/3 < SPP < 1/2$ [17], where S and P are the slot and pole numbers respectively.

Though the above methods and other general guidelines [22] are helpful for selecting the stator slot-pole combination, there is scope for more detailed case studies with the aim of showing how the general performance trade-offs apply to a practical machine design when the numbers of slots and poles are varied over a wide range.

This chapter uses 2-D finite-element analysis to examine eleven different slot and pole variations for a given machine design to provide more detailed insights into the effect of the changes on the machine performance. Comparisons are presented between previously published predictions and the finite-element analysis results for parameters such as stator tooth and yoke losses [1], [23]; cogging torque [20], rotor losses and the effect of segmentation [5]-[7]; and field-weakening performance [2], [6].

2.1. Baseline Design and Analysis Approach

2.1.1. 2-D Finite-Element Method to Solve Magnetic Problems

A rotating permanent magnet (PM) machine generally consists of a number of parts, including stator iron, stator winding, rotor magnet and rotor iron etc. Each part of the machine corresponds to an electromagnetic domain. These domains are then subdivided

into a finite number of small elements, a triangular-shape normally, in the finite-element method (FEM). The magnetic quantities, such as magnetic flux density **B**, magnetic field strength **H** etc. are solved for each apex of these triangular elements based on Maxwell's equations. FEM has been shown to be an accurate way to analyse magnetic problems and is widely used in electric machine design.

Electric machines with laminated cores are normally treated as effectively 2-dimensional (2-D) in FEM analysis. The fringing magnetic effect at the two axial ends is normally neglected as it is usually small. Therefore, 2-D FEM can be applied by only solving the machine's cross-section in *x-y* plane which is perpendicular to the rotation centre. This can substantially reduce execution time in comparison to solving an entire 3-D FEM model but have similar results. Only the 2-D FEM is used to produce the finite-element results in this thesis.

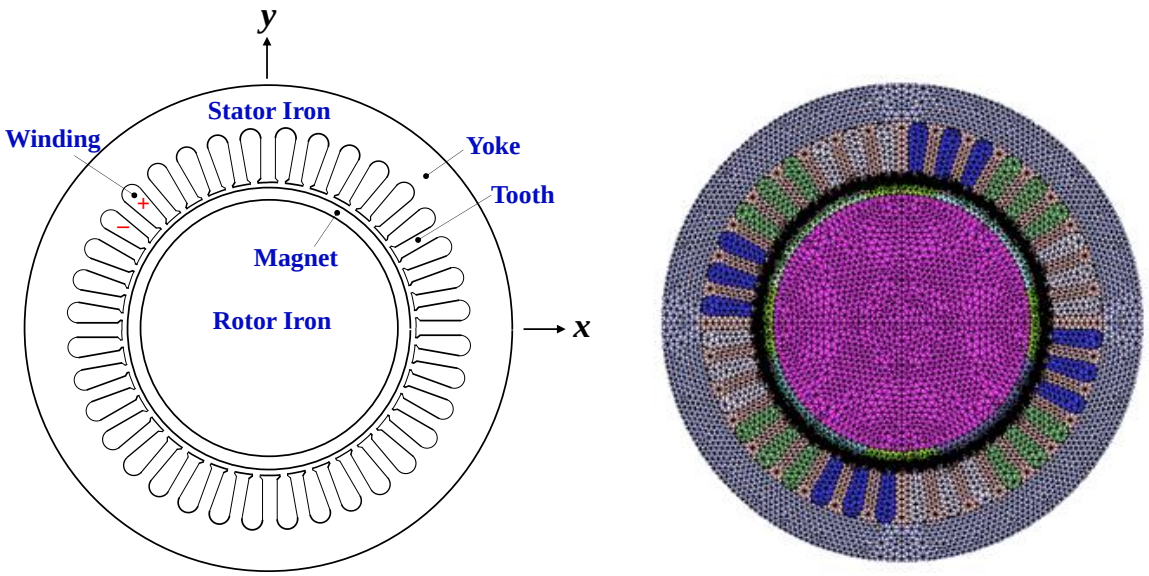

Figure 2-1: Sketch (left) and mesh (right) of cross-section in *x-y* plane for an example PM machine

2.1.2. Base-Line Machine and Analysis Methodology

The baseline surface PM machine uses the stator from a small commercial 4-pole induction motor which was rated at 2.2 kW at 1,415 rpm, corresponding to a rated torque of about 15 Nm. The design of the 36-slot stator was left unchanged, while the induction machine rotor was replaced with a surface PM design using sintered rare-earth magnets, and the airgap

increased from 0.4 mm to 1.5 mm to allow room for mechanically holding the magnets. The machine cross-section is shown in Figure 2-2 and its parameters are listed in Table 2-1.

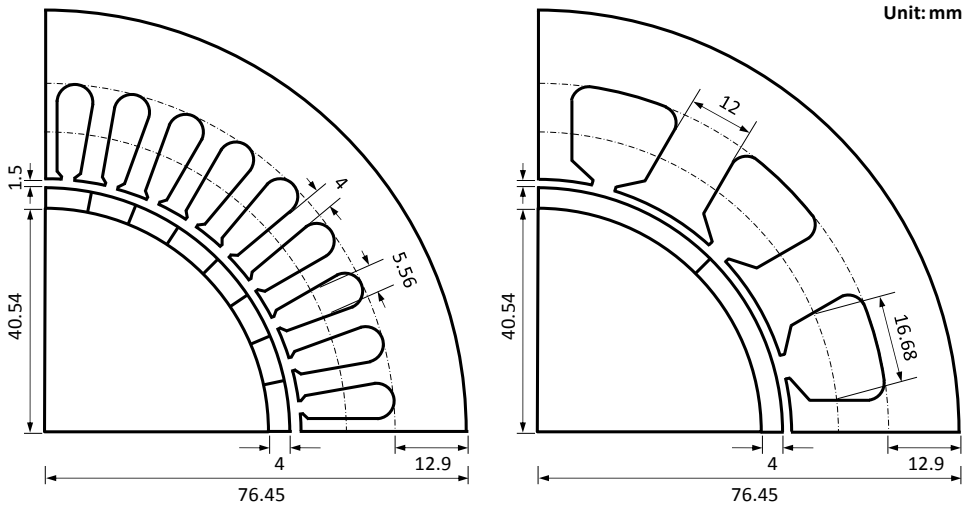

Figure 2-2: Cross-sections for the 36- and 12-slot stators

Table 2-1: Key Parameters and Dimensions of the SPM Machines

Stator Outer Diameter	152.9 mm
Stator Inner Diameter	92.08 mm
Stack Length	95 mm
Number of Stator Slots	36, 12
Air gap Length	1.5 mm
Magnet type	NdFeB (sintered)
Remanent Flux Density	1.1 T
Magnet Thickness	4 mm
Magnet Resistivity	$1.5 \times 10^{-6} \Omega m$
Magnet Pole-Arc	180° electrical
Rotor Back-Iron Resistivity	$2.22 \times 10^{-7} \Omega m$

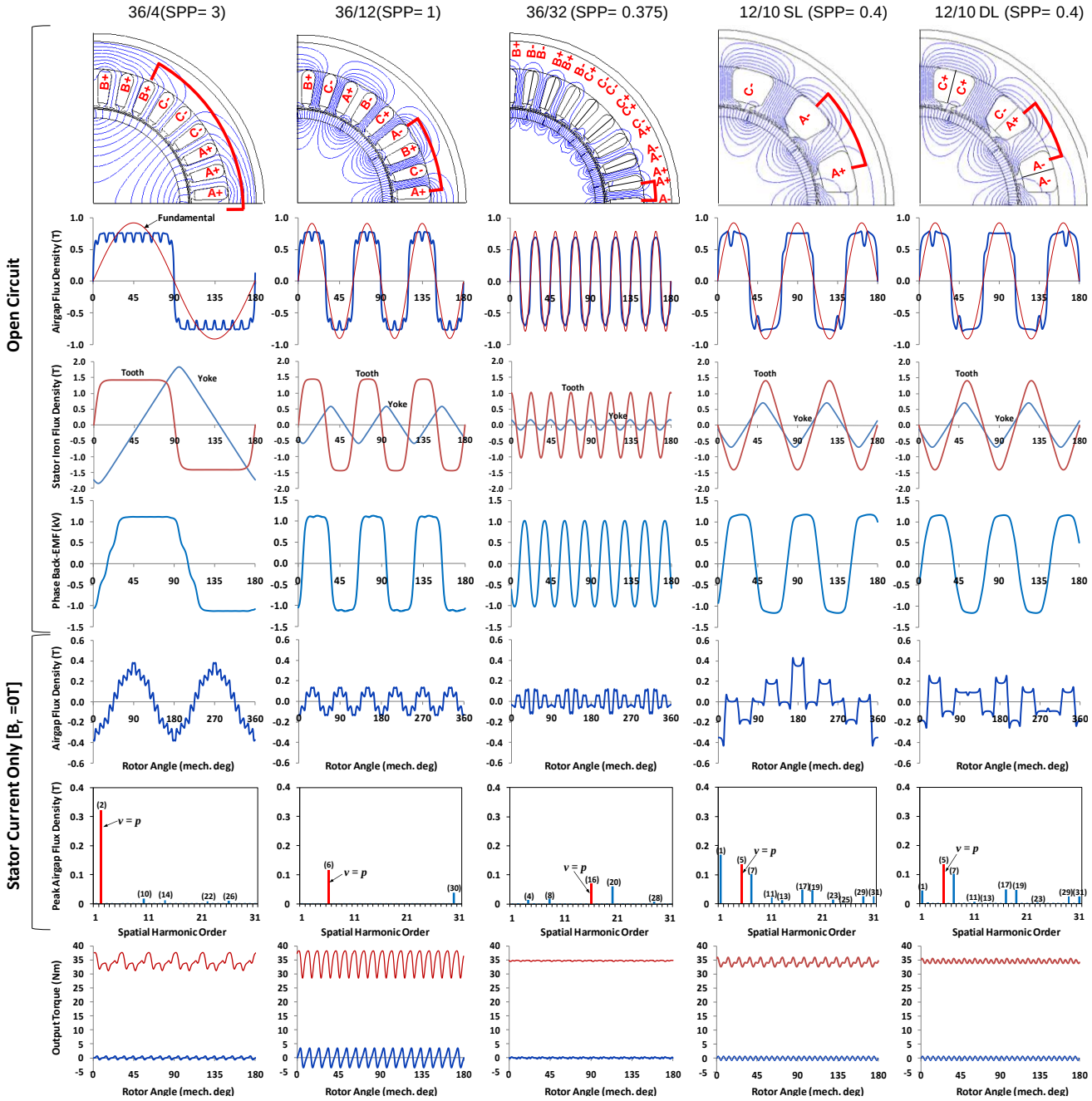

Figure 2-3: FE open-circuit flux line plot, spatial airgap flux distribution, stator tooth/yoke flux density waveform and back-EMF at 6,000rpm (rows 1-4), the airgap flux distribution due to stator current and its spatial harmonic spectrum (rows 5 and 6) and the cogging torque and torque ripple waveforms (row 7) for five of the machine designs

The effect of changing to a 12-slot stator was also considered. This had the same inner and outer dimensions and same total stator slot area as the original 36-slot stator but with stator teeth which are three times wider (see Figure 2-2). The assumed stator winding arrangements are shown in the top row of Figure 2-3.

The effect of varying the number of poles was examined. For the 36-slot stator, 4, 6, 12, 24 and 32 pole designs were examined using the same stator lamination. For the 12-slot stator, 4, 8, 10 and 14 pole designs were considered with both single- and double-layer designs for the fractional-slot 10 and 14 pole designs. There were thus a total of eleven machine designs which were examined. Note that the thickness of stator yoke could have been reduced as the pole number increased, however for simplicity this was kept constant.

A rated output power point of 22 kW at 6,000 rpm (rated torque of 35 Nm) was chosen for the surface PM machine as being more realistic for a high-performance drive application. This corresponds to a moderate shear stress of about 28 kPa (about 4 psi). To obtain a reasonable efficiency at this speed, a low-loss 0.5 mm thick lamination steel was used in the simulations (50JN290 with a loss density of 2.9W/kg at 1.5T/50Hz). The number of series turns per phase and stack length was kept constant.

A comprehensive series of 2-D finite-element simulations was performed for the eleven machine designs. Figure 2-3 shows example finite-element results for five of these designs: the 36-slot 4 pole, 12 pole and 32 pole designs, and the 12-slot 10 pole single- and double-layer designs. The first four rows show open-circuit results including a flux line plot, airgap flux density, stator tooth/yoke flux density and phase back-EMF waveform. These will be discussed in the analysis of stator iron and copper losses in Section 2.2. The next two rows show the airgap flux density due to the stator current and its spatial harmonic spectrum. These strongly affect the rotor losses and will be discussed in the analysis of the full-load losses in Section 2.3.

Finally the last row shows the cogging torque and torque ripple at rated output torque, which is described in Sections 2.2.3 and 2.3.3 respectively.

This chapter also includes in Section 2.4 a discussion of the field-weakening performance of the machine designs, an aspect which is important for traction applications.

2.2. Open-Circuit Parameters

This section examines the open-circuit parameters of the machine designs including: the back-EMF (and its effect on the full-load copper loss), the open-circuit iron loss, and the cogging torque.

2.2.1. Back-EMF

A surface permanent magnet (SPM) machine produces only the magnet torque, this is proportional to the back-EMF. For a constant value of rated torque, a lower back-EMF corresponds to higher required stator current and hence copper loss. The back-EMF is directly proportional to the product of the fundamental airgap flux density and the stator winding factor.

The spatial magnet airgap flux density waveforms are shown in row 2 of Figure 2-3. Due to the 180° magnet pole-arc, the airgap flux is ideally rectangular and the simulated results closely approximate this for low pole numbers e.g. 4 poles. As the number of poles increase, magnet fringing effects become more significant [23] and the airgap and tooth flux density become more sinusoidal, reducing their fundamental values.

The fundamental stator winding factor k_{w1} is a measure of how well the winding couples with the fundamental airgap magnetic flux. The winding factor is the product of the distribution factor k_{d1}, accounting for the phase differences between the back-EMF waveforms of series-connected coils, and the pitch factor k_{p1}, accounting for differences between the coil and the pole pitch.

$$k_{w1} = k_{d1} \cdot k_{p1} \tag{2-1}$$

The winding factors are a function of the number of slots per pole per phase (*SPP*). As discussed earlier, *SPP* values of 1 and above correspond to distributed windings while lower values correspond to concentrated windings. Table 2-2 shows the winding factor for the eleven machines classified by the seven unique values of *SPP*. Note for both *SPP* = 1 and 0.5, two of the designs have the same *SPP* value and hence winding factors. Also the single (S) and double (D)-layer designs have the same *SPP* but different winding factors.

Table 2-2: Fundamental Winding Factor k_{w1}

SPP	3	2	1	1/2	2/5		3/8	2/7	
Distributed Windings				Concentrated Windings					
36s	4p	6p	12p	24p			32p		
12s			4p	8p	10p-S	10p-D		14p-S	14p-D
k_{d1}	0.960	0.966	1	1	1	0.966	0.960	1	0.966
k_{p1}	1	1	1	0.866	0.966	0.966	0.985	0.966	0.966
k_{w1}	0.960	0.966	1	0.866	0.966	0.933	0.945	0.966	0.933

Figure 2-4 illustrates how the calculated back-EMF of the eleven machines is related to the product of the calculated peak fundamental airgap flux density and the analytical winding factor. It also shows the calculated rated current which is required to produce rated torque, this is inversely proportional to the back-EMF. Note that the back-EMF of the 24 and 32-pole, 36-slot machines are particularly low which results in higher values of rated current.

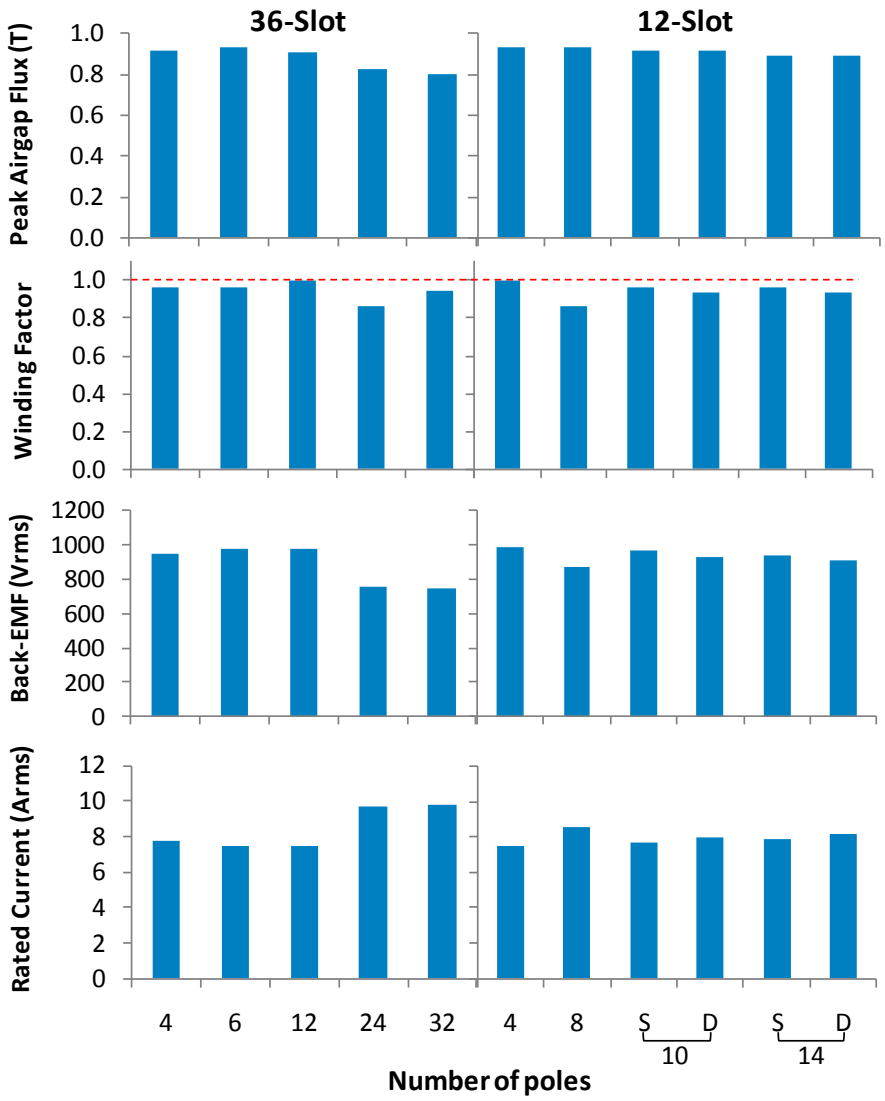

Figure 2-4: Calculated peak fundamental airgap flux density, analytical winding factor, calculated phase fundamental back-EMF at 6,000rpm and rated current for the 36- and 12-slot SPM machines

Though open-circuit quantities are being examined in this section, the copper losses at rated torque will now be considered as these are directly related to the back-EMF magnitude.

Figure 2-5 shows the calculated copper losses at rated torque which are obtained from the estimated mean length per turn for the stator winding and the rated current. The copper losses are divided into the slot and end-winding copper loss. The stator slot copper loss is only affected by the rated current. The end-winding copper loss drops inversely with the number of poles. Double-layer concentrated windings have lower end-winding copper losses than single-layer windings due to their shorter mean end-turn length.

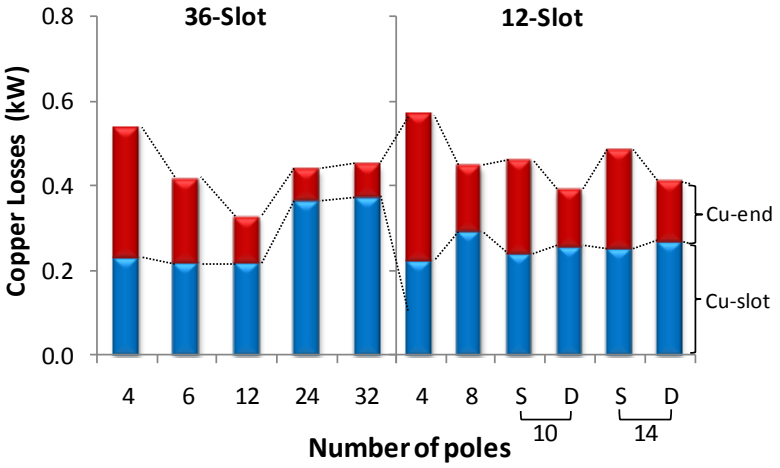

Figure 2-5: Calculated stator-slot and end-winding copper loss at rated torque (35 Nm).

In general, with low numbers of poles, the end-winding length and hence copper loss is large, while with high numbers of poles, the back-EMF is lower and hence the slot copper losses are larger. The minimum calculated total stator copper loss at rated torque is obtained with the 36-slot 12-pole design (which has *SPP* = 1 and hence unity winding factor) with the second lowest being the 12-slot 10-pole double-layer design.

2.2.2. Open-Circuit Losses

Under open-circuit conditions, the primary loss in the machines is due to stator iron losses in the teeth and yoke as shown in Figure 2-6. The open-circuit rotor losses in the rotor iron and magnets due to the stator slotting are relatively small if the rotor is laminated and the magnets are segmented (discussed in following section). Figure 2-6 shows the calculated loss breakdown at 6,000 rpm.

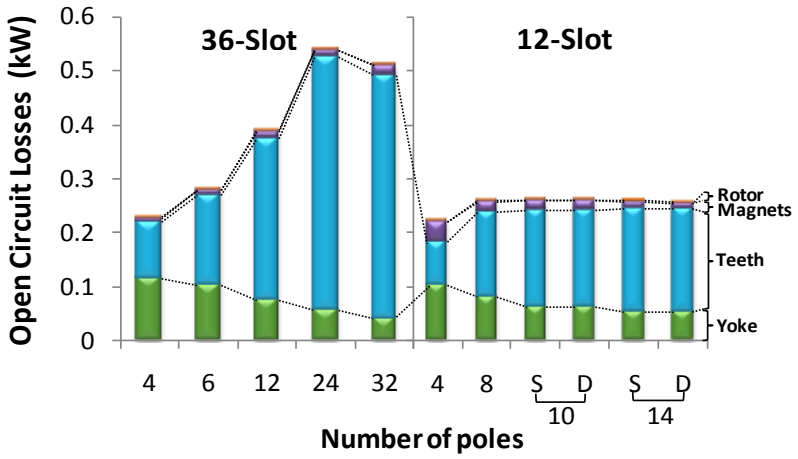

Figure 2-6: Calculated open-circuit loss for the machine designs at 6,000 rpm. A laminated rotor and segmented magnets are assumed

The calculated stator yoke and tooth flux density waveforms are shown in row 3 of Figure 2-3. The stator tooth flux waveforms can be obtained by taking a moving average of the airgap flux density waveform over one stator slot pitch. This "filtering" effect is more pronounced with the 12-slot stator due to its wider stator slot pitch.

Assuming sinusoidal flux densities and only eddy-current loss, the stator tooth losses at 6,000 rpm would be expected to ideally increase with the square of the number of poles (and hence frequency) for a constant tooth flux density. Given that the stator yoke thickness is assumed fixed, then the stator yoke losses should ideally be constant, as the yoke flux density should be inversely proportional to the number of poles.

Figure 2-6 shows that for the 36-slot machine, starting from the 4-pole design, increasing the number of poles to 6 and then 12, results in an increase in stator tooth iron losses which appear to be proportional to number of poles rather than the square of the number of poles as ideally predicted. This is likely due to the reduction of both the peak fundamental value and the harmonic content of the stator tooth flux waveform (see Figure 2-3, row 3).

Ref. [23] analyses this effect by examining the rate of change of flux density with time and shows that the stator tooth iron losses should be proportional to the product of the number of poles and the number of slots for distributed winding machines.

For the 12-slot designs, the tooth losses roughly double between the 4 and 8 pole designs, but the increase for the 10 and 14 pole concentrated winding designs is small. As

predicted by [23], the tooth losses are also generally smaller for the 36-slot design with a comparable number of poles.

Figure 2-3 shows that the yoke flux density waveform approximates a triangle-wave with a relatively constant maximum slope despite changes in the number of poles. This implies that the stator yoke losses should be relatively constant which matches the analytical predictions.

In practice, Figure 2-6 show that the yoke losses fall slowly when the number of poles is increased. This is likely to be due to the stator yoke flux density falling faster than inversely with poles due to fringing effects and also due to the reduction in harmonics.

Overall, as would be expected, the total open-circuit loss for the 36-slot design is lowest for the 4-pole machine and increases significantly with the number of poles. For the 12-slot designs the total open-circuit losses are relatively constant and slightly less than the 36-slot 6-pole machine losses.

2.2.3. Cogging Torque

Cogging torque is caused by the alignment of the edges of the stator teeth and the magnet poles. The frequency of the cogging torque is proportional to the least common multiple of the slots and poles, $LCM(S, 2p)$. It is generally expected that the cogging torque amplitude is inversely proportional to its frequency and hence the $LCM(S, 2p)$. In [20], an index $2p \cdot S/LCM(S, 2p)$, was proposed to predict the cogging torque amplitude changes with the slot and pole number. Figure 2-7 compares the above two cogging torque indices based on the *LCM* and the calculated peak cogging torque. Note that the ability of the indices to predict the trends in the cogging torque results rather than their absolute values is what is important.

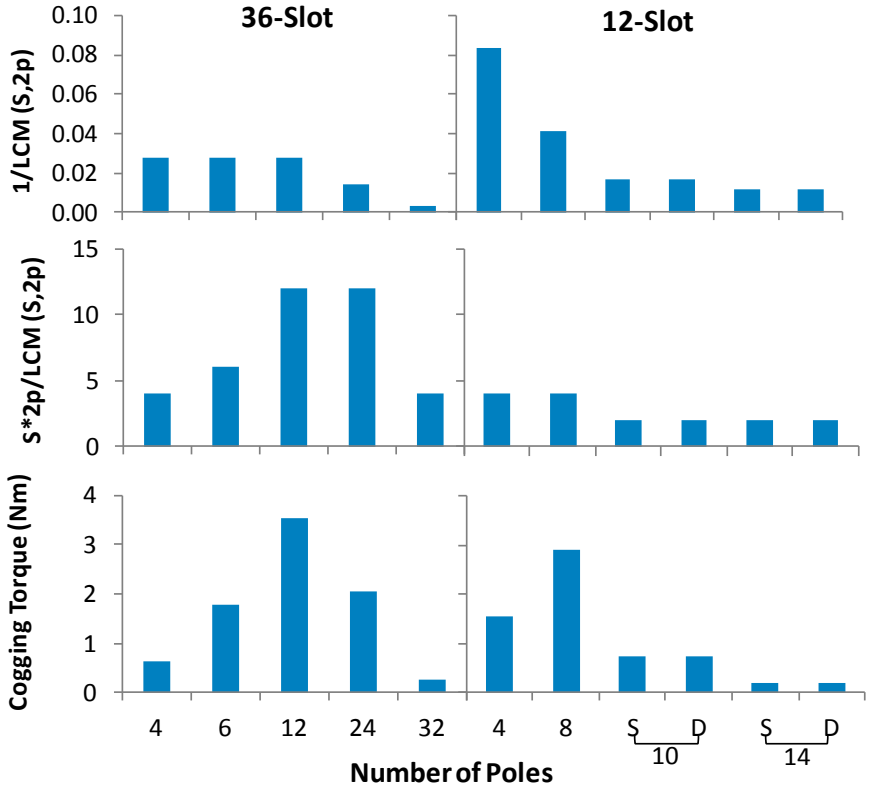

Figure 2-7: Two cogging torque indices based to the least common multiple of the number of slots and poles, and the calculated peak cogging torque for the 36- and 12-slot machines

For the machines with distributed windings, e.g. the 36-slot machine with 4, 6 and 12 poles, the *LCM* values are the same but the number of aligned edges between the stator teeth and magnets and hence the cogging torque is proportional to the number of poles.

The concentrated windings have a fractional *SPP* which results in a low alignment between the stator teeth and the magnet poles and hence lower cogging torque. For these designs the cogging torque is roughly inversely proportional to $LCM(S, 2p)$.

When comparing the cogging torque of machines with the same integral value of *SPP*, e.g. the 36-slot, 12-pole and the 12-slot, 4-pole machines which both have $SPP = 1$, it was found that the cogging torque increased roughly proportional to the number of slots as expected.

The empirical factor $2p \cdot S/LCM(S, 2p)$ introduced in [20] is able to generally predict the trends seen for the 36-slot machine but does not do so well for the 12-slot machine.

2.3. Full-Load Performance

This section examines the performance of the machines at rated current at 6,000 rpm. Rated current is that which is required to produce an output torque of 35Nm assuming the current is sinusoidal and controlled in phase with back-EMF to give maximum torque per ampere operation.

2.3.1. Rotor Iron and Magnet Losses at Rated Current

In this first subsection, the magnet remanent flux density B_r is set to zero to investigate the rotor magnet and iron losses due to the stator current.

When excited by three-phase balanced, sinusoidal currents, the stator windings should ideally produce a sinusoidally-distributed airgap magnetic field which rotates at synchronous speed. In such a case, the rotor sees a constant magnetic field and there should be no rotor losses.

Row 5 of Figure 2-3 shows the calculated airgap spatial flux waveform with rated stator current in the machine and no magnets. Row 6 shows the corresponding frequency spectrum with the fundamental component highlighted.

Distributed winding machines generate a reasonable approximation to a sinusoidal airgap flux density with a strong fundamental component with small harmonics. On the other hand, concentrated winding machines can have significant amplitude harmonics which can be comparable or even exceed the amplitude of the fundamental [5], [6], [45]. These harmonics induce currents into the conductive rotor magnets and back-iron producing eddy-current losses. Note for concentrated winding machines some harmonics can be of lower frequency than the fundamental (sub-harmonics).

According to reference [5], the $SPP = 0.5$ designs (e.g. 36-slot 24-pole and 12-slot 8-pole) are expected to have the lowest rotor loss among all the double-layer concentrated winding configurations; and the $SPP \leq 0.33$ (e.g. 12-slot 10-pole and 14-pole single-layer designs) are expected to have the minimum rotor loss amongst the single-layer concentrated winding designs.

Figure 2-8 illustrates two proposed analytical indices to predict the relative rotor loss. The first index is based on the sum of squares of the harmonic flux density amplitudes.

The second index is based on the sum of the square of the products of the harmonic flux density amplitude and the effective frequency of the currents induced in the rotor.

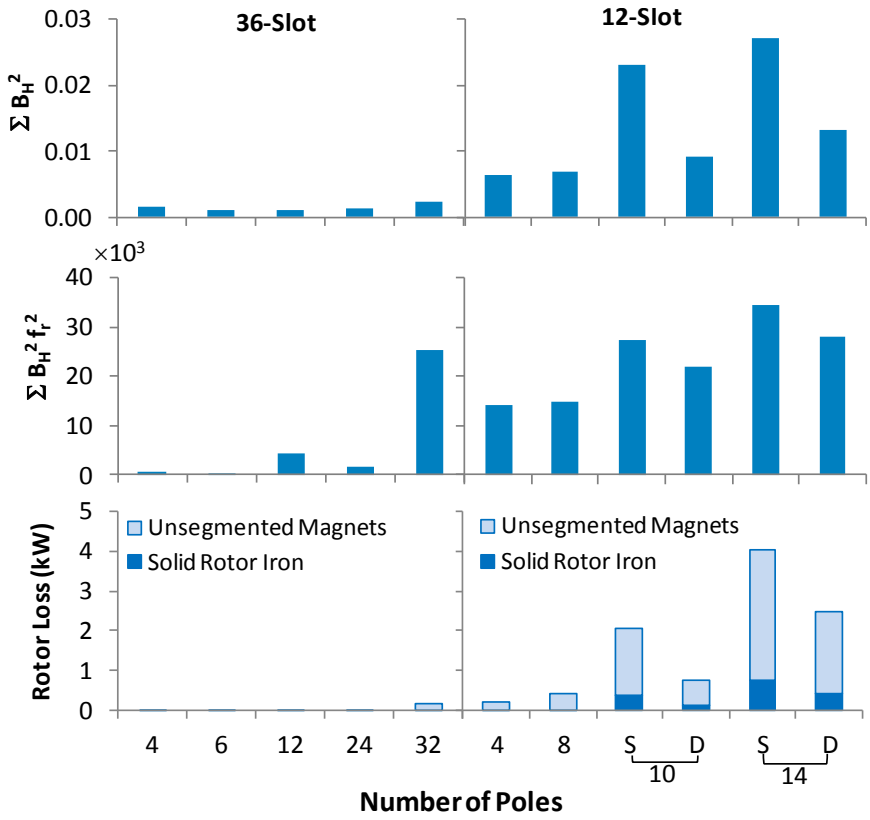

Figure 2-8: Two proposed rotor loss indices and the calculated solid rotor and un-segmented magnet power losses for 36- and 12-slot machines

Figure 2-8 also shows the calculated magnet and rotor loss assuming the rotor magnets form a solid conductive ring and the rotor back-iron is solid. Firstly it can be seen that the rotor losses, particularly the magnet losses, can be very high (compared to the rated output power of 22 kW) for the 12-slot fractional-slot designs. On the other hand the lowest rotor losses are obtained with the 36-slot distributed-winding designs. This result is not surprising based on the stator airgap flux density harmonic spectra in Figure 2-3.

In Figure 2-8, comparing the relative trends of the two rotor loss indices with the FEM calculated rotor loss, it appears that the first index (sum of squares of harmonic amplitudes) is a better match to the calculated results, especially when the number of stator slots was changed. This is somewhat surprising as the second index is a closer match to eddy-current loss theory.

The standard solutions to reducing the rotor losses is to segment the rotor magnets (or use bonded magnets), and to use a laminated rotor back-iron. Segmenting the rotor

magnets reduces the induced voltage in each magnet and increases the eddy-current path length and thus reduces eddy-current losses. The rotor magnet poles can be separated into a number of circumferential pieces [7] and/or axial pieces [3], [6]. In this chapter, the circumferential segmentation scheme is used as it is more easily implemented in 2-D FE simulation.

Figure 2-9 shows the effect on the calculated rotor losses for the 12-slot designs found by laminated the rotor iron (top graph) and secondly by segmenting the rotor magnets (bottom graph). Laminating the rotor was simulated by changing its conductivity to zero and using the standard FE post-processing method to calculate iron loss. The magnet segmentation was done in two stages (see Figure 2-10). Firstly the conductive magnet ring was converted to electrically-isolated magnet poles, and secondly each magnet pole was segmented into four circumferential pieces by inserting small (0.25mm) radial airgaps into the finite-element model. The reduction in magnet volume due to these airgaps has a negligible effect on the back-EMF due to the small size of the airgaps.

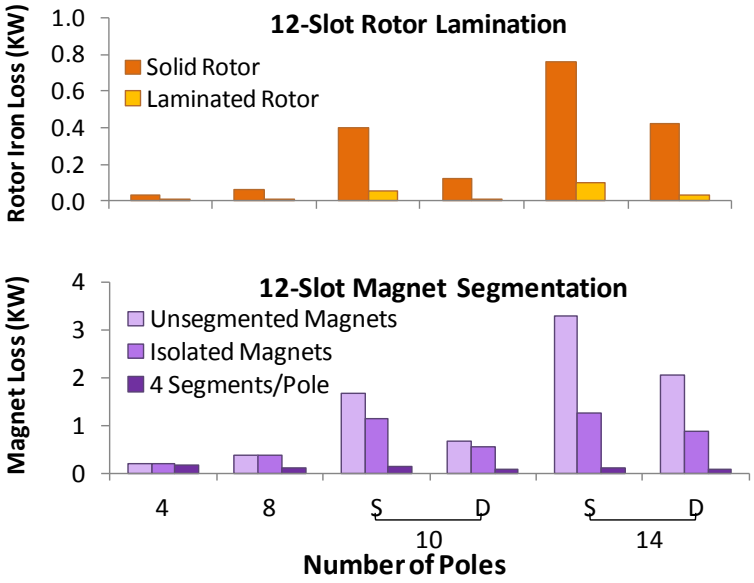

Figure 2-9: Calculated rotor iron and magnet losses showing the effect of lamination and magnet segmentation for the 12-slot machines at 6,000rpm

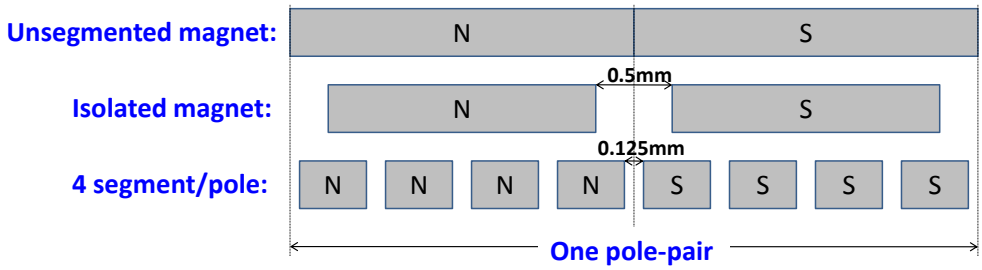

Figure 2-10: Diagram showing the schemes of segmenting the rotor magnets. Note the size of gaps is not drawn to scale. For example for the 10 pole machines, one pole-pair is about 29mm long.

Figure 2-9 shows that laminating the rotor iron and segmenting the rotor magnets substantially reduce the rotor losses. Note the higher the initial loss, the larger the percentage reduction with the magnet segmentation.

2.3.2. Full-Load Losses

Figure 2-11 reproduces the open-circuit losses at rated speed from Figure 2-6 and also shows the corresponding full-load losses (not including stator copper loss) at rated torque. The 36-slot stator uses a solid rotor and non-segmented magnets while the 12-slot stator uses a laminated rotor and has four magnet segments per pole to keep the rotor losses to reasonable levels. The 36-slot stator has low rotor and magnet losses and so using a laminated rotor and segmented magnets would have little effect on its performance except for the 32-pole design.

The full-load stator tooth and yoke losses are generally comparable to the open-circuit values for the distributed winding designs. For the 36-slot concentrated winding designs the stator tooth losses increase significantly with load, likely due to significant circulating flux in the stator tooth tips. For the 12-slot concentrated winding designs the stator yoke losses increase substantially, particularly for the single-layer windings. This is likely to be due to the high levels of leakage flux with this winding type.

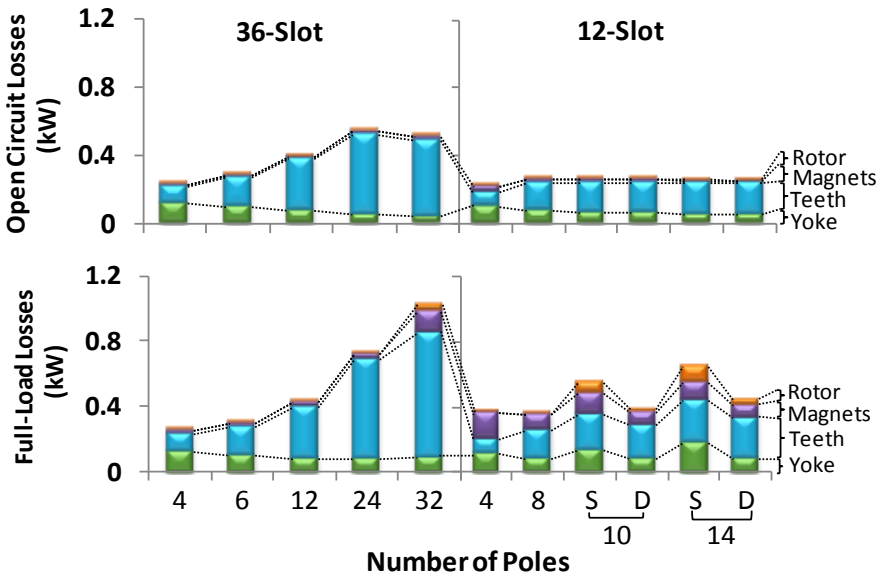

Figure 2-11: Calculated stator iron and rotor losses for the open-circuit (upper) and full-load conditions (lower) for 36- and 12-slot machines at 6,000 rpm. The 12-slot machines use a laminated rotor and 4 segments/pole

Figure 2-11 also shows the magnet and rotor iron loss. For the 12-slot designs, these rotor losses become smaller than the stator iron losses when using a laminated rotor and magnet segmentation.

Figure 2-12 shows the full-load iron and magnet losses from Figure 2-11 along with the full-load copper losses from Figure 2-5 to show the total full-load power loss and also the corresponding calculated efficiency. As the number of poles increase, the 36-slot designs show an initial drop in copper losses but a continuous increase in stator iron losses. This results in the 36-slot 6 and 12 pole designs having the lowest total loss with the 4 pole design not far behind.

For the 12-slot stator, the lowest losses are with the 8 pole design and the double-layer 10 and 14 pole rotors.

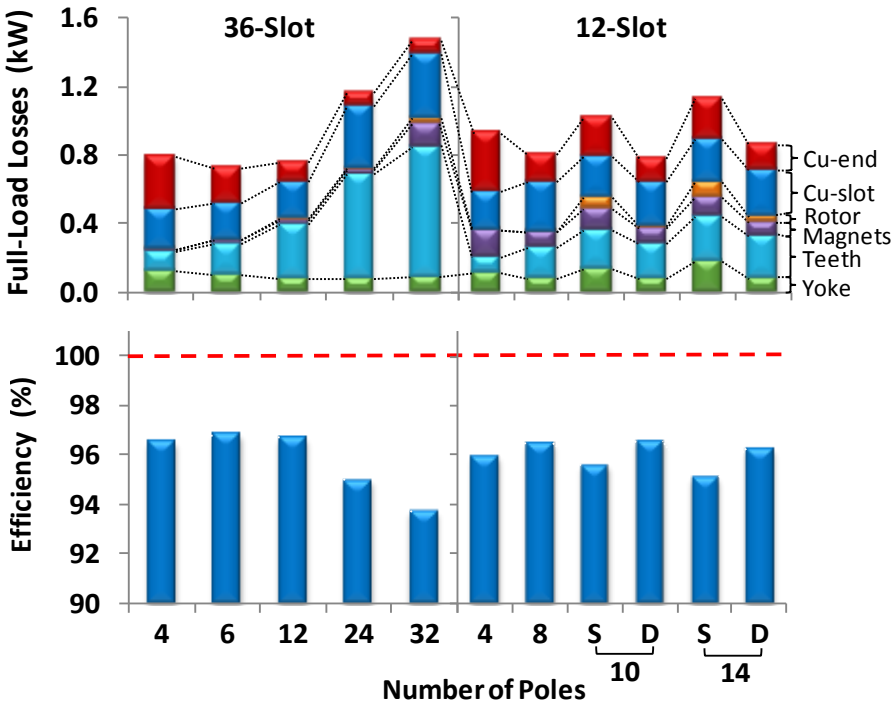

Figure 2-12: Calculated total full-load loss for the 36- and 12-slot (with the laminated rotor and 4 segments/pole) machines and corresponding calculated efficiency at 35 Nm and 6,000 rpm. Windage and bearing losses were not considered.

2.3.3. Torque Ripple

The torque ripple is the sum of the electromagnetic torque variations and the cogging torque. Assuming the stator currents are sinusoidal, the electromagnetic torque variations are due to non-triplen harmonics in the back-EMF waveform. The electromagnetic torque variations are at multiples of six times the fundamental frequency. The cogging torque has a frequency equal to the fundamental frequency multiplied by the lowest common multiple of the number of slots and poles, $LCM(S, 2p)$.

The graphs in the bottom row of Figure 2-3 show the cogging torque and torque ripple waveforms at rated (average) output torque. The peak total ripple torque and peak cogging torque are shown in Figure 2-13 for all the designs. Figure 2-3 shows as the number of poles increase, the back-EMF waveform becomes more sinusoidal and hence the electromagnetic torque ripple reduces in amplitude and increases in frequency.

As was seen earlier, the cogging torque is high for distributed winding machines and both reduces in amplitude and increases in frequency for concentrated winding machines.

In addition, double-layer designs have a more sinusoidal back-EMF and hence less electromagnetic torque ripple than single-layer designs.

The largest ripple torque is found with the 12-pole, 36-slot machine where the cogging and electromagnetic ripple torque have the same frequency. The smallest ripple torque is found with the 32-pole, 36-slot machine.

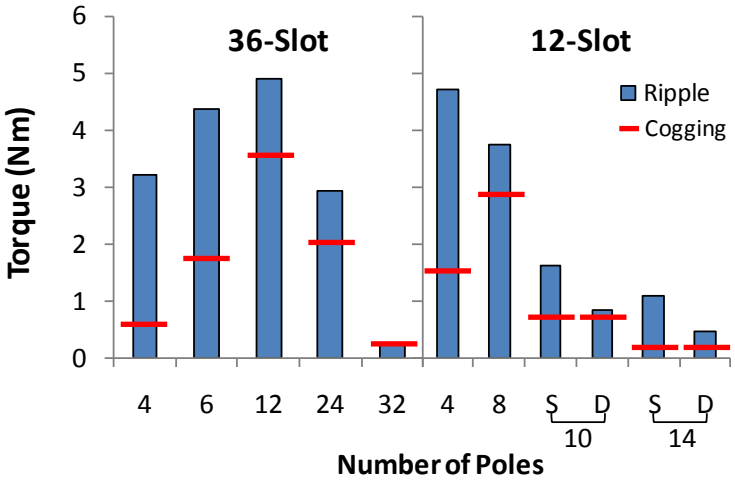

Figure 2-13: Calculated peak torque ripple at full-load in comparison to the peak cogging torque for the 36- and 12-slot machines

It is important to note that both the electromagnetic torque ripple and the cogging torque are sensitive to the magnet arc [1]. A constant value of magnet arc (180°) was used in this chapter. Substantial reductions in both the total ripple torque and cogging torque can be obtained by optimizing the magnet arc and using standard techniques such as skewing, though this will result in a small reduction in average torque.

2.4. Field-Weakening Performance

In this section, the field-weakening performance will be investigated for the 36- and 12-slot machines.

2.4.1. Inductance and Characteristic Current

The characteristic current I_{ch}, corresponds to the machine's high-speed short-circuit current [2],

$$I_{ch} = \frac{E_{ph}}{X_d} \tag{2-2}$$

where E_{ph} is the phase back-EMF voltage and X_d is the d-axis reactance which is the product of the d-axis inductance L_d and the electrical angular frequency ω_e. For good field-weakening performance it is desirable to make the characteristic current comparable to the rated current [42].

Figure 2-14 shows the back-EMF, the reactance X_d and the characteristic current (with the value of rated current highlighted) for each design. As seen earlier, the back-EMF varies between the designs due to differences in the fundamental airgap flux density and winding factor.

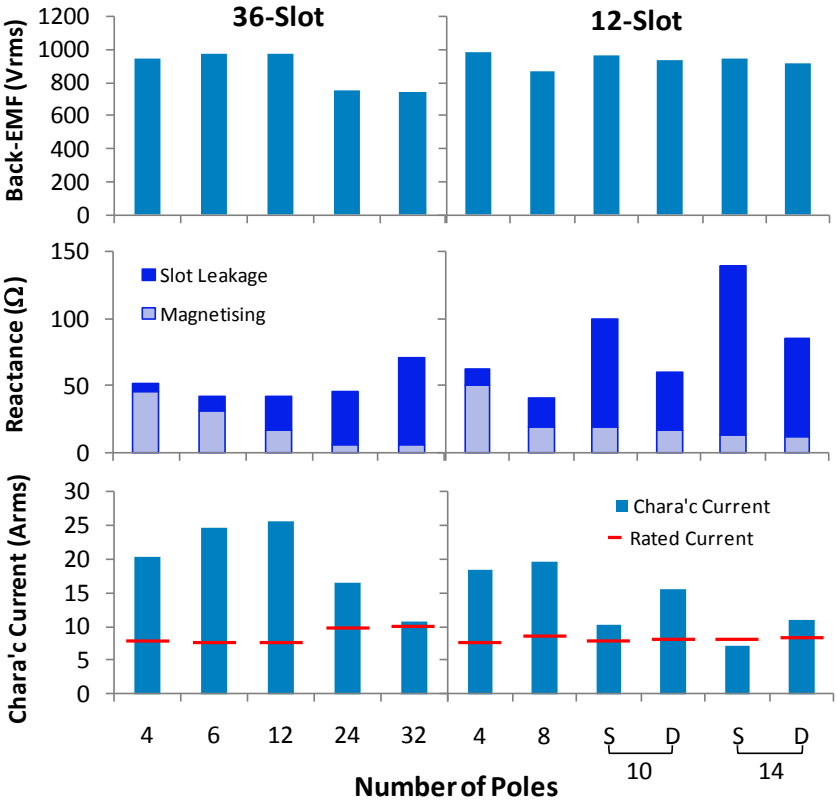

Figure 2-14: Calculated phase back-EMF, reactance (neglecting end-winding reactance) and characteristic current of 36- and 12-slot SPM machines at 6000rpm

The reactance X_d has three major components: the magnetizing reactance, the slot leakage reactance and the end-winding reactance.

The magnetizing inductance is inversely proportional to the square of the number of poles, but the electrical frequency is proportional to the number of poles so the net effect is

that the magnetizing reactance is inversely proportional to the number of poles, which can be seen in Figure 2-14. The magnetizing reactance values shown are analytically calculated from the number of effective sine-distributed turns.

The slot leakage inductance of the stator winding is inversely proportional to the number of slots, but to a first approximation, is not affected by the number of poles. Thus the slot leakage reactance would be expected to increase proportionally to the poles as the frequency increases.

In Figure 2-14 the slot leakage inductance was not calculated directly, but instead a 2-D finite-element simulation was used to calculate the total inductance and the difference between this and the analytically calculated magnetizing inductance is shown as slot-leakage inductance.

It was found that values of characteristic current close to the rated current is most easily obtained using concentrated winding designs [2]-[4], [6]. For instance the 32-pole, 36-slot machine has very low magnetizing reactance but a large slot leakage reactance. Alternatively, the single-layer 10-pole or 14-pole 12-slot designs have both large magnetizing and slot leakage inductance. Large values of slot leakage inductance mean that it is relatively easy to adjust the total inductance by small changes to the slot geometry, particularly near the slot opening.

Note that the end-winding leakage inductance was neglected in the above 2-D finite-element analysis calculations which will result in over-estimating the characteristic current, particularly in designs with high slot-leakage reactance.

2.4.2. Field-Weakening Performance

The field-weakening performance of the eleven machine designs was calculated based on the parameters from Figure 2-14 using identical values of rated voltage (1200V) and current (9.8A). The results are shown in Figure 2-15 where the dashed line shows the ideal field-weakening characteristic.

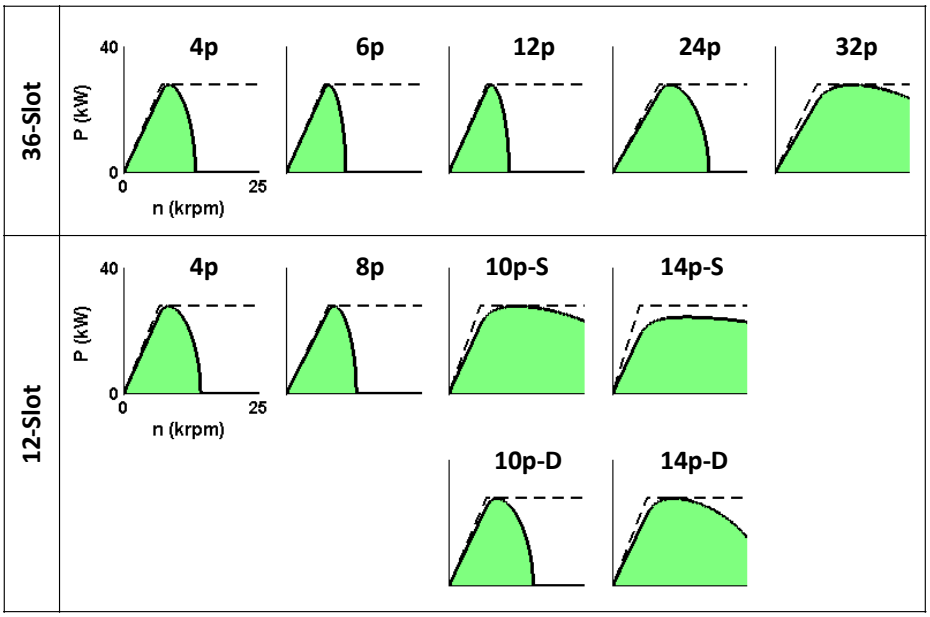

Figure 2-15: Calculated field-weakening output power versus speed for the 36- and 12-slot machines operating with the same voltage and current limit.

At low speeds, the output power increases linearly with speed with a slope proportional to the output torque. With the assumed constant value of rated current, the output torque is proportional to back-EMF.

At higher speeds, the field-weakening performance is determined by the characteristic current. Designs with high values of characteristic current compared to the rated current show limited high-speed operating performance as the magnet flux cannot be effectively opposed by the stator current, e.g. the 36-slot, 4-pole design. The closer the characteristic current is to the rated current, the wider the high-speed operating range, though there is some loss of output power around rated speed e.g. the 12-slot, 10-pole single layer design. If the characteristic current is below the rated current (e.g. the 12-slot, 14-pole, single-layer design) then the peak output power reduces.

The best field-weakening performance was found with the 36-slot 32-pole and the 12-slot 10-pole (single-layer) designs. Note that the results in Figure 2-15 can be strongly affected by the choice of the value of rated current, particularly for designs where the characteristic current is close to the rated current.

2.5. Conclusion

The effect of using different slot-pole combinations was studied in detail for a particular stator design to help machine designers gain useful insights into the effect on losses, torque ripple and field-weakening performance. The following are the key conclusions.

- Power loss at rated torque and speed for distributed windings: the stator iron loss increases with the number of poles while the copper loss decreases initially. This produces a minimum total loss with about 6 to 12 poles for the stator considered. The magnet and rotor iron losses can usually be neglected.
- Power loss at rated torque and speed for concentrated windings: low slot number machines (e.g. 12 slots for the stator considered) have high rotor losses unless segmented or bonded magnets and a laminated rotor are used. Double-layer windings have lower rotor and stator copper losses compared to the single-layer windings as they have reduced airgap spatial harmonics and shorter stator end-windings. The rotor losses were found to be proportional to the sum of the squares of the spatial airgap flux density harmonic components produced by the stator current.
- Cogging torque and torque ripple: for distributed windings with integer values of *SPP*, the peak value of the cogging torque and torque ripple increases with the number of poles due to the alignment between the magnet poles and the stator teeth. Concentrated windings normally have lower cogging torque and torque ripple.
- Field-weakening performance: concentrated windings give better field-weakening performance than distributed windings due to their higher slot leakage inductance producing values of characteristic current which are closer to rated current.

Chapter 3. Analysis of Iron Loss in IPM Machines under Deep Field-Weakening

Chapter 2 presented a general study of the slot-pole combinations with various windings configurations for SPM machines. However, SPM machines are not good candidates for high-speed field-weakening applications in comparison to the IPM machines for a variety of reasons, such as SPM machines having a higher back-EMF voltage and no reluctance torque. Also, the SPM machines have lower mechanical integrity because the magnets are located at the outer part of the rotor where the centrifugal force is very large when speed increases. Therefore, IPM rotors are usually preferred in the high-speed field-weakening conditions, and the distributed windings are often implemented to increase the magnetising inductance and hence the reluctance torque and thus the torque density. The iron loss in stator and rotor cores is one of the major issues for IPM machines operating under high-speed field-weakening conditions, although the sizing, thermal and structural aspects may also be important in a broader perspective.

In applications such as electric vehicle traction requiring a wide constant-power speed range, the iron loss of interior permanent magnet (IPM) machines at high speeds can significantly affect the overall efficiency. Operation at high speed in traction drives

corresponds to deep field-weakening conditions. This is where the flux from the *d*-axis stator current is comparable to the magnet flux and the fundamental airgap flux density component is small. Due to the high synchronous frequency and the frenquent variation of iron flux density in one electical cycle, the eddy-current loss is normally much larger than the hysteresis loss [25][27][28], and so will be the only type of iron loss considered.

3.1. Introduction

Infinite constant-power speed range can be obtained when the operating current is equal to the characteristic current I_{ch}, see Figure 3-1. At speeds belows the corner speed (point 1 in Figure 3-1), the machine operates with limit current under the maximum-torque-per-ampere (MTPA) control strategy in order to minimize the copper loss which is the dominant loss at low speed. At speeds above the corner speed, the machines operates under the field-weakening (FW) with the *dq*-axis current trajectory infinitely approaching the chartristic current I_{ch} and the iron loss increasingly dominantes the copper loss with increase of speed up-to the deep field-weakening (point 2 in Figure 3-1), where the iron loss is similar to the high-speed short-circuit condition in general with $I_d = I_{ch}$ and $I_q \approx 0$ [24].

This chapter will focus on the eddy-current loss, the dominant form of iron loss under deep field-weakening conditions, and propose a new closed-form formulation for calculating the stator and rotor eddy-current loss. The detailed comparisons of the optimized and baseline designs will be presented in this chapter, using a combination of closed-form analytical expressions, finite-element analysis (FEM) and experimental validation.

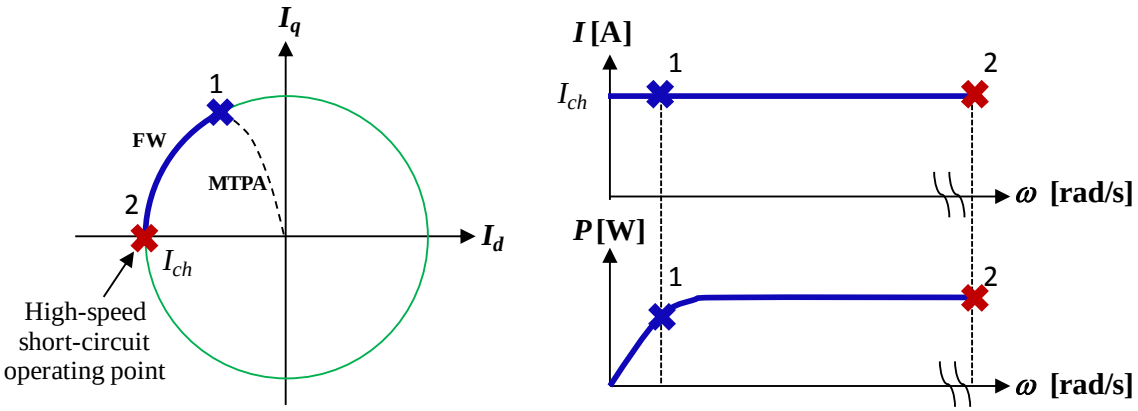

Figure 3-1: Diagram showing the deep field-weakening with the optimal operating current limit

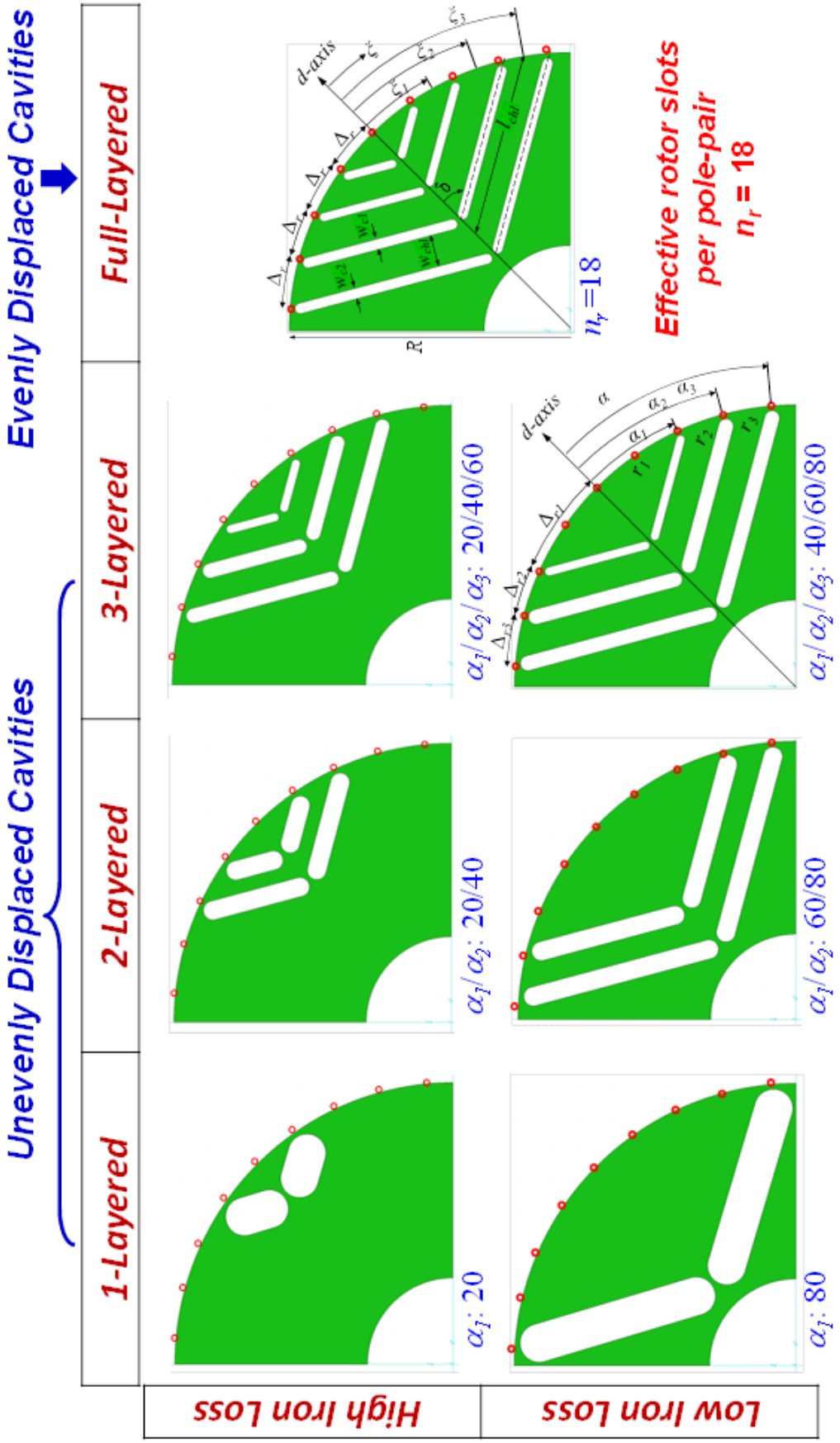

Figure 3-2: Cross-sections of rotors with n_r = 18, showing examples of 1-, 2- and 3-layered rotors, and the full-layered (4-layer) rotor. It also shows the definitions of the rotor α and ξ angular coordinate systems, rotor layer angular spacing Δ_r and $\Delta_{r1\text{-}3}$ and rotor potentials $r_{1\text{-}3}$.

Vagati et al. showed that the torque ripple can be largely reduced by adopting evenly-spaced rotor cavities, i.e. by maintaining the rotor-effective-slot number [29], [30]. In this chapter, the rotor-effective-slot number n_r is adopted to represent the potential circumferential positions for placing the rotor cavities. Figure 3-2 shows seven example rotors with the same rotor-effective-slot number n_r = 18 which corresponds to 9 evenly-spaced (20° elec.) potential angular cavity positions per pole along the rotor circumference which are shown as red circles. The rotor cavities, otherwise known as rotor slots, flux barriers or layers, can begin and end at these slot positions. This leads to rotor barriers which are regularly spaced at angles which are multiples of $2\pi/ n_r$.

In Figure 3-2, the notation of the angular cavity positions is used in the form of $\alpha_1/\alpha_2/\alpha_3\cdots$. The arrangement of the cavity positions can be classified into two categories in general: unevenly displaced cavities and evenly displaced cavities.

The design with n_r = 18 can have a maximum number of rotor layers (called a full-layered rotor) of four. There are also multiple alternatives of designs with fewer rotor layers, 1-, 2- and 3-layers, some of which are shown. The total (that is, the sum of the) thickness of the rotor barriers per pole is kept constant, in order to obtain a similar value of *d*-axis inductance L_d.

For the designs shown, the angular positions of the ends of the rotor cavities of a full-layered rotor are evenly spaced along the rotor circumference (20° elec.) while those for 1-, 2- and 3-layered rotors are not necessarily evenly spaced (but are still multiples of 20° elec.).

The first row of Figure 3-2 shows the high-iron-loss cavity arrangements for the unevenly-displaced-cavities rotors, while the second row shows the low-iron-loss cavity arrangements for the evenly-displaced-cavities rotors. The detailed explanation of the rotor cavity arranements will be given in Section 3.3.

3.1.1. Related Works

Under deep field-weakening conditions, the fundamental airgap flux is relatively low and the stator eddy-current loss is primarily caused by the rotor mmf harmonics due to the presence of flux barriers in the rotor. Earlier work used the total harmonic distortion (THD) value to quantify the level of rotor mmf harmonics in the stator iron loss analysis

[24]. Han et al. proposed the power-loss-stator-teeth (PST) index which improved the THD analysis by including the filtering effect of the stator teeth tips [25]. Barcaro et al. used lumped-circuit modelling of the rotor-mmf to predict the stator teeth eddy-current loss including the parameters of rotor geometry [26]. Pellegrino et al. presented the analytical modelling of the rotor-mmf using the discrete-time sample modelling of the rotor-mmf by only considering the rotor-mmf produced by the stator-mmf harmonics [27]. The discrete-time sample modelling of rotor-mmf presented in [27] is limited to the IPM/reluctance rotors with evenly displaced cavities. Rotor channel "tunneling" of the stator mmf slot harmonics is the major cause of the rotor eddy-current loss for interior PM and synchronous reluctance machines with multi-layered rotor designs [27], [28].

Pellegrino et al. presented the trade-off between the minimization of eddy-current loss and torque ripple, and suggested optimal slot numbers for the stator and rotor [27]. Han et al. discussed the optimal rotor channel location to minimize the tunneling of the stator mmf slot harmonics [28]. In [28], it was also indicated that these optimal channel locations cannot be obtained without changing the rotor-effective-slot number.

Based on the above review, the impact of stator-slot and rotor-effective-slot number for unevenly displaced cavities and for varying numbers of rotor-cavity layers on the total eddy-current loss of interior PM machines under field-weakening conditions has not been seen in the literature.

3.1.2. Objectives and Contributions

The key contributions of this chapter are summarized bellow,

- This chapter proposes a novel closed-form formulation for calculating the stator and rotor eddy-current loss for various numbers of layers of rotor cavities. This formulation applies to distributed windings with fractional and integer SPP values > 1, but it does not apply to SPP values < 1.
- The optimal circumferential positions of rotor cavities to minimize total eddy-current loss for 1-, 2- and 3-layered rotors are explored.
- The effect of large changes in the stator-slot and rotor-effective-slot number on total eddy-current loss is investigated.
- The impact of changing the number of rotor-cavity layers on total eddy-current loss is presented.

The structure of this chapter is as follows. Section 3.2 presents the analytical modelling of eddy-current loss for the stator and rotor iron cores. Section 3.3 examines the optimal positioning of rotor-cavities to minimize the total eddy-current loss for unevenly spaced cavities. Section 3.4 covers the total eddy-current loss changes with stator-slot and rotor-effective-slot number with the optimal positioning of rotor cavities presented in Section 3.3.

3.2. Analytical Eddy-Current Loss Modelling

The development of the closed-form eddy-current loss solutions consists of the following steps. Firstly the rotor-mmf is calculated. From this the harmonic flux density components in the airgap, stator teeth and yoke are derived and the stator teeth and yoke iron loss densities are determined. Next the rotor iron loss densities are found based on an analysis of the *q*-axis tunnelling flux in the rotor. In this context, tunnelling refers to the flux passing through the rotor channels. Finally the volumes of the stator and rotor iron are calculated.

The rotor magnet eddy-current loss is small for designs with distributed stator windings in general [8], as the stator-mmf harmonics are limited and the magnets are buried deeply inside the rotor iron for the interior PM machines.

3.2.1. Stator and Rotor Magneto-Motive Force

3.2.1.1. Stator Magneto-Motive Force

The stator-mmf is produced from the accumulation of current conductors distributed along the stator slots. The analytical expression of stator-mmf [32] is,

$$f_s(\theta,t)=\frac{3}{2}\frac{4}{\pi}\frac{N_t I_m}{P}\left[\sum_{h=1,7,13...}\frac{k_{sh}}{h}\sin(h\theta-\omega_e t)+\sum_{h=5,11,17...}\frac{k_{sh}}{h}\sin(h\theta+\omega_e t)\right] \tag{3-1}$$

The fundamental component of stator-mmf is,

$$f_{s1}(\theta,t)=\hat{f}_{s1}\cdot\sin(\theta-\omega_e t) \tag{3-2}$$

and amplitude of fundamental stator-mmf is

$$\hat{f}_{s1} = \frac{3}{2}\frac{4}{\pi}\frac{N_t I_m}{P} k_{s1} \tag{3-3}$$

where,

- θ is the stator angle coordinate in [elec. deg];
- k_{sh} is the winding factor;
- h is the order of stator-mmf spatial harmonics.
- P denotes the number of poles;
- ω_e is the synchronous angular frequency [rad/s], $\omega_e = 2\pi f_1$
- N_t is the total turns per phase;
- I_m is the peak of phase current [Apk]

It is worth noticing that the fundamental component of stator-mmf rotates with same speed and direction as the rotor.

3.2.1.2. Rotor Magneto-Motive Force

In this thesis, the rotor mmf for the cases with unevenly-displaced cavities in Figure 3-2 was modelled using a lumped-circuit approach, while the rotor mmf for the cases with evenly-displaced cavities (or full-layered) was modelled based on a discrete-sampling process [27] as the regular spatial step-changes in rotor mmf results in primary rotor-slot harmonic components ($k \cdot n_r \pm 1$, $k = 1, 2, 3\ldots$).

Method 1: Lumped-Circuit Magnetic Model

The spatial distribution of an ideal stepped rotor mmf can be expressed as a Fourier series' expansion,

$$f_r(\theta, t) = \sum_{h=1}^{\infty} \hat{f}_{rn} \cos(h\theta - h\omega_e t) \tag{3-4}$$

where the amplitude of n^{th} harmonic rotor-mmf is expressed as

$$\hat{f}_{rn} = \frac{4}{\pi}\frac{1}{n}\cdot\sum_{j}\sin(n\alpha_j)\cdot(r_j - r_{j+1}) \tag{3-5}$$

where,

- α_j is the angular position [elec. deg] for the j-th rotor cavity in Figure 3-2;
- r_j is the magnetic potential for the j^{th} rotor iron segment. This segment is magnetically isolated by the $(j\text{-}1)^{th}$ and j^{th} rotor cavities.

Equation (3-4) shows that all the rotor mmf harmonics rotate at the same mechanical speed, which is the same speed as the stator fundamental mmf. The magnetic potential for each rotor iron segment r_j can be generally calculated based on a linear lumped-circuit magnetic model [31], [26] and [34]. An example rotor with 3-layered cavities has three values of rotor mmf, r_1, r_2 and r_3 as shown in Figure 3-3. The general assumptions made in this method include,

- the stator and rotor iron have infinite permeability apart from the rotor ribs, where the mmf drop and saturation of the iron was ignored;
- an equivalent smooth stator was obtained by adopting Carter's coefficient;
- only the rotor mmf produced by the fundamental stator mmf in (3-5) is considered. This results in a rotor mmf which does not vary with time.

Based on the above assumptions, the application of the fundamental stator mmf results in a constant magnetic scalar potential within each of the rotor iron channels. Therefore, the rotor mmf distribution along the rotor periphery is a symmetric waveform with respect to the d- and q-axes. A magnetic circuit representing one-half pole of the machine can then be used to calculate the rotor mmf as shown in Figure 3-3 b.

In Figure 3-3 b, $\overline{f_{s1}^{\Delta r1}}$, $\overline{f_{s1}^{\Delta r2}}$ and $\overline{f_{s1}^{\Delta r3}}$ are the spatial averages of the stator mmf over the corresponding rotor iron segment span Δ_{r1}, Δ_{r2} and Δ_{r3}; R_g is the sectional airgap reluctance and R_b is the rotor flux barrier reluctance. The rotor bridges are assumed to be saturated with a constant leakage flux density.

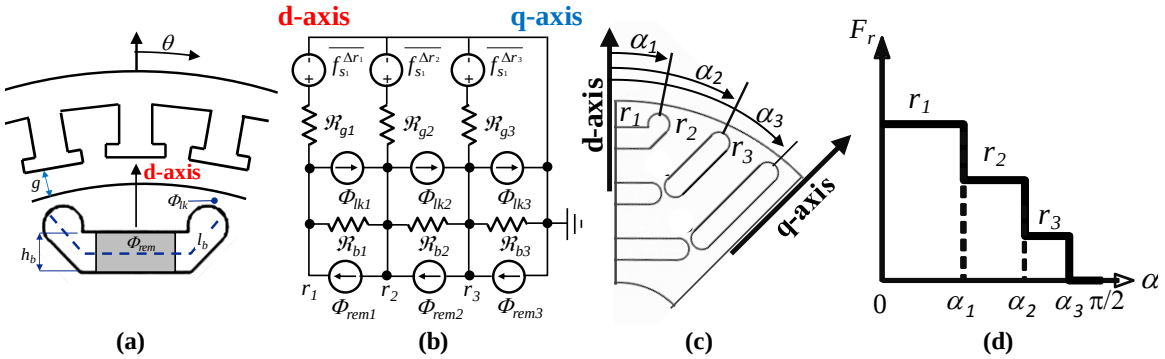

Figure 3-3: Diagrams showing: the major quantities and reference axes (a), the simplified ½-pole magnetic circuit used for calulating the rotor mmf assuming a sinusoidal stator MMF (b), the rotor barrier angular locations and mmfs (c), and the corresponding rotor mmf for a ¼ electric cycle (d)

The magnetic scalar potential obtained from the magnetic circuit in Figure 3-3 b can be expressed as,

$$\begin{bmatrix} r_1 \\ r_2 \\ r_3 \end{bmatrix} = T_{\Re} \cdot \begin{bmatrix} \Phi_{rem1} + \overline{f_{s1}^{\Delta r1}} / \Re_{g1} - \Phi_{lk1} \\ \Phi_{rem2} - \Phi_{rem1} + \overline{f_{s1}^{\Delta r2}} / \Re_{g2} - \Phi_{lk2} \\ \Phi_{rem3} - \Phi_{rem2} + \overline{f_{s1}^{\Delta r3}} / \Re_{g3} - \Phi_{lk3} \end{bmatrix} \tag{3-6}$$

where the conversion matrix $T_{\Re}$ is expressed as,

$$T_{\Re} = \begin{bmatrix} \frac{1}{\Re_{b1}} + \frac{1}{\Re_{g1}} & -\frac{1}{\Re_{b1}} & 0 \\ -\frac{1}{\Re_{b1}} & \frac{1}{\Re_{b1}} + \frac{1}{\Re_{b2}} + \frac{1}{\Re_{g2}} & -\frac{1}{\Re_{b2}} \\ 0 & -\frac{1}{\Re_{b2}} & \frac{1}{\Re_{b2}} + \frac{1}{\Re_{b3}} + \frac{1}{\Re_{g3}} \end{bmatrix}^{-1} \tag{3-7}$$

Equations (3-6) and (3-7) show that the rotor-mmf comes from three sources: stator-mmf f_s, magnet remanent flux Φ_{rem} and rotor-rib leakage flux Φ_{lk}. Under the open-circuit condition, the stator-mmf f_s equals zero and the magnet remanent flux Φ_{rem} is the only one producing rotor mmf. In comparison, the rotor mmf produced by the stator-mmf f_s is generally much larger than the rotor mmf produced by the magnet remanent flux Φ_{rem} under the deep field-weakening condition. Due to the fact that rotors of IPM/Reluctance machine are usually designed to be highly magnetically anisotropic to achieve greater

reluctance torque, the cavities' reluctance $\Re_b$ can be much greater than the sectional airgap reluctance. This leads to the cavities' reluctance $\Re_b$ being assumed to be infinite in some analysis situations.

Equations (3-6) and (3-7) include all the factors which affect the rotor mmf. Among these factors, the angular positions of the rotor cavities α_1, α_2 and α_3 have been identified to be the major factor affecting the rotor-mmf harmonics and hence the stator teeth and yoke eddy-current loss. An analytical expression of the rotor mmf as a function of the angular positions of the rotor cavities can be derived based on the following further assumptions:

- Impact of the magnet remanent flux, the flux passing through the rotor layers and the rib leakage flux can be neglected with appropriate designs [27]. The rotor mmf contributed by the magnet remanent flux are far less than the rotor mmf contributed by the stator current under the deep field weakening conditions which can be also neglected [27];

Based on the above assumptions, the analytical expression of rotor mmf in (3-6) and (3-7) can be simplified by neglecting the terms corresponding to the magnet remanent flux Φ_{rem} and the rotor-rib leakage flux Φ_{lk} and by setting the cavities' reluctance $\Re_b$ to infinity, and expressed as a function of the fundamental stator-mmf amplitude $\hat{f}_{s1}$ and positions of rotor cavities α_j,

$$r_j = \hat{f}_{s1} \cdot \frac{\sin(\alpha_j) - \sin(\alpha_{j-1})}{\alpha_j - \alpha_{j-1}} \tag{3-8}$$

For the case of r_1, the potential of the outermost iron segment, α_{j-1} equals zero.

Method 2: Discrete-Time Sampling Model

The cavities for the full-layered rotor are evenly spaced along the rotor periphery. The rotor mmf produced by the fundamental stator mmf for the full-layered rotors can thus be obtained by adopting a discrete-time sampling model [27]. The amplitude of the n^{th} harmonic of the rotor mmf in (3-5) can be simplified by only considering the rotor-slot harmonics $n = k \cdot n_r \pm 1$, and expressed as,

$$\hat{f}_{rn} = \frac{\hat{f}_{s1}}{n} \cdot \left(\operatorname{sinc} \frac{\pi}{n_r} \right)^2 \tag{3-9}$$

where the sinc function used is defined as $\sin(x)/x$.

Equations (3-5) and (3-9) give the same results for full-layered designs, e.g. a 4-layer design with $n_r = 18$, 3-layer with $n_r = 12$, 2-layer with $n_r = 8$ and 1-layer with $n_r = 4$.

For full-layered rotors, the largest rotor mmf harmonics are of the order $n = k \cdot n_r \pm 1$ and they have negligible low-order harmonics (e.g. 3rd, 5th, 7th). In comparison, the use of unevenly displaced rotor cavities reduce the number of spatial steps in the rotor mmf and hence its rotor-slot harmonic components, but instead, they can have significant low-order harmonics, particularly with low numbers of layers.

In this thesis, the two rotor-mmf expressions (3-5) and (3-9) are used for evenly and unevenly displaced cavities, because the dominant harmonic components in the rotor mmf may change from the rotor-slot harmonics ($k \cdot n_r \pm 1$) for evenly-dispaced cavities (e.g. full-layered rotor in Figure 3-2) to the low-order harmonics (3rd, 5th, 7th) for the unevenly-dispaced cavities (e.g. 1-, 2- and 3-layered rotors in Figure 3-2). This will be further analyzed and verified by FEM and experimental testing in the following chapters.

3.2.2. Stator Flux and Eddy-Current Loss Density

The spatial harmonics of the rotor-mmf lead to stator iron loss. In this section, the analytical expressions of flux density and hence iron loss in the stator yoke and teeth are derived as a function of the rotor-mmf.

As noted above, only the rotor-mmf produced by the fundamental stator-mmf will be considered. The stator-mmf spatial harmonics have negligible effect on the stator iron loss because of their much lower rotating speed with respect to the stator compared to the rotor-mmf harmonics.

3.2.2.1. Airgap, Stator Yoke and Teeth Flux Density

The spatial sum of the stator- and rotor-mmf results in the spatial distribution of radial airgap flux density B_g which can be obtained as,

$$\begin{aligned} B_g(\theta,t) &= \frac{\mu_o}{g_e}\left[F_r(\theta,t) - F_s(\theta,t)\right] \\ &= \sum_{n=1,\,3,\,5\ldots} \hat{B}_{gn} \cos\left(\frac{nP}{2}\theta - n\omega_e t\right) \end{aligned} \tag{3-10}$$

The amplitude $\hat{B}_{gn}$ is,

$$\hat{B}_{gn} = \begin{cases} \hat{B}_{gr1} - \hat{B}_{gs1} = \dfrac{\mu_o}{g_e}\left(\hat{f}_{r1} - \hat{f}_{s1}\right) & \text{for } n = 1 \\ \hat{B}_{grn} = \dfrac{\mu_o}{g_e}\,\hat{f}_{rn} & \text{for } n > 1 \end{cases} \tag{3-11}$$

Assuming that the fundamental stator mmf $f_{s1}(\theta)$ is equal to the fundamental rotor mmf $f_{r1}(\theta)$ in amplitude but opposite in direction under optimal deep field-weakening condition, the fundamental airgap flux density resulting by summing the two terms is close to zero. The spatial distribution of airgap flux density contributed by the rotor-mmf $f_r(\theta)$ only is denoted as B_{gr}, see (3-12). The stator tooth flux density B_t is obtained by averaging B_{gr} over a stator slot pitch Δ_s, see (3-13). The stator yoke flux density B_y is obtained by integrating a "freezed" B_{gr} with a constant speed of $-\omega_r$. This results in (3-14).

$$B_{gr}(\theta) = \frac{\mu_o}{g_e}\, f_r(\theta) = \sum_{n=3,5,7\ldots} \hat{B}_{grn} \cos(n\theta) \tag{3-12}$$

$$B_t(t) = \frac{k_t}{\Delta_s} \int_{-\Delta_s/2}^{\Delta_s/2} B_{gr}(\theta,t)\, d\theta = \sum_{n=3,5,7\ldots} \hat{B}_t \cos(n\omega_r t) \tag{3-13}$$

$$B_y(t) = \frac{k_y}{\pi} \int_{0}^{-\omega_r t} \hat{B}_{gr} \cos(n\theta)\, d\theta = \sum_{n=3,5,7\ldots} \hat{B}_y \sin(-n\omega_r t) \tag{3-14}$$

By solving the above equations, it can be shown that the amplitudes of n^{th} (n >1) harmonics of the above flux density components are,

$$\hat{B}_{grn} = \frac{\mu_o}{g_e}\,\hat{f}_{rn} \tag{3-15}$$

$$\hat{B}_{tn} = \frac{\mu_o}{g_e}\,\hat{f}_{rn} \cdot k_t \cdot \mathrm{sinc}\left(\frac{n\pi}{n_s}\right) \tag{3-16}$$

$$\hat{B}_{yn} = \frac{\mu_o}{g_e}\,\hat{f}_{rn} \cdot k_y \cdot \frac{1}{n\pi} \tag{3-17}$$

where,

- n_s is the number of stator slots per pole-pair
- μ_o is the magnetic permeability of a vacuum;
- g_e is the effective airgap length;
- θ is the stator circumferential coordinate;
- Δ_s is the the stator tooth pitch angle;
- k_t is the ratio of the stator tooth pitch length at airgap to the stator tooth-body width;
- k_y is the ratio of the pole pitch length at airgap to the stator yoke radial thickness;

As the stator tooth flux is the spatial average of the airgap flux density over the stator tooth pitch, see (3-13), this results in the sinc function in (3-16). For instance, when the stator tooth pitch is equal to the spatial wavelength of the rotor slot-harmonic mmf then there is no stator tooth flux. This is because the rotor slot-harmonic mmf produces circulating flux at the tip of the stator tooth but this flux does not enter the tooth body. Thus using a lower stator slot number generally results in lower stator losses. The rotor yoke flux density expression in (3-17) shows that the rotor mmf harmonic amplitudes are divided by the harmonic number. Note that all $n > 1$ harmonics in the yoke and teeth flux density come from the rotor mmf.

3.2.2.2. Stator Yoke and Teeth Eddy-Current Loss Densities

The stator teeth and yoke eddy-current loss densities [W/m^3] are obtained by applying Parseval's theorem,

$$p_{eddy} = k_e f_1^2 \sum \hat{B}_n^2 \cdot n^2 \tag{3-18}$$

where,

- f_1 is the fundamental frequency;
- k_e is the eddy-current coefficient [W/m^3]. The same value of k_e = 1.0 W/m^3 is assumed in both the analytical and FEM calculation of the eddy-current loss in this chapter.

By substituting (3-16) and (3-17) into (3-18), the final closed-form expressions of the eddy-current loss density [W/m^3] for the stator tooth and yoke as a function of the rotor-mmf harmonics f_{rn} can be obtained as,

$$p_{teeth} = k_e f_1^2 \cdot \left(k_t \frac{\mu_o}{g_e} \frac{n_s}{\pi} \right)^2 \sum \hat{f}_{rn}^2 \cdot \left[\sin\left(\frac{n\pi}{n_s} \right) \right]^2 \tag{3-19}$$

$$p_{yoke} = k_e f_1^2 \cdot \left(k_y \frac{\mu_o}{g_e} \frac{1}{\pi} \right)^2 \sum \hat{f}_{rn}^2 \tag{3-20}$$

The derivation of the harmonic components of the yoke flux density by equations (3-14) and (3-17) based on integrating the airgap flux density components is a novel analytical procedure proposed by the thesis. This allows a closed-form expression (3-20) for the yoke eddy-current loss to be obtained. The previous analytical procedure to find the yoke flux density is to sum the flux in the stator teeth flux over half a pole [27], [34]. However this method does not produce a closed-form expression for the yoke flux nor the iron loss.

3.2.3. Rotor Flux and Eddy-Current Loss Densities

In the previous subsections it has been shown that knowledge of the rotor mmf waveform leads to a closed-form solution of the airgap flux and hence loss density in the stator teeth and yoke. In this subsection, knowledge of the stator mmf harmonic amplitudes leads to a closed-form calculation of the resulting rotor flux and hence loss density in the rotor.

The rotor layers separate the rotor into a number of magnetic channels or segments which carry *q*-axis flux. The fundamental stator mmf is synchronised to the rotor and produces non time-varying values of *q*-axis flux. However the stator mmf harmonics are not synchronised to the rotor and can produce large amplitude, time-varying flux densities in these rotor channels (called "tunneling"). This *q*-axis "tunneling" flux has been identified as the primary cause of rotor eddy-current loss for multi-layered rotors [28].

The following assumptions were made in the analysis. The effect of flux crossing the cavities and rotor saturation was neglected. In addition, the rotor surface loss produced by the combination of the airgap permeance variation and stator mmf harmonics are not included.

The *q*-axis tunneling flux is obtained by taking the difference of the spatial-averaged stator mmf components seen by each end of a rotor channel, divided by the total effective airgap reluctance (see Figure 3-4).

$$B_{chl}(t)=\frac{\mu_0}{g_e}\frac{k_{chl}}{2}\left(\int_{\xi_j-\Delta_r/2}^{\xi_j+\Delta_r/2} f_{sh}\,d\xi-\int_{-\xi_j-\Delta_r/2}^{-\xi_j+\Delta_r/2} f_{sh}\,d\xi\right) \tag{3-21}$$

The major harmonic component in the *q*-axis tunneling flux is of the order of $k{\cdot}n_s$, which is produced by the interaction of the two stator-mmf harmonic side-bands ($k{\cdot}n_s{\pm}1$), where k is an integer (k =1, 2, 3…). The amplitude of the ($k{\cdot}n_s$)-order tunneling flux with k = 1 is expressed as,

$$\hat{B}_{chl}=\frac{\mu_o}{g_e}k_{chl}\sum_{h=n_s\mp1}\hat{f}_{sh}\cdot\sin\left(h\xi_j\right)\cdot\mathrm{sinc}\left(\frac{h\Delta_r}{2}\right) \tag{3-22}$$

where,

- $\hat{f}_{sh}$ is the amplitude of the h-order stator mmf component,

$$\hat{f}_{sh}=\pm\hat{f}_{s1}/h \qquad \text{for } h=n_s\mp1 \tag{3-23}$$

  '+' for $h = n_s-1$ and '–' for $h = n_s+1$;

- h is the order of the stator mmf harmonics;
- k_{chl} is the ratio of the rotor channel pitch length at airgap to the rotor channel width;

- ξ_j is the circumferential position of the pitch center of a rotor channel at the airgap (see Figure 3-2);
- Δ_r is the the rotor channel pitch angle, i.e. the circumferential interval between two adjacent cavities; Δ_r is constant and equal to $2\pi/n_r$ [elec. rad] for the full-layered rotor as shown in Figure 3-2. Note $\Delta_{r1} = \alpha_1$, $\Delta_{r2} = \alpha_2 - \alpha_1$ and $\Delta_{r3} = \alpha_3 - \alpha_2$ for 3-layer rotors.

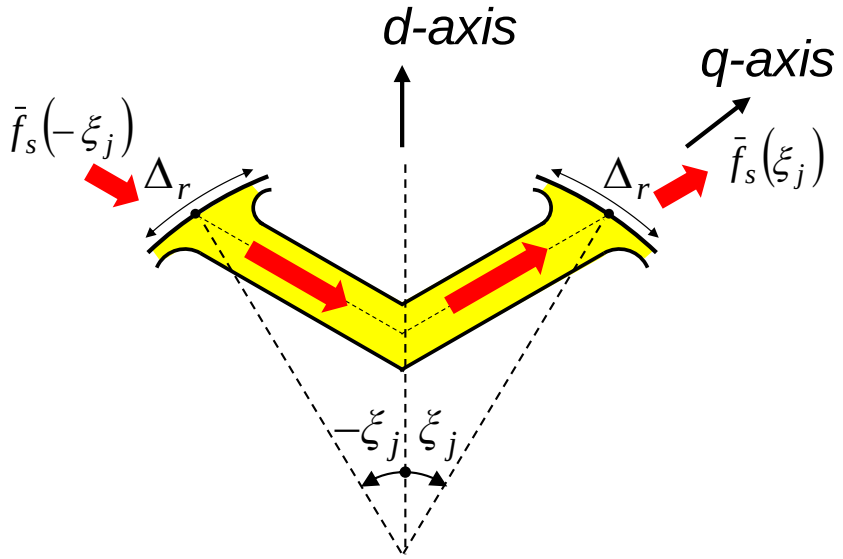

Figure 3-4: Diagram showing the *q*-axis "tunneling" flux in a rotor channel

Applying Parseval's theorem and considering only the dominant component in the frequency spectrum of order $k \cdot n_s$, the final rotor eddy-current loss density expression as a function of stator-mmf harmonics f_{sh} with $k = 1$ is obtained as,

$$p_{chl} = k_e f_1^2 \left[\frac{\mu_o}{g_e} k_{chl} n_s \sum_{h=n_s \mp 1} \hat{f}_{sh} \cdot \sin(h\xi_j) \cdot \mathrm{sinc}\left(\frac{h\Delta_r}{2} \right) \right]^2 \tag{3-24}$$

This derivation of a closed-form expression for the *q*-axis tunneling eddy-current loss is novel. Equation (3-24) is helpful to understand and estimate how the iron loss of a single rotor channel varies with its location and pitch angle. The analysis in [28] identified the key parameters (the rotor channel positions) and proposed optimal values to minimize the tunneling flux. Reference [27] shows the rotor-channel flux is the integral of the airgap

flux over the channel pitch. In neither work was a closed-form rotor-tunneling flux solution presented.

3.2.4. Volumes of Stator and Rotor Iron

The stator and rotor iron volumes are required to calculate the total iron losses. Their key geometric parameters are shown in Figure 3-5.

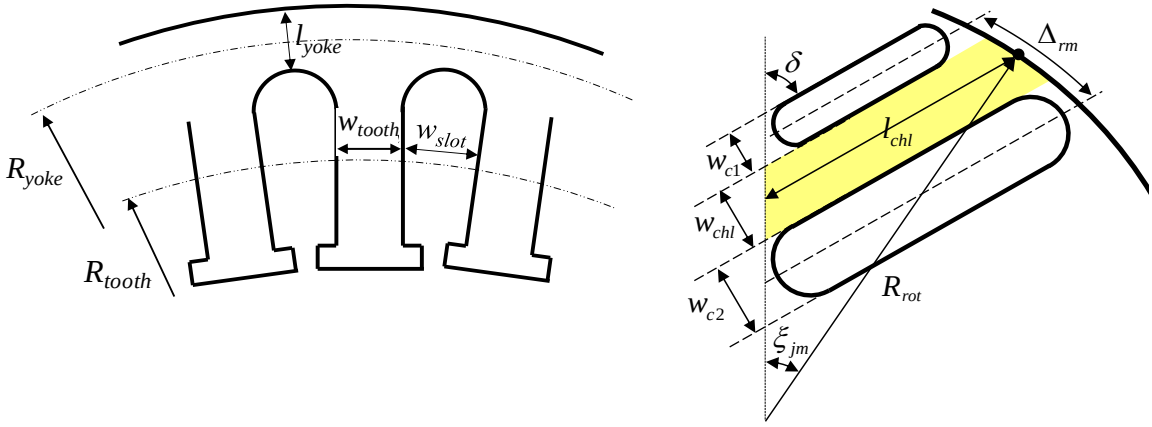

Figure 3-5: Diagram showing the parameters used for calculating the iron volumes

The stator yoke volume V_{yoke} is kept constant by maintaining the yoke thickness l_{yoke} when the stator slots number changes,

$$V_{yoke} = l_{yoke} \cdot 2\pi R_{yoke} \cdot l_{stk} \tag{3-25}$$

where,

- l_{stk} is the stack length of stator and rotor laminations;
- R_{yoke} is the average radius of the stator yoke;

The stator tooth volume V_{tooth} is kept constant by keeping the same ratio of tooth-body width w_{tooth} to slot width w_{slot} when the stator slot number changes,

$$V_{tooth} = l_{tooth} \cdot 2\pi R_{tooth} \frac{w_{tooth}}{w_{tooth} + w_{slot}} \cdot l_{stk} \tag{3-26}$$

where,

- l_{tooth} is the radial length of stator teeth;
- R_{tooth} is the average radius of stator teeth;

From geometry, the expressions for the rotor-channel mean length l_{chl_j}, mean width w_{chl_j} (see Figure 3-2) and volume V_{chl_j} can be obtained as,

$$l_{chl\_j} = 2R_{rot} \cdot \sin\left(\frac{\Delta_{rm}}{2}\right) \cdot \cos\left(\xi_{jm} - \delta\right) \tag{3-27}$$

$$w_{chl\_j} = R_{rot} \cdot \frac{\sin \xi_{jm}}{\sin \delta} - w_c \tag{3-28}$$

$$V_{chl\_j} = l_{chl\_j} \cdot w_{chl\_j} \cdot l_{stk} \tag{3-29}$$

where,

- ξ_{jm} is the circumferential position of the pitch center of rotor channel j at airgap in [mech. deg] (see Figure 3-4);
- Δ_{rm} is the rotor channel pitch angle in [mech. deg];
- δ is the angle between the cavities and d-axis in Figure 3-5, which is set to a constant 60 mech. deg;
- R_{rot} is the rotor outer radius;
- w_c is the thickness of each cavity. The total thickness of the rotor layers per pole is maintained constant.

The analytical rotor channel volume estimation equations (3-27), (3-28) and (3-29) are obtained by assuming the particular 'V-shaped' rotor cavity. This assumption of rotor channel shape will not impact on the comparison of iron loss when varying the number and positions of cavity layers. Therefore, the conclusion of this work will be generically valid for other rotor-cavity shapes.

These equations are novel and provide accurate results when changing the number of layers over a wide range of values while maintaining the total thickness of these cavities. The analysis in [28] assumed a constant volume for the rotor channels in the iron loss calculation, which is only appropriate for small changes in the number of rotor-cavity layers.

The eddy-current loss is obtained by multiplying the eddy-current loss density in (3-19), (3-20) and (3-24) with the corresponding volume.

The analysis process is summarised in the flow-chart below, which includes the number of key equations.

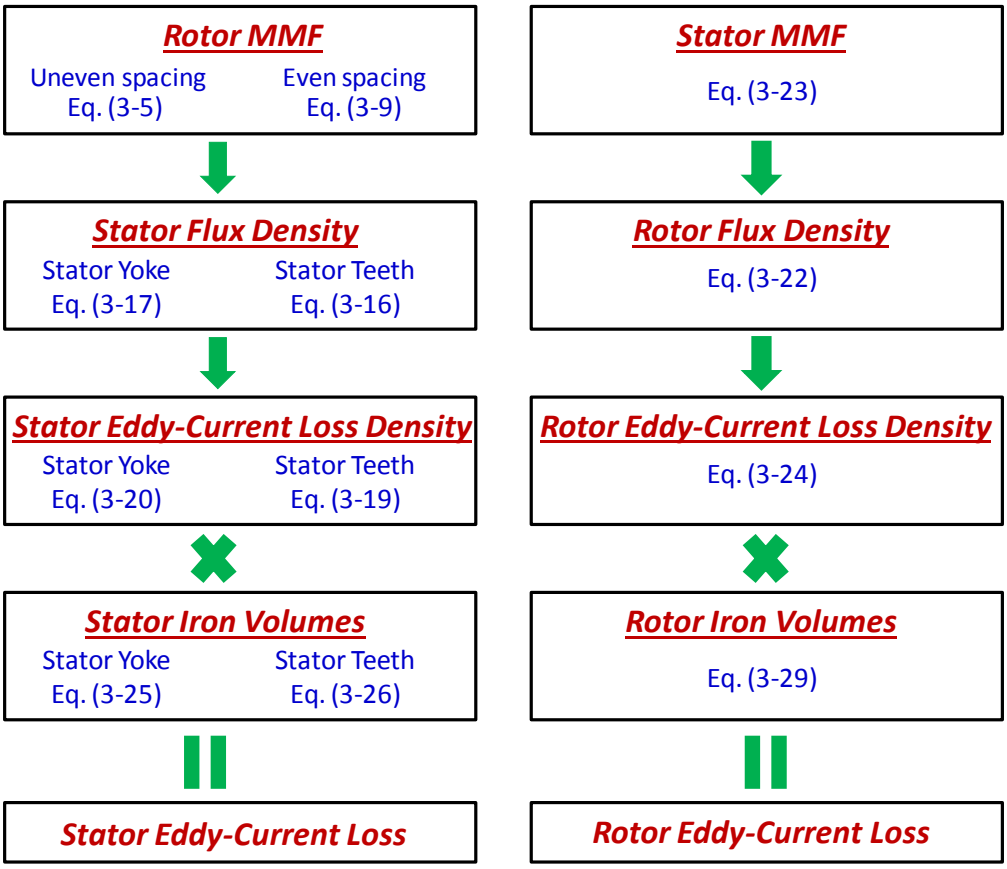

Figure 3-6: Flow-chart of analysis process for the stator eddy-current loss (left) and the rotor eddy-current loss (right)

The novel closed-form analytical expressions described above allow the calculation of the eddy-current loss in watts for the stator teeth, stator yoke and rotor iron for a given value of the eddy-current coefficient. In the next sections they will be used to explore the

effect of the number of rotor layers, the rotor-cavity positioning and the selection of the stator and effective-rotor slot numbers.

It can be seen from the expressions (3-3), (3-5), (3-8), (3-19), (3-20) and (3-24) that the stator teeth, yoke and rotor eddy-current loss is proportional to the square of fundamental stator mmf and hence the square of I_d assuming I_q = 0A. A rated current of 8.6Arms is adopted consistently for all the analytical and FEM results for eddy-current loss.

3.3. Optimisation of Rotor-Cavity Positioning

This section explores effect of the number of layers and their positioning within the rotor on the total eddy-current loss using the analytical equations derived in the previous section. The optimal layer positions resulting in the minimum eddy-current loss are presented.

The following assumptions are used in the analysis. The stator design and the effective-rotor-slot number are kept constant. The total thickness of the rotor barriers per-pole is kept constant in order to obtain a similar value of *d*-axis inductance L_d. The operating current is kept consistent as 8.6Arms for all the designs.

A constant base value is chosen to normalize all the analytical and FEM eddy-current loss results in Sections 3.3 and 3.4. The value chosen is the total eddy-current loss (134W) of the baseline 3-layer reluctance machine (ns18nr12) calculated by FEM with the eddy-current coefficient k_e = 1 at the speed of 3000rpm and rated current of 8.6Arms. The detailed information of the baseline machine (ns18nr12) can be seen from Chapter 5.

Figure 3-7 shows the results of the analysis for 1-, 2- and 3-layered rotors. For each number of layers, there are a number of different alternative designs depending on the location of the layers within the rotor. These are described by the angular position of the layers (e.g. 20/60/80) as shown in Figure 3-2. The top row shows the analytical results based on the closed-form solutions. The second and third rows show the finite-element analysis results for reluctance and IPM machines. In each graph, the bars show the breakdown of losses between the rotor, teeth and yoke. These are discussed in more detail below.

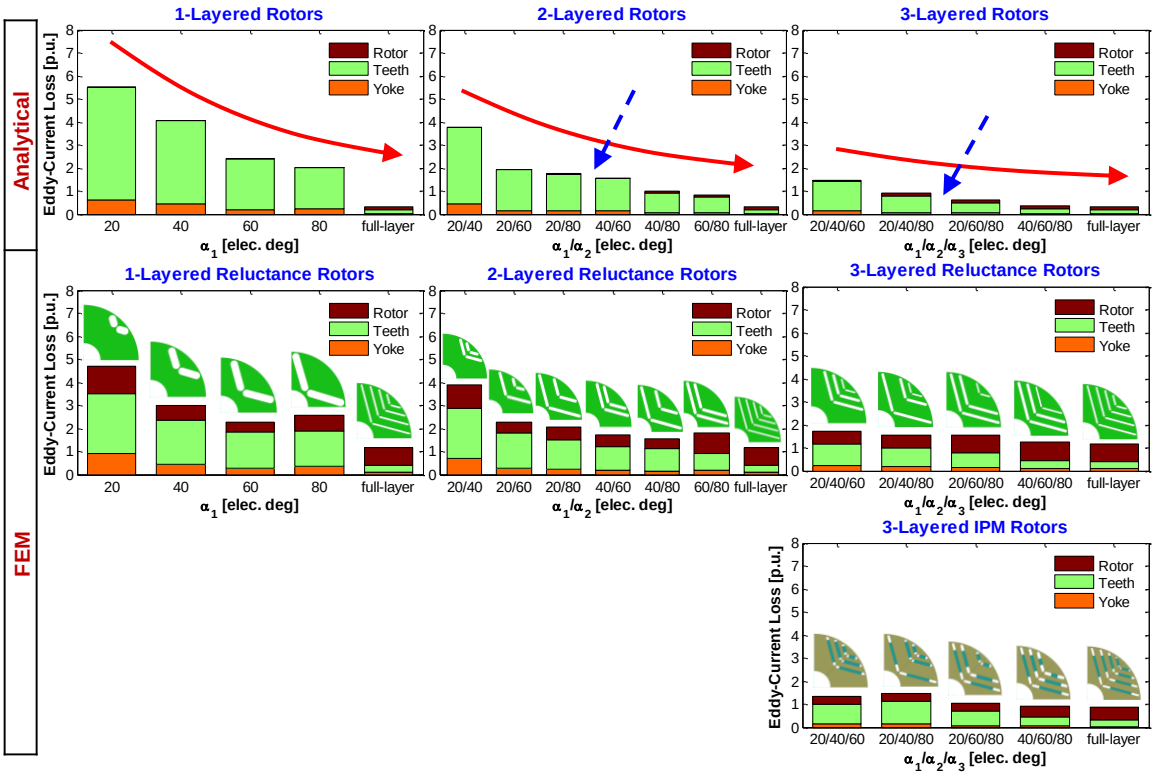

Figure 3-7: The eddy-current loss for all the possible rotor-cavity positionings of the 1-, 2-, 3- and full-layered rotor designs for the stator-slot and rotor-effective-slot number, n_s = 15 and n_r = 18. It shows the analytical prediction (1st row), the FEM reluctance rotors with linear rotor steel and saturable rotor bridges (2nd row) and the FEM IPM rotors with saturable rotor steel (3rd row) at the rated current of 8.6Arms. All results are normalised to a base value of 134W.

3.3.1. Analytical Predicted Eddy-Current Loss

The 1st row in Figure 3-7 shows the analytically predicted eddy-current loss where the effect of the magnets is neglected. The following are some observations on this:

- Stator iron loss decreases with increasing numbers of rotor layers as this reduces the rotor-slot mmf harmonics by making rotor-mmf more sinusoidal. For the same number of rotor layers, stator iron loss drops when placing the cavities deeper inside the rotor.
- Rotor losses due to "tunneling" of the stator-slot harmonics become larger when the number of rotor layers increase and when these layers are closer together. Full-layered rotors generally have the highest rotor losses.

- Stator loss dominates for the 1- and 2-layered rotor designs. Increasing the number of rotor layers to 3 or 4 reduces the stator losses with only a small increase in the rotor loss.

3.3.2. FEM Eddy-Current Loss with Reluctance Rotors

The 2nd row in Figure 3-7 shows the finite-element (FEM) calculated eddy-current loss for the reluctance rotor. The model uses linear steel for the stator and rotor laminations and saturable steel for the rotor ribs. This is because a constant value of current (8.6Arms) was used in order to compare iron loss at the same current for all the reluctance machines. If a saturable steel was used, this current will result in a high degree of saturation for the reluctance machines with lower number of cavity-layers, such as the 1- and 2-layered rotors. However, the same current results in much less saturation for the reluctance machines with 3- and 4-layered rotors.

The trends of the stator teeth and yoke loss changes with rotor layer positioning predicted by the analytical expression matches the FEM results remarkably well considering the simplifying assumptions used in the analysis.

The rotor loss is however considerably under-estimated by the analytical model. The reason for this error for higher numbers of layers is likely due to the flux crossing the cavities being significant when the rotor layers become thinner. Also for 1- and 2-layered rotor designs the rotor surface loss produced by combinations of the airgap permeance variation and stator-mmf harmonics which was neglected, may become significant. The use of linear steel for the rotor iron (except the ribs) in FEM significantly increases the rotor surface loss.

3.3.3. FEM Eddy-Current Loss with IPM Rotors

The 3rd row in Figure 3-7 shows the FEM eddy-current loss for the 3-layered IPM rotors obtained after adding magnet into the 3-layered reluctance rotors in the 2nd row in Figure 3-7.

In this simulation, the linear magnetic steel assumption used in the reluctance machine was removed and high-quality lamination steel (35JN250) with an eddy-current loss coefficient k_e = 1 [W/m^3] was used for the stator and rotor laminations. The total magnet volume was kept constant for all the rotors.

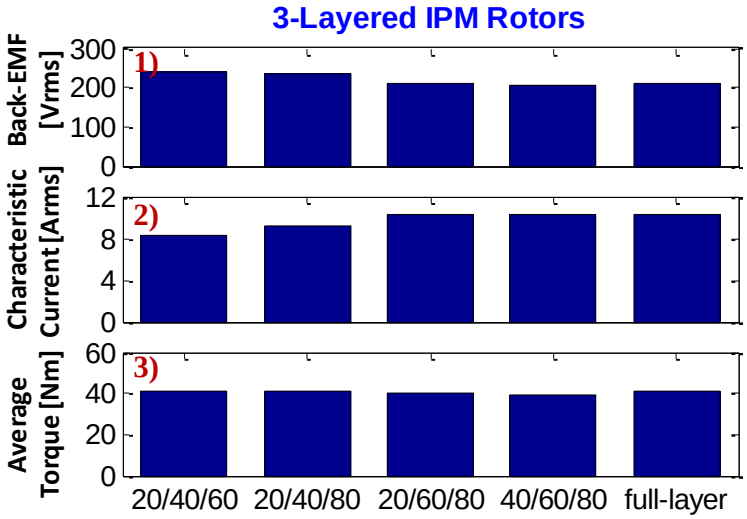

Figure 3-8: FEM analysis for the 3-layered IPM rotors for n_s = 15 and n_r = 18 obtained by adding magnets into the 3-and full-layered reluctance rotors in Figure 3-7, showing: 1) line-to-line back-emf at 1000rpm; 2) characteristic current; 3) maximum average torque with the rated current of 8.6Arms

Figure 3-8 illustrates,

- The back-emf values show less than 5% variation when the rotor-cavity positions varies from "deeply buried" (e.g. 40/60/80) to "close to the surface" (e.g. 20/40/60). The full-layered IPM rotor produced the smallest back-emf.
- The characteristic current has the smallest value when the rotor cavities are closer to the rotor surface. It rises when the rotor cavities are more deeply buried.
- The maximum average torque at the same rated current is nearly identical, within 2%.

The stator eddy-current loss with the IPM rotors in Row 3 of Figure 3-7 are similar to that of the reluctance rotors in Row 2, while the rotor losses with the IPM rotors are approximately half that of the reluctance rotors. This difference in rotor loss is likely due to the reduction in rotor surface losses as a non-linear rotor steel is being used in IPM rotors.

3.4. Optimisation of Stator-Slot and Rotor-Effective-Slot Number Combinations

This section examines the effect on eddy-current loss by changing the stator-slot number n_s and rotor-effective-slot number n_r from the baseline values of n_s = 15 and n_r = 18. The eddy-current loss is calculated by using the closed-form analytical expressions.

3.4.1. Effect of Changing Rotor-Effective-Slot Number

Figure 3-9 extends the analytical eddy-current loss results in Figure 3-7 by keeping the same stator-slot number (n_s = 15) and varying the rotor-effective-slot number (from 4 to 60) with the rotor-cavity positioning corresponding to the minimum total eddy-current loss for each stator-rotor slot combination.

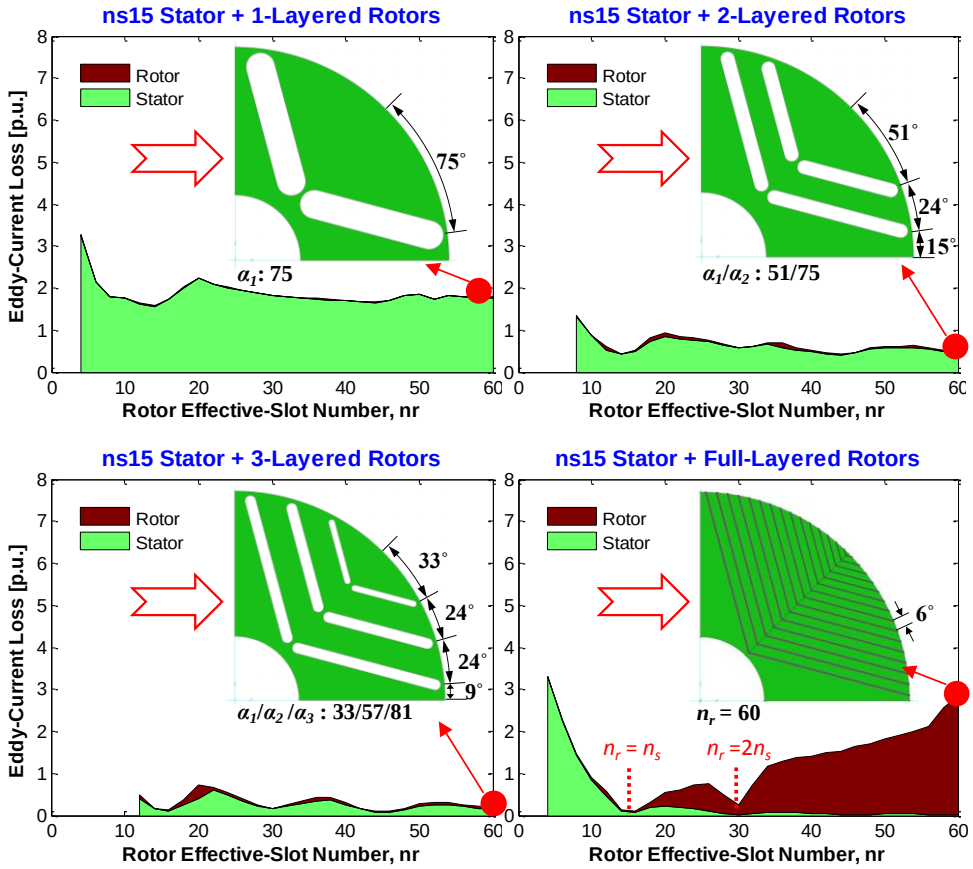

Figure 3-9: The eddy-current loss by keeping the same ns15 stator and varying the rotor-effective slot number with the rotor-cavity positioning for the minimum total eddy-current loss for each stator-rotor slot combination in Figure 3-7 for the 1-, 2-, 3- and full-layered rotors.

Figure 3-9 illustrates,

- The stator loss is generally larger than the rotor loss for 1-, 2- and 3-layered rotors.
- The reduction in stator loss from 1-layered to 2-layered rotors is much larger than from 2-layered to 3-layered rotors.
- The full-layered rotors show a significant increase in the rotor eddy-current loss when the rotor-effective-slot number becomes large. This is consistent with the high rotor loss found with axially-laminated rotor designs [41].

For 1- to 3-layer rotors, the rotor design "converges" to an "optimal rotor layer positioned" design as the effective rotor slot number increases. The cross-section of this design is shown in Figure 3-9 for each number of layers.

3.4.2. Effect of Changing Stator-Slot Number

Figure 3-10 shows the effect of keeping the same rotor-slot number (n_r = 18) and varying the stator slot number (from 6 to 48), with the rotor-cavity positioning corresponding to the minimum eddy-current loss for each stator-rotor combination for the 1- to 3-layered rotors.

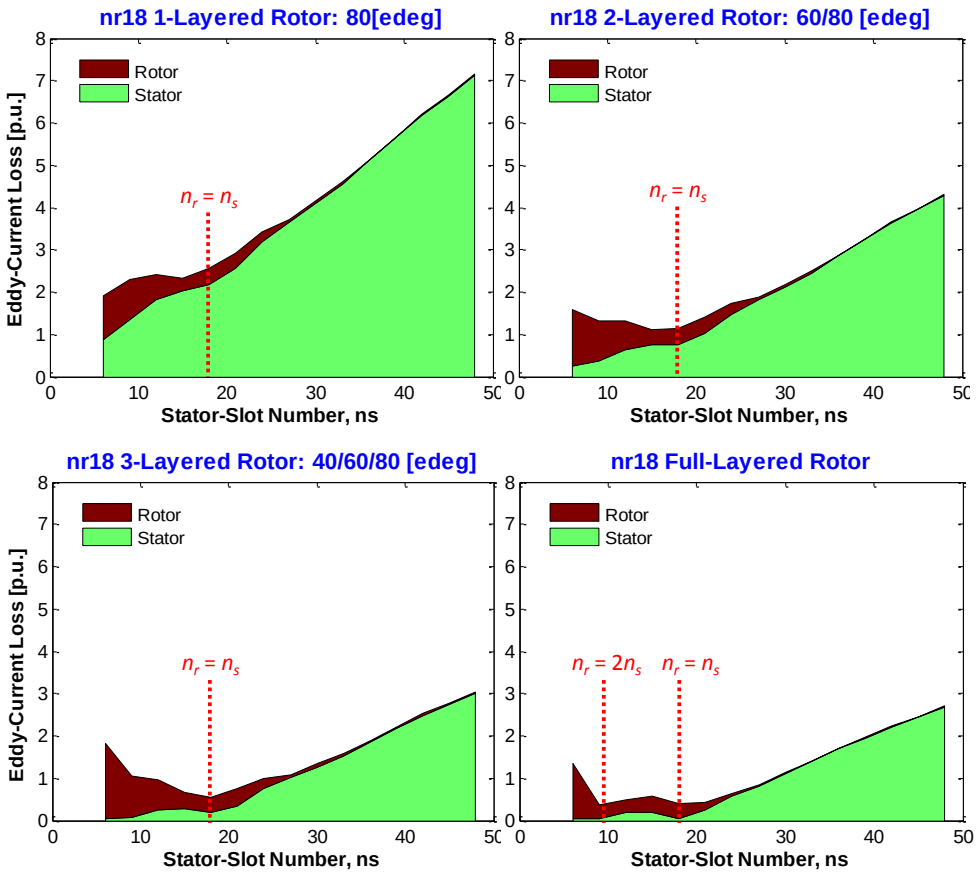

Figure 3-10: The eddy-current loss by keeping the same rotor (nr18) with the minimum eddy-current loss rotor cavity positioning and varying the stator slot number for the 1-, 2-, 3- and full-layered rotors.

Figure 3-10 shows that the stator loss generally increases with the stator-slot number, but shows a local minimum at approximately $n_s = n_r$.

The rotor loss generally drops with increasing stator-slot number, as the spatial wave-length of the stator-slot harmonic mmfs become smaller and become more easily filtered by the rotor channel pitch. In the meantime, the increasingly narrow stator teeth become less effective in filtering the rotor-slot harmonic mmfs, leading to a rapid rise of stator iron loss. The detailed analysis of this filtering effect is shown in Appendix A.

The minimum total eddy-current loss occurs at $n_s = n_r$. However, designs with $n_s = n_r$ have been reported to have high torque ripple [27] which is another aspect to be considered in a practical design.

3.4.3. Effect of Changing Both Stator-Slot and Rotor-Effective-Slot Number

Figure 3-11 shows the eddy-current loss contours obtained by varying both the stator-slot and rotor effective-slot numbers with the minimum eddy-current loss cavity positioning for each stator-rotor combination. Contours for 1 to 3 and full-layered designs are shown.

The stator-slot number is varied from 6 to 48 and the rotor effective slot number is varied from 4 to 60, yielding a total of 435 designs. For each design, the rotor layer positioning to obtain the minimum total loss was found for 1-, 2- to 3-layered designs using the analytical model. Figure 3-11 shows analytically calculated total loss contour plots for these designs as well as for full-layered designs.

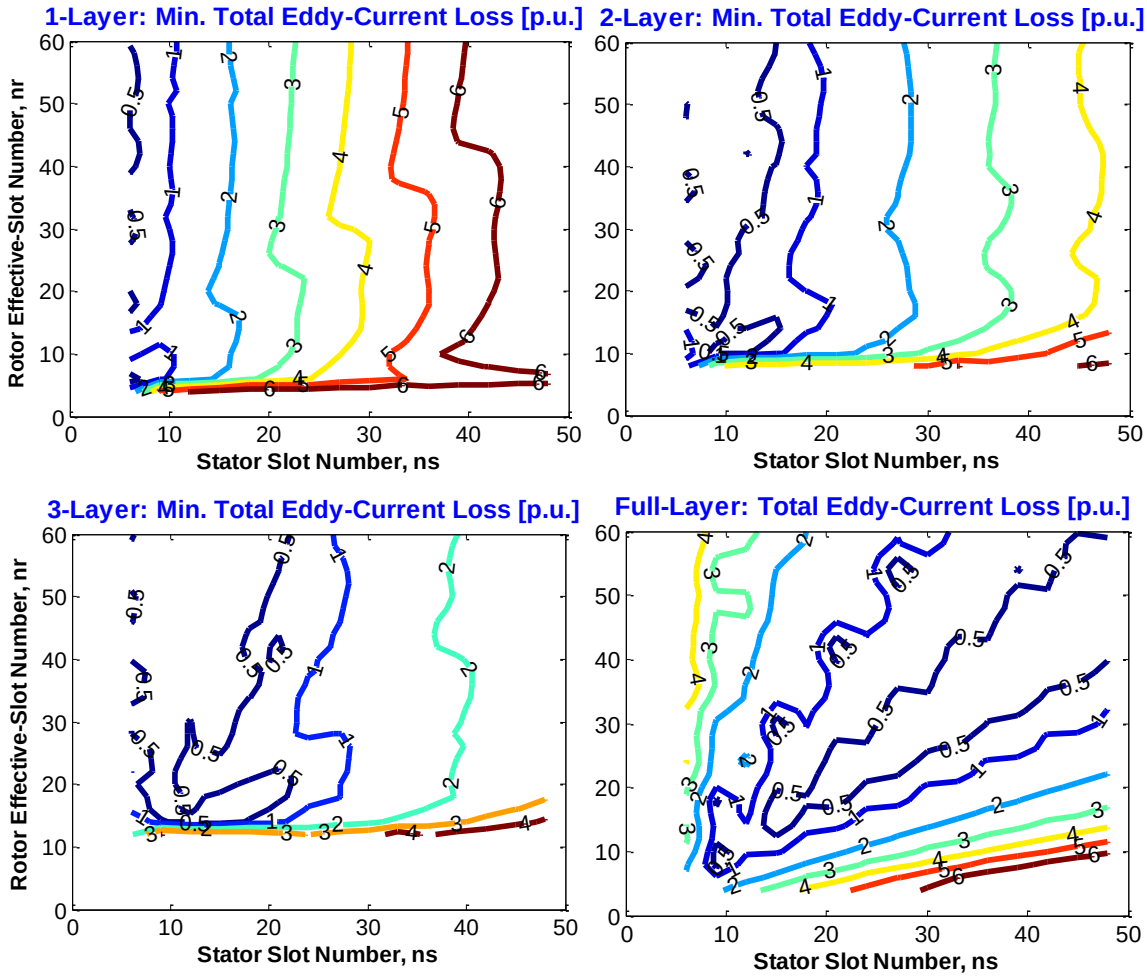

Figure 3-11: The total eddy-current loss contours in a plane of n_r versus n_s, with the minimum total eddy-current loss rotor-cavity positioning for each stator-rotor slot combination showing the results for 1-layered, 2-layered, 3-layered and full-layered rotor designs.

Figure 3-12a compares the 1pu loss contours from Figure 3-11 for the 1- to 3-layered designs. Figure 3-12b shows the 1pu loss contours for the full-layered design. Figure 3-12c shows contours of the rotor to stator-slot number (n_r/n_s) ratio.

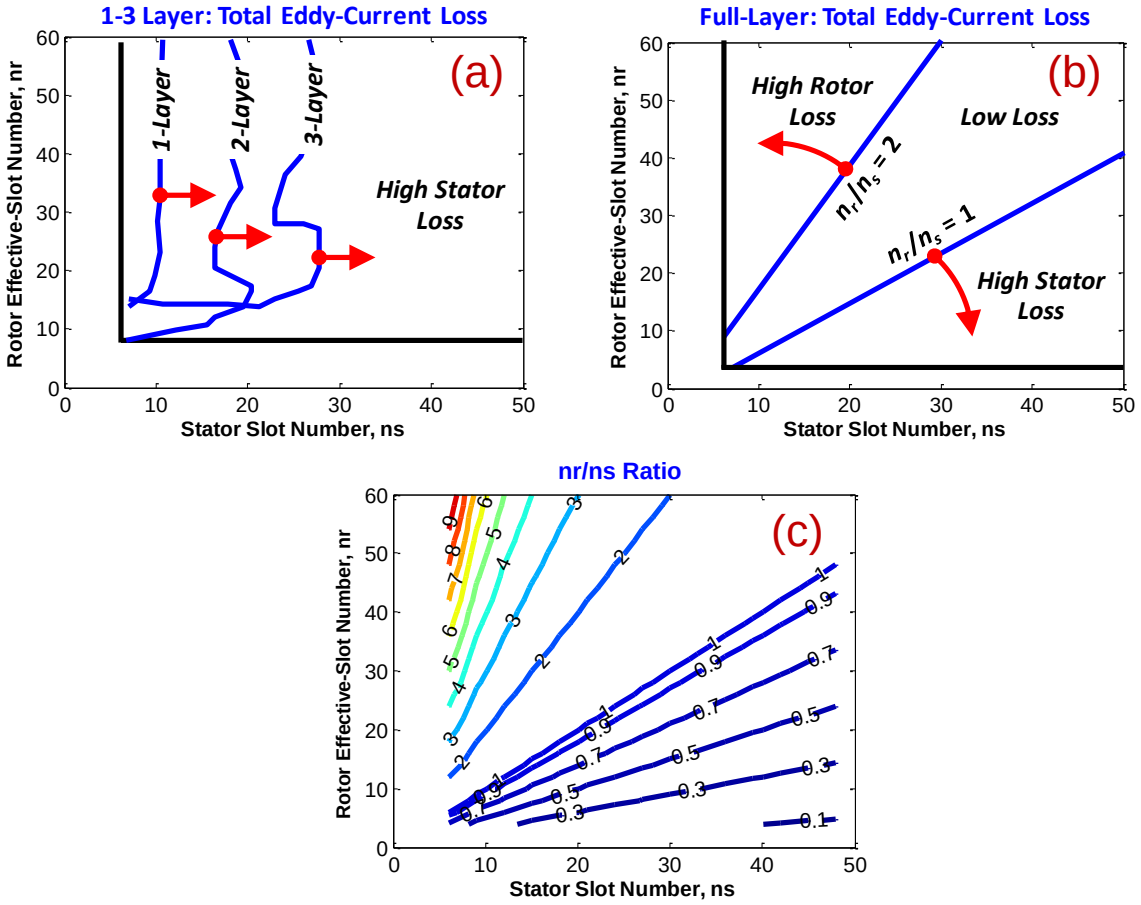

Figure 3-12: The eddy-current loss map in n_s versus n_r for (a) the 1pu loss contours for the 1-, 2- and 3-layered rotors; (b) the 1pu loss contours for the full-layered rotors; and (c) the n_r / n_s ratio contours

The following observations can be obtained from Figure 3-12, with combining the observations from Figure 3-9 and Figure 3-10,

- For the 1- to 3-layered designs, stator loss is dominant. This is generally proportional to the stator slot number n_s and hence the minimum total loss occurs at the lowest number of stator slots.

- The 1pu loss contour moves to larger stator slot numbers with the increase of the number of rotor layers. This means that higher layer number designs have more flexibility in selecting the stator slot number while still keeping a low loss.
- The total loss is sensitive to the rotor effective slot number n_r for 1- to 3-layered designs when n_r becomes small and the design approaches the corresponding full-layered design.
- The full-layered rotor designs have a minimum total loss for designs where the number of effective rotor slots is between n_s and $2n_s$. The eddy-current loss increases when n_r is outside this range.

In summary, the total eddy-current loss is more dependent on the stator-slot number and less dependent on the rotor-effective-slot number for lower numbers of cavity layers. In comparison, the total eddy-current loss is more dependent on the rotor-effective-slot number when the number of cavity layers becomes higher.

3.4.4. Selection of Stator to Rotor Slot Number Ratio

The contour lines of the ratio n_r/n_s are shown in Figure 3-12c. The total loss of the 435 machine design combinations from Figure 3-11 are then plotted versus their n_r/n_s ratio in Figure 3-13 for the different numbers of layers.

Figure 3-13 illustrates with the same n_r/n_s ratio, that the eddy-current loss is reduced by lowering the stator-slot and rotor-effective-slot number. The minimum eddy-current loss occurs with the lowest values of n_s and n_r, and forms the 'minimum loss boundary'. Moving from 1- to 3-layers does not substantially change the minimum loss boundary but does reduce the variation in the total loss between different designs for a given n_r/n_s ratio. The full-layer rotors have the smallest loss variation for a given n_r/n_s ratio but show a significant increase in the total loss for high n_r/n_s ratios due to rotor flux tunneling.

As the full-layered rotors fill all the potential circumferential positions, their rotor loss significantly increases at high n_r/n_s ratio because the number of layers is increasing. In comparison, the machines with 1-, 2- and 3-layered rotors minimize the rotor loss with optimal rotor-cavity positioning for each stator-rotor slot combination, resulting in the reduction of iron loss at high n_r/n_s ratio because the number of layers are not changing but the cavities are being placed more accurately at the minimum loss positions.

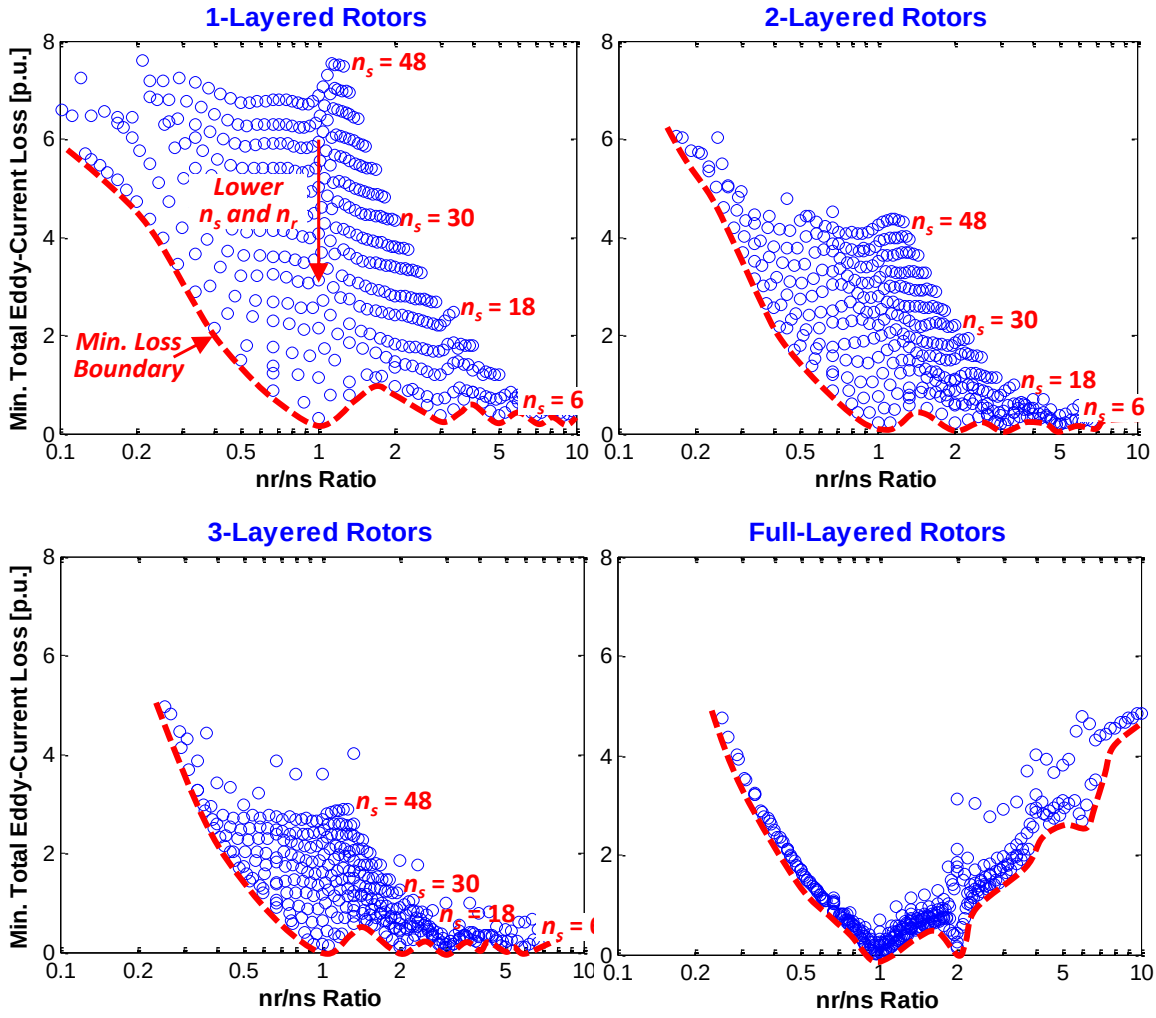

Figure 3-13: The total eddy-current loss versus n_r/n_s ratio for each design with the minimum total eddy-current-loss rotor cavity positioning for each stator-rotor slot combination in Figure 3-10 (shown as circles) showing the 1-, 2-, 3- and full-layered designs.

Figure 3-14 plots the minimum loss boundaries versus the ns/nr ratio for 1-, 2-, 3- and full-layered rotors from Figure 3-13. The stator loss generally dominates with $n_r/n_s < 1$ and the rotor loss increases rapidly with $n_r/n_s > 1$. The figure shows a general low eddy-current loss region with $1 < n_r/n_s < 2$, which is able to keep the total eddy-current loss less than 1p.u. for all the different cavity-layered designs.

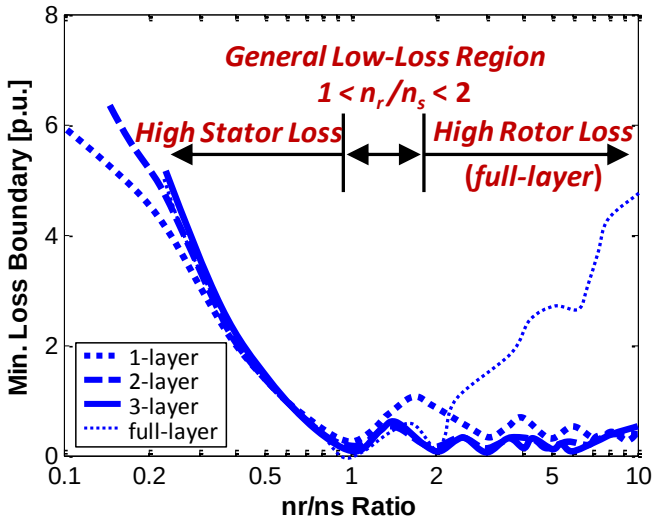

Figure 3-14: The minimum eddy-current loss boundaries in the total eddy-current loss versus n_r/n_s ratio highlighted in Figure 3-13 for 1-layered, 2-layered, 3-layered and full-layered rotor designs

In Figure 3-7, a comparison of the analytical estimates in Row 1 and the finite-element predictions for reluctance machines in Row 2 show a considerable under-estimation of the rotor loss for the 1- to 3-layered rotors.

The sensitivity of the results in Figure 3-13 and Figure 3-14 due to this error was checked by repeating the analysis with a scaling factor of 10 on the analytical rotor loss. It was found that the shape of the minimum-loss boundaries for all cavity-layer numbers remains similar.

This means the conclusions of total eddy-current loss versus n_r and n_s are not sensitive to the under-estimation of the rotor loss. This is likely to be due to the machines considered having distributed windings which have relatively small stator mmf harmonics. The stator iron loss is normally larger than the rotor iron loss for the 1-, 2- and 3-layered rotors, except for the full-layered design where the q-axis tunneling rotor loss increases rapidly with n_r.

3.5. Conclusion

This chapter investigated the rotor-cavity positioning and the combination of stator-slot and rotor-effective-slot number on the eddy-current loss for IPM/reluctance machines operating under deep field-weakening conditions. The major contributions are summarized below.

- New closed-form analytical expressions of the stator and rotor eddy-current loss are developed for IPM/reluctance machines. The expressions apply to distributed windings with fractional and integer SPP values > 1, but it does not apply to SPP values < 1.
- The optimal rotor cavity positioning for minimum total eddy-current loss is presented for 1-, 2- and 3-layered IPM/reluctance rotors.
- The trends of eddy-current loss changes with variations in the stator-slot and rotor-effective-slot number are predicted for 1-, 2-, 3- and full-layered rotors.

The following suggestions are proposed for the design of IPM/reluctance machines to minimize iron loss under deep field-weakening operation.

- Increasing the number of cavity layers leads to a large drop in stator iron loss but a comparatively smaller rise in rotor iron loss, results in a reduced total iron loss in general for 1- to 3-layer rotors.
- For a fixed value of n_r/n_s, reducing the stator-slot number n_s leads to a significant drop in total iron loss for the designs with unevenly displaced rotor cavities, meaning that the minimum iron loss occurs with small stator slot numbers.
- Designs with $1 < n_r/n_s < 2$ were able to keep a low total eddy-current loss in general for all the cavity-layer designs, where the minimum loss occurs at $1 < n_r/n_s \leq 1.2$ and $1.8 < n_r/n_s < 2$. However, designs in this regime have increased rotor iron loss. It is generally more challenging to remove heat from the rotor than from the stator and this may result in increased rotor temperature and reduced magnet flux.
- Designs with $0.8 \leq n_r/n_s < 1$ have comparable total iron loss as those with $1 < n_r/n_s \leq 1.2$, with a greater proportion of this in the stator iron. This may bring the advances by adopting the typical stator cooling strategies such as water jackets and blowing air on fins etc.
- Designs with an integer number of n_r/n_s have the minimum total iron loss if the stator slotting effect is neglected. However, the combinations with n_r equal to a multiple of n_s are usually avoided by designers because of their substantial torque ripple components caused by the product of the stator slot ($k \cdot n_s \pm 1$) and rotor slot ($k \cdot n_r \pm 1$) harmonic mmfs when n_r is the multiple of n_s. Despite of this intrinsic flaw, possible improved designs for these special combinations may be obtained by applying skewing to the stator and rotor laminations.

Chapter 4. FEM Optimization and Experimental Verification

This chapter presents the FEM optimisation and experimental verification of an example interior permanent magnet (IPM) machine design. A baseline 36-slot 4-pole (*SPP* = 3) three-barrier IPM machine with high field-weakening iron losses was considered [34]. An optimized 30 slot, 4 pole (*SPP* = 2.5) three-barrier IPM machine with a significantly reduced iron loss is proposed and compared to the baseline design. This chapter describes the final optimized design and performs a detailed comparison of the optimized and baseline designs using a combination of the analytical model, finite-element method (FEM) and experimental tests.

4.1. FEM Design and Optimisation

The baseline three-layer 36-slot 4-pole IPM machine with n_s = 18 and n_r = 12 is referred to as "ns18nr12". The optimized design is based on an ns15nr18 IPM topology. A rotor barrier effective slot number, n_r =18, which is slightly greater than the stator slot number, n_s = 15, is used to reduce the stator iron loss as described in Chapter 3, while the odd

number of slots per pole pair n_s = 15 generally provides lower torque ripple [35]. The rotors of the above two machines were interchanged to produce two further machine designs for analysis: ns18nr18 and ns15nr12.

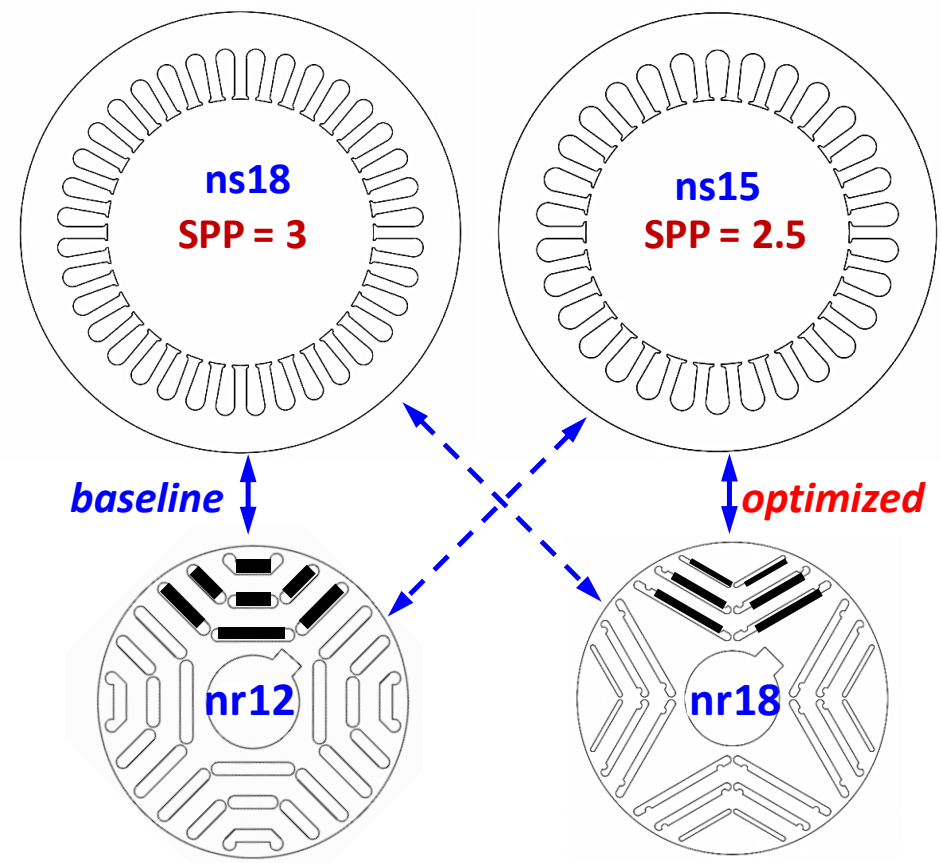

Figure 4-1: Cross-section views of stators and rotors showing the four combinations: the baseline ns18nr12 and the optimized ns15nr18, along with ns18nr18 and ns15nr12 obtained by interchanging the stators and rotors

Table 4-1: General Dimensions for All Test IPM Machines

Number of Rotor Pole	4
Stator ID/OD	92.08/152.4 mm
Airgap	0.39 mm
Stack length	95 mm
Phase Voltage limit	240 Vrms

The general dimensions and number of rotor poles in Table 4-1 are consistent for all IPM machines during the optimization. A rated phase voltage limit of 240 Vrms was used.

Table 4-2 and Table 4-3 include the key parameters for the stators and rotors. The ns15 stator has 300 series turns per phase in comparison to the 282 series turns per phase for the ns18 stator as shown in Table 4-2. This will result in a 6% higher open-circuit flux linkage given the same fundamental airgap flux density, and hence a higher characteristic current assuming the same *d*-axis inductance. The optimized nr18 rotor uses a 30% less magnet than the baseline nr12 rotor, but the B_r of the nr18 rotor magnet is 10% higher than the nr12 rotor magnet. These two aspects will be identified in the next section of experimental verification.

Table 4-2: Parameters for Stators

Parameter	**ns18 Stator**	**ns15 Stator**
Stator slot number	36	30
Stator pole number	4	4
Conductors per slot	47	60
Coils per phase	6	5
Series turns per phase	282	300
Slot packing factor	0.30	0.32
Winding resistance	3.5 Ω	4.4 Ω
Stator laminations	0.35 mm 35JN250	0.35 mm 35JN250

Table 4-3: Parameters for IPM Rotors

Parameter	**nr12 Rotor**	**nr18 Rotor**
Effective rotor slot number	24	36
Rotor pole number	4	4
Rotor laminations	0.35 mm 35JN250	0.35 mm 35JN250
Magnet material	sintered NdFeB	sintered NdFeB
Magnet volume per pole	2.57×10^{-5} m^3	1.81×10^{-5} m^3

The 35JN250 steel of 0.35mm thickness has been used for the prototype machines. The B-H curve in Figure 4-2 shows that the 35JN250 steel starts to saturate at a flux density of 1.4T.

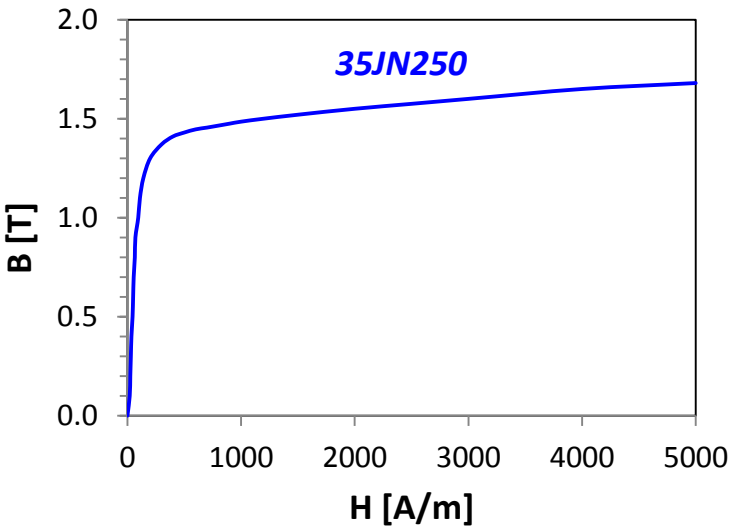

Figure 4-2: The B-H characteristic from the 35JN250 steel datasheet

4.1.1. FEM Design of D-Axis Flux Linkage and Torque

Chapter 3 has shown that the stator eddy-current loss is proportional to the square of the rotor-slot harmonic mmfs f_{rn} ($n = k \cdot n_r \pm 1$, $k = 1, 2, 3\ldots$). As the rotor-slot harmonic mmfs f_{rn} is proportional to the fundamental stator mmf f_{s1} and hence proportional to the total series ampere-turns per phase $f_{rn} \propto N_t I_m$, it ultimately reveals that the stator eddy-current loss is proportional to the square of the total series ampere-turns per phase, $p_{stator\_eddy} \propto (N_t I_m)^2$. Similarly, the rotor eddy-current loss is proportional to the square of the stator-slot harmonic mmfs f_{sh} ($h = k \cdot n_s \pm 1$, $k = 1, 2, 3\ldots$). As the stator-slot harmonic mmfs f_{sh} is proportional to the total series ampere-turns per phase $f_{sh} \propto N_t I_m$, it means that the rotor eddy-current loss is also proportional to the square of the total series ampere-turns per phase, $p_{rotor\_eddy} \propto (N_t I_m)^2$. The $N_t I_m$ values were kept constant in Chapter 3, that is, N_t = 300 turns and I_m = 12.2 Apk (i.e. 8.6 Arms).

During the numerical optimization, the stator outer and inner diameters and axial stack length were kept constant. The characteristic current I_{ch} is maintained at about 12.5 Arms for all the machines as shown in Figure 4-3. The magnet flux linkage per phase for the machines is about 0.6 Vs, which corresponds to an open-circuit phase voltage of 400V at 3,000rpm. The characteristic current I_{ch} is a function of the magnet flux linkage Ψ_m and *d*-axis inductance L_d, expressed as,

$$I_{ch} = \frac{\psi_m}{L_d} \tag{4-1}$$

The characteristic current I_{ch} is critical to the machine's maximum performance capability at the high-speed deep field-weakening condition. In order to obtain a similar characteristic current, the magnet flux linkage Ψ_m and *d*-axis inductance L_d in (4-1) are carefully considered during the FEM design. As $I_q \approx 0$A under deep field-weakening, only the *d*-axis flux linkage versus *d*-axis current characteristic was considered in the FEM design in Figure 4-3.

The average torque at the design operating current is another guideline in the optimization. The total average torque T_{ave} consists of the reluctance T_{mag} and magnet torque T_{rel}, expressed as,

$$T_{ave} = T_{mag} + T_{rel} = 3p[\psi_m I_q + (L_d - L_q) I_d I_q] \tag{4-2}$$

In Figure 4-4, the total average torque and reluctance torque were computed in FEM with and without magnetization of the rotor magnet respectively. The magnet torque was then obtained by subtracting the total average torque by the reluctance torque. A constant current amplitude of 8.6Arms was used for all the machines.

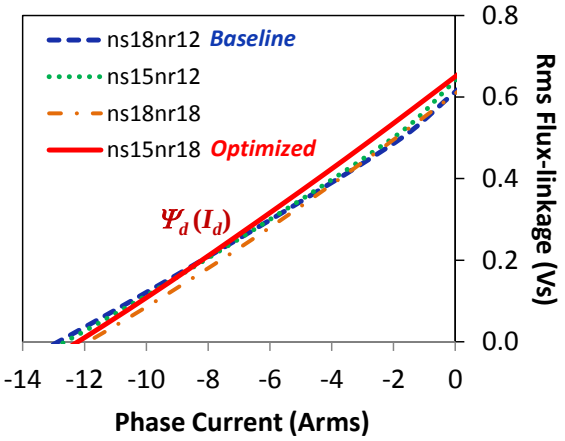

Figure 4-3: FE *d*-axis flux-linkage versus *d*-axis current plot with the initial values of magnet remanence B_r

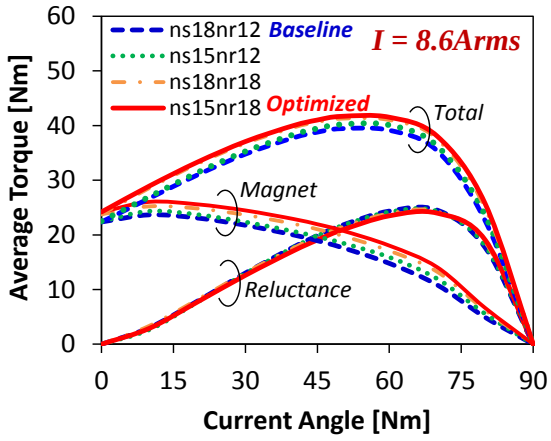

Figure 4-4: FE average torque versus current angle plot with the initial values of magnet remanence B_r; current amplitude was kept constant at 8.6Arms for all the machines

The nr18 IPM rotor was designed to give the same magnetic flux linkage as the nr12 IPM rotor. The initial values of magnet remanent flux density B_r were obtained from the magnet datasheets. The initial magnet B_r used in the optimized nr18 IPM rotor was given as 1.2 T which was about 10% higher than 1.1 T of the baseline nr12 IPM rotor. The ns18 IPM rotor uses 30% less magnet than the ns12 IPM rotor as shown in Table 4-3. This results in the IPM machines with the same stator but different rotors having a similar magnet flux-linkage at zero current, such as ns15nr12 versus ns15nr18 and ns18nr12 versus ns18nr18.

As shown in Table 4-2, the ns15 stator has 300 series turns per phase which is about 6% more than the 282 series turns per phase for the ns18 stator. This results in the magnet flux-linkage of IPM machines with the ns15 stator being 6-7% higher than those with the ns18 stator, such as ns15nr12 versus ns18nr12 and ns15nr18 versus ns18nr18.

The total thickness of the rotor cavities for the nr18 rotor was about 46% less than that of the nr12 rotor. This results in about a 20% higher *d*-axis inductance of the nr18 rotor in comparison to the nr12 rotor. The thinner cavities of the nr18 rotor result in a lower magnet volume than the nr12 rotor as mentioned above.

Figure 4-4 shows that all the machines have similar calculated reluctance torque but that the machines with the nr18 IPM rotor are slightly higher in magnet torque. It is well known that the magnet torque is proportional to the magnet flux linkage, so that the higher magnet flux linkage helps the machines with the nr18 IPM rotor to compensate for the higher *d*-axis inductance, resulting in a similar calculated characteristic current as the machines with the nr12 IPM rotor.

In general, all the IPM machine designs have a similar calculated performance as shown in Figure 4-3 and Figure 4-4.

4.1.2. FEM Design for Iron Loss Reduction

The commercial finite-element package JMAG® was used to calculate the iron loss element by element based on Steinmetz's equation. The hysteresis and eddy-current loss coefficients for the adopted JFE-35JN250 steel were obtained from its iron loss datasheet.

$$p_{iron} = 88 f B_{pk}^2 + 1 f^2 B_{pk}^2 \qquad \left[W / m^3 \right] \tag{4-3}$$

The electric resistivity of the sintered NdFeB magnet was set as 150μΩ·cm [56] for the calculation of the magnet eddy-current loss in FEM. The FEM iron loss of the IPM machines with I_d = -8.6Arms and I_q = 0Arms are shown in Figure 4-5, Figure 4-6 and Figure 4-7.

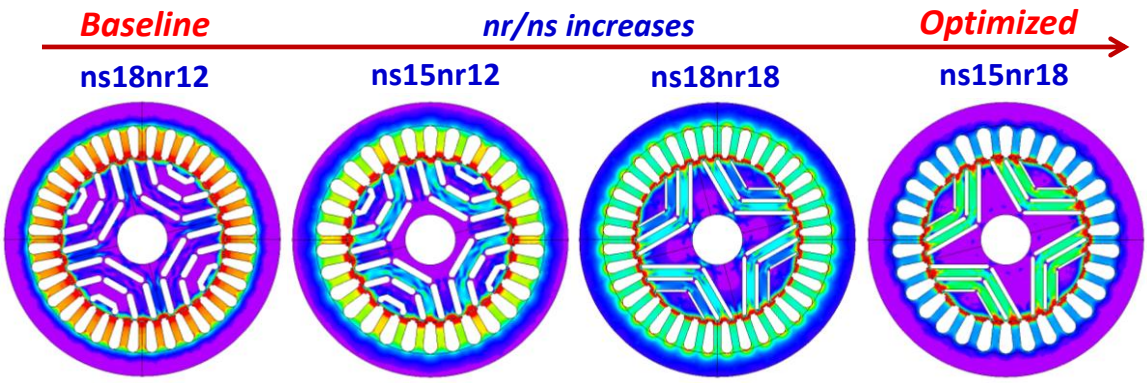

Figure 4-5: FEM iron loss density contours with I_d = -8.6Arms, I_q = 0Arms

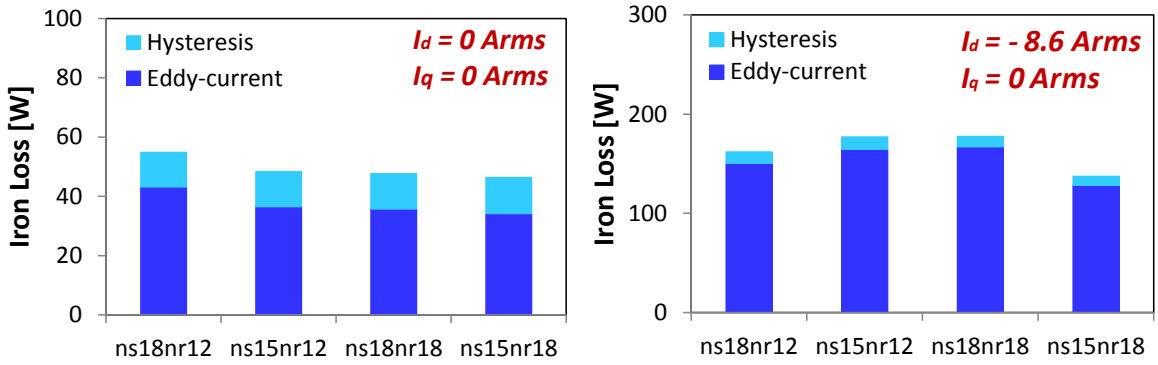

Figure 4-6: FEM eddy-current and hysteresis loss of the IPM machines under the open (left) and short-circuit (right) conditions at a speed of 3,000rpm

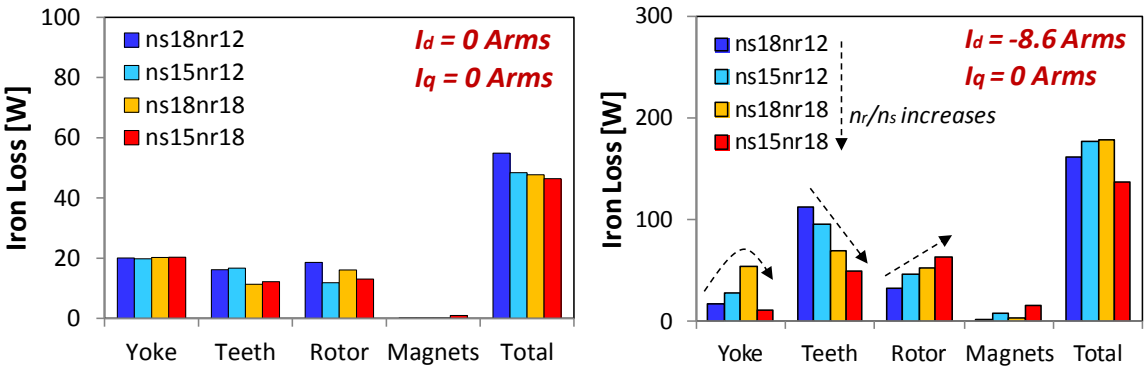

Figure 4-7: FEM iron loss breakdowns for the IPM machines under the open (left) and short-circuit (right) conditions at a speed of 3,000rpm

Figure 4-5 shows the contours of iron loss density, indicating that the location of highest iron loss migrates inwards from the stator to the rotor with increasing n_r/n_s ratio.

In Figure 4-6, it can be seen that the eddy-current loss dominates hysteresis loss under the high-speed deep field-weakening condition.

As shown in Figure 4-7, the optimised design lowered the stator-slot number n_s from 18 to 15, and increased the rotor-effective-slot number n_r from 12 to 18. By doing this, the rotor-slot harmonics $k \cdot n_r \pm 1$ in the rotor-mmf are more easily filtered by the stator teeth and yoke and so the stator iron loss is significantly reduced. Though there would be a small increase in the rotor iron loss, the total iron loss would still be largely reduced under the deep-field weakening condition, as long as the n_r/n_s ratio is close to 1, according to the analysis in Chapter 3.

In Figure 4-7, the stator teeth and yoke has about 79% of the total iron loss for the baseline IPM machine (ns18nr12) under the deep-field weakening condition. After numerical optimisation by FEM, the proposed ns15nr18 IPM design has a significantly reduced stator iron loss under the deep-field weakening (see Figure 4-7), though a slightly increased rotor eddy-current loss due to the increased level of stator mmf harmonics. Nevertheless, the total iron loss (including the magnet loss) of the optimised ns15nr18 machine is reduced to 85% of the baseline ns18nr12 machine under the deep field-weakening and open-circuit condition as shown in Figure 4-7, where the stator and rotor core loss are reduce to 76% under the deep field-weakening.

It can also be seen in Figure 4-7 that the magnet eddy-current loss is relatively small compared to the iron loss. This is because the magnets are buried deeply in the rotor, so that they are well shielded from the limited penetration of the spatial stator-mmf harmonics produced by the distributed windings. The spatial stator-mmf harmonics do however penetrate the outer layer of rotor iron, resulting in a considerable rotor surface iron loss. Figure 4-7, again illustrates that the stator iron loss decreases while the rotor iron loss increases with the n_r/n_s ratio. This matches with the analysis in Chapter 3.

It is found from the FEM parametric study that the airgap permeance variation heavily affects the yoke eddy-current loss. The closer the stator and rotor slot number (i.e. n_s and n_r), the stronger this airgap permeance effect and hence the higher the stator yoke eddy-current loss as shown in Figure 4-7.

4.1.3. FEM Design for Torque Ripple Reduction

The odd stator-slot number n_s avoids the rotor-slot harmonic mmfs f_{rn} ($n = k \cdot n_r \pm 1$, k =1, 2, 3…) coupling with the stator mmf harmonics f_{sn}, resulting in a significant reduction in torque ripple [35]. The torque ripple waveforms for the four machines are calculated by FEM and shown in Figure 4-8. The input current used was 8.6Arms with a current angle γ = 45°.

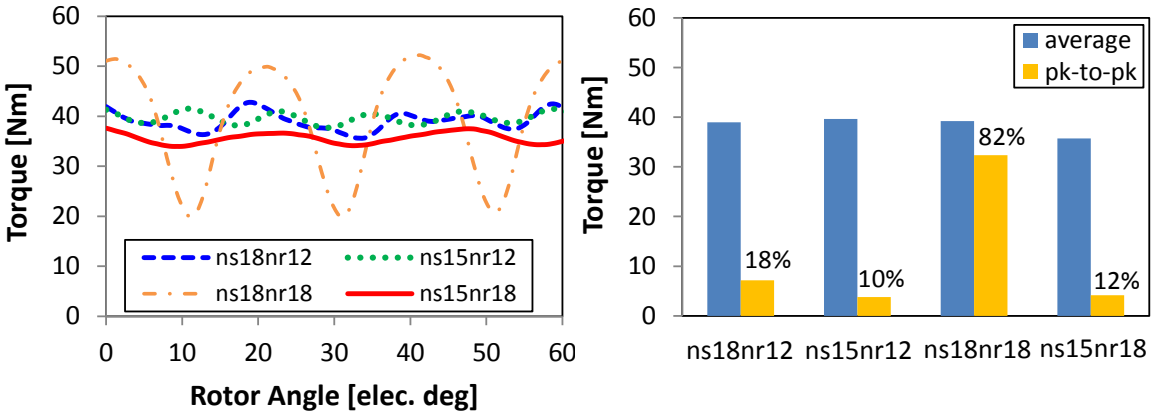

Figure 4-8: The torque versus rotor angle (left) and the average torque and peak-to-peak torque ripple (right) calculated by FEM with I = 8.6Arms, γ = 45°

Figure 4-8 shows that the IPM machines with the ns15 stator generally have much lower torque ripple as the rotor-slot harmonic mmfs ($k \cdot n_r \pm 1$) do not contribute to the torque ripple when n_s is an odd number. The ns18nr18 machine produces the maximum torque ripple because substantial torque ripple components are produced by the product of the stator-slot ($k \cdot n_s \pm 1$) and rotor-slot ($k \cdot n_r \pm 1$) harmonic mmfs when n_r is a multiple of n_s.

In Figure 4-8, the peak-to-peak torque ripple of the optimized ns15nr18 IPM machine is reduced by more than 40% in comparison to the baseline ns18nr12 IPM machine. The ns15nr12 IPM machine has slightly less peak-to-peak torque ripple than the optimized ns15nr18.

4.2. Experimental Verification

Experimental tests were conducted on the baseline (ns18nr12) and optimized (ns15nr18) machines and the two combinations obtained by interchanging the rotors and stators (i.e.

ns18nr18 and ns15nr12). This resulted in test results for four different machines with n_r/n_s ratios varying from 12/18 to 18/15 (see Figure 4-9).

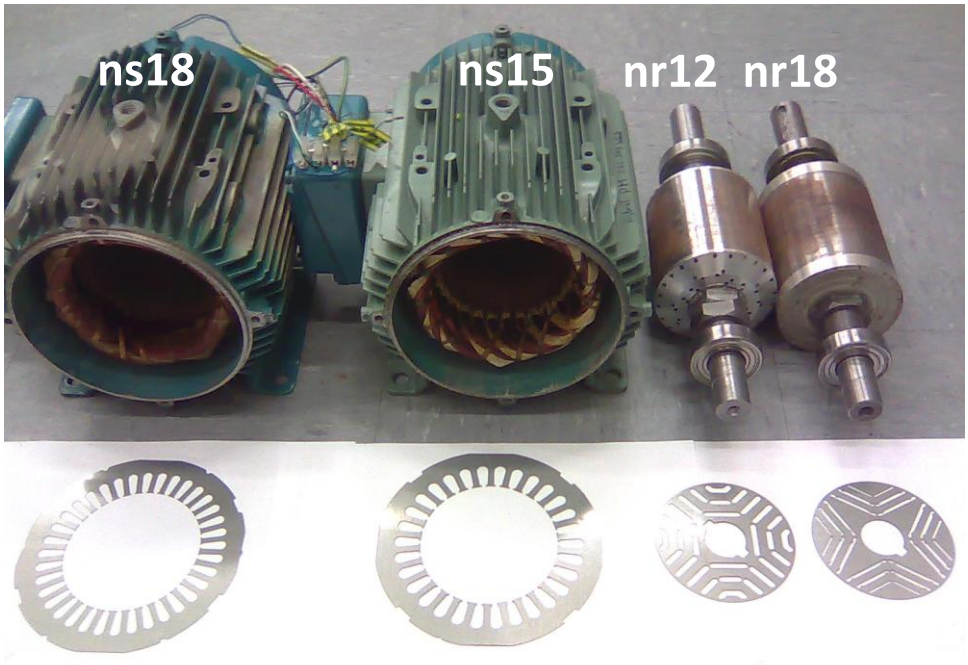

Figure 4-9: The ns18 and ns15 stators, and nr12 and nr18 rotors from left to right

The equivalent circuit parameters were measured in order to predict the performance of the IPM machines. The phase resistance was measured by putting a DC current into the stator winding at room temperature. The *d*-*q* flux linkage $\Psi_d(I_d)$ and $\Psi_q(I_q)$ was measured by the steady-state AC test with the rotor locked to the *d*- and *q*-axis positions [37]. The back-EMF and hence the magnet flux linkage Ψ_m was obtained by measuring the terminal voltage in the open circuit test. With these measured parameters, the machine performance can be predicted with the terminal phase voltage equal to the rated value 240V and 0V (short-circuited).

Infinite constant-power speed range can be obtained when the operating current is equal to the characteristic current I_{ch}. The iron loss under the deep field-weakening condition is similar to the short-circuit condition for IPM machines where $I_d = -I_{ch}$ and $I_q = 0$A [33], [40].

The iron loss was measured in the short circuit and open circuit test. The test results are compared to the analytical and FEM calculations. In the short-circuit test, the input torque and speed were measured to calculate the input mechanical power. The iron loss is

obtained by subtracting the input mechanical power from the measured windage and friction losses (based on testing the stator with a non-magnetized rotor), and the copper loss of the stator winding calculated from the measured stator current.

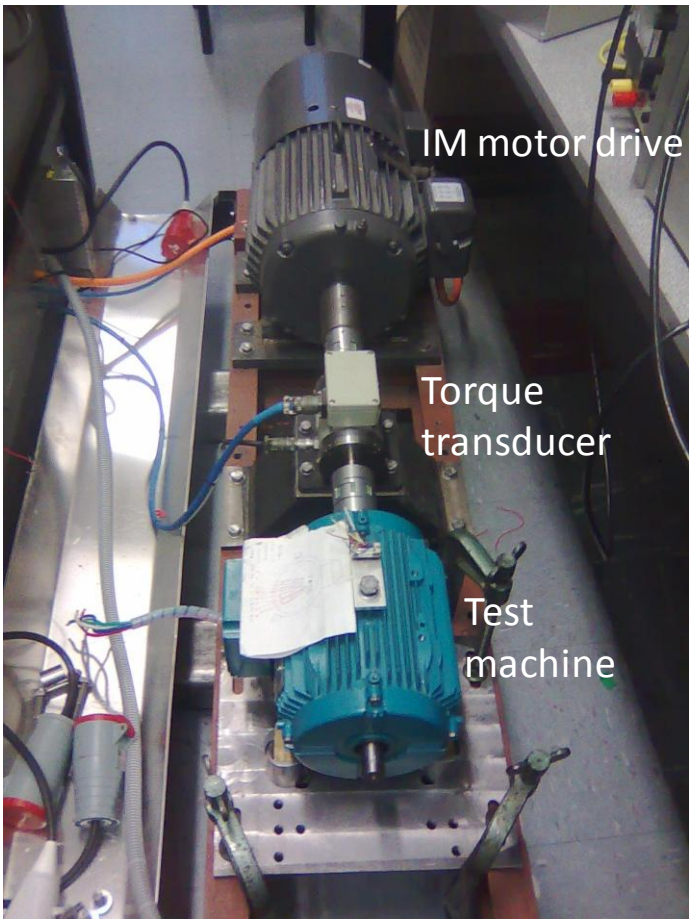

Figure 4-10: The dynamometer setup showing the test IPM machine, torque transducer and induction motor drive

4.2.1. Experimental Verification of FEM Calculated Parameters

This subsection presents the experimental verification of the key parameters calculated by FEM, including the *d-q* flux linkage $\Psi_d(I_d)$ and $\Psi_q(I_q)$ and back-emf E_{ph}.

The initial values of magnet remanent flux density B_r used for FEM modelling are corrected according to the measured back-EMF E_{ph} from the open-circuit test. The *d-q* flux linkage $\Psi_d(I_d)$ and $\Psi_q(I_q)$ calculated from the 2-D FEM will be adjusted by adding the end-winding inductance. The FEM calculated average torque versus current angle

characteristic in Figure 4-4 is compared with the one using the corrected magnet remanent flux density and *d-q* axis inductance.

4.2.1.1. Rotor Magnet Remanent Flux Density B_r

The rms phase back-emf E_{ph} is proportional to the rms magnet flux linkage per phase Ψ_m, expressed as,

$$E_{ph} = \psi_m \cdot \omega_e \tag{4-4}$$

where ω_e is the synchronous frequency in [elec. rad/s].

In Figure 4-11, the back-emf waveforms calculated by FEM after correction of the magnet flux density match the experimental measurements well for both the time waveforms and frequency spectra. The back-emf of the IPM machines with the same rotors but different stators (ns15 versus ns18 stator) satisfy the scaling factor of the number of series turns per phase, i.e. 480V/453V=442V/413V=300/282.

As explained earlier, the difference in back-emf for the IPM machines with same stators but different rotors is due to the lowered magnet remanent flux density and magnet volume of the nr18 IPM rotor in comparison to the nr12 IPM rotor.

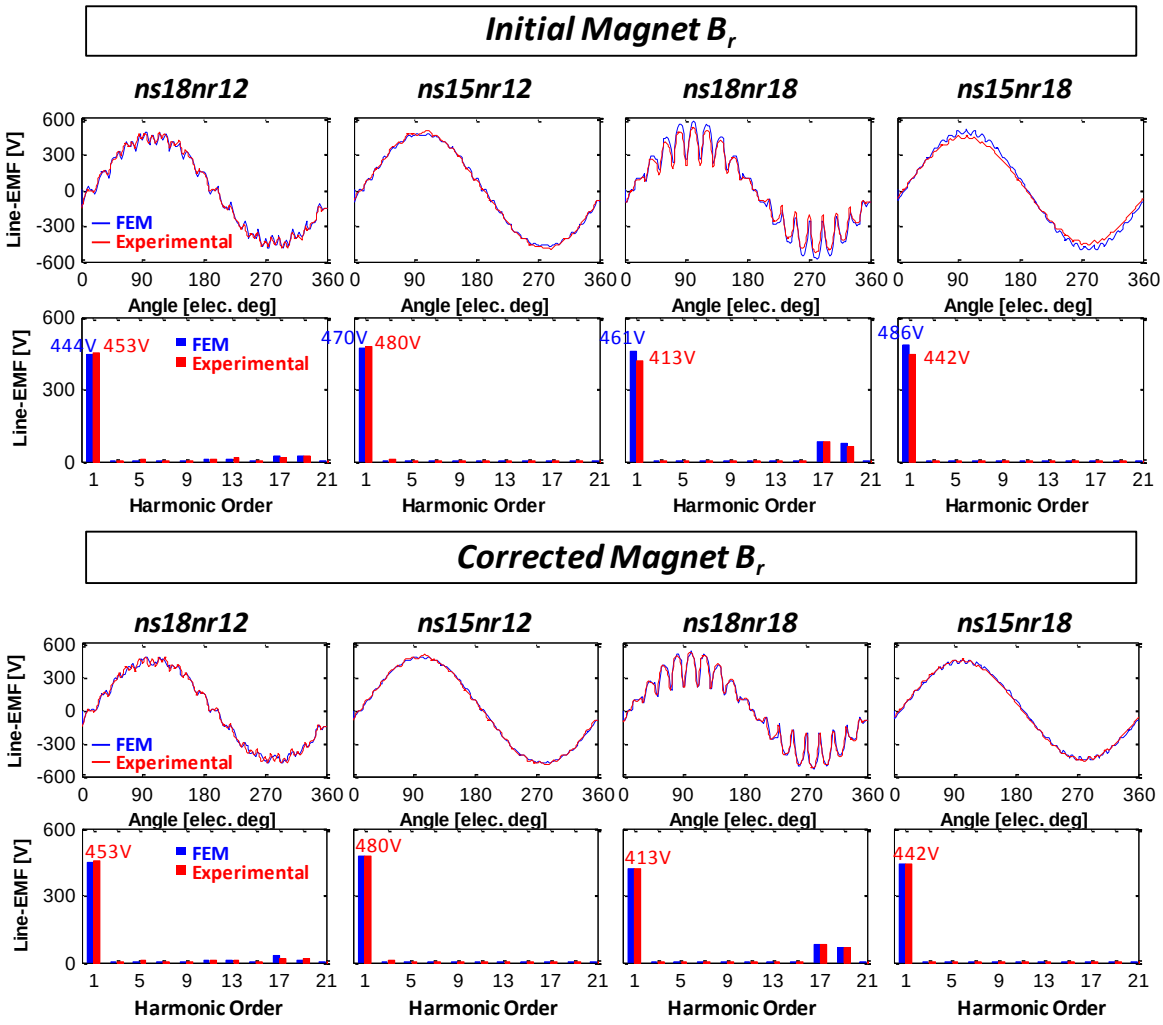

Figure 4-11: Line back-emf waveforms and spectra calculated by FEM with the inital (upper) and corrected (bottom) magnet B_r in comparison to the experimental result at 1,500rpm

A difference between the measured and calculated back-emf magnitudes were found for the machines. This could be caused by combination of a number of reasons including: difference between the actual magnet remanent magnet flux density versus the datasheet value, difference between actual airgap length versus the nominal value and a difference in the thickness of the rotor bridges and their nominal value etc. In this work, the error due to the actual magnet flux density being different its datasheet value is considered to be the primary one, and the other ones are neglected.

The magnet flux linkage Ψ_m increases proportionally with the magnet remanent flux density B_r before saturation occurs as shown in Figure 4-12. The discrepancy in B_r value will affect the FEM result of magnet flux linkage Ψ_m, and hence characteristic current I_{ch}. The initial magnet B_r of nr18 IPM rotor used in FEM optimization was considerably higher

than the actual magnet B_r. This value of B_r needs to be corrected according to the measured back-emf in Figure 4-11.

The optimized nr18 rotor uses 30% less magnet than the baseline nr12 rotor, but the magnet B_r of the nr18 rotor needs to be 9% higher than the ns12 rotor in order to obtain the same magnet flux linkage and hence characteristic current when combined with the same stators. However, the B_r values corresponding to the measured back-emf are generally lower than the initial magnet B_r values used for FEM optimization as shown in Figure 4-12. This discrepancy in magnet B_r needs to be corrected in order to more accurately predict the characteristic current and field-weakening performance for the IPM machines.

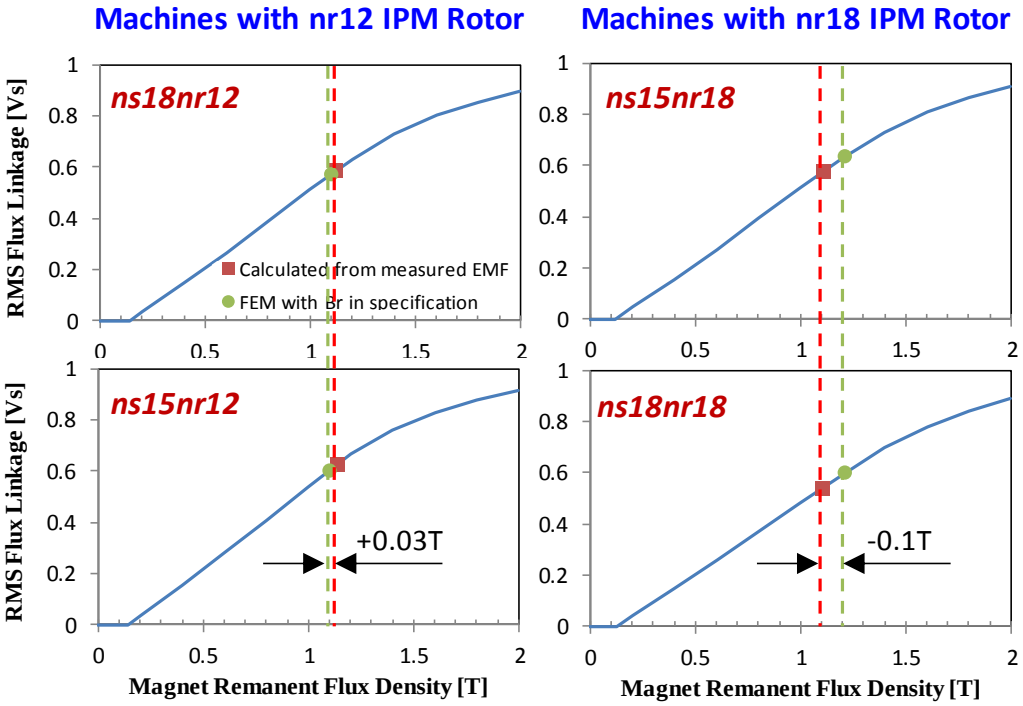

Figure 4-12: Calculated RMS magnet flux linkage versus magnet remanent flux density B_r identifying the discrepancy in given B_r value in specification sheet

Table 4-4: The Correction of Magnet Remanent Flux Density B_r

Magnet Remanent Flux Density, B_r	nr12 Rotor	nr18 Rotor
Initial B_r used for FEM optimization	1.10T	1.21T
Tuned B_r to match measured EMF	1.13T	1.11T
Discrepancy in B_r to tune %	+ 2.7%	- 8.3%

The discrepancies in the magnet B_r affect the open-circuit spatial distribution of airgap flux density and thus the magnet flux linkage Ψ_m. The peak magnet flux linkage as a function of the series turns per phase N_t and the synchronous component of the airgap flux density created by the rotor magnet under open circuit conditions $\hat{B}_{gm1}$ can be expressed as,

$$\hat{\psi}_m = k_{w1} N_t \hat{\Phi}_{g1} = \frac{2\hat{B}_{gm1} l_{stk} r_g k_{w1} N_t}{p} \tag{4-5}$$

where r_g is the airgap radius; k_{w1} is the fundamental (synchronous) winding factor; p is the number of pole-pairs; and l_{stk} is the effective axial stack length which is assumed to be the same as the lamination stack length. The rms magnet flux linkage is expressed as,

$$\psi_m = \frac{\hat{\psi}_m}{\sqrt{2}} = \frac{\sqrt{2}\hat{B}_{gm1} l_{stk} r_g k_{w1} N_t}{p} \tag{4-6}$$

The open-circuit spatial distribution of airgap flux density for the IPM machines with the initial B_r values and the final corrected (tuned) B_r values are shown in Figure 4-13.

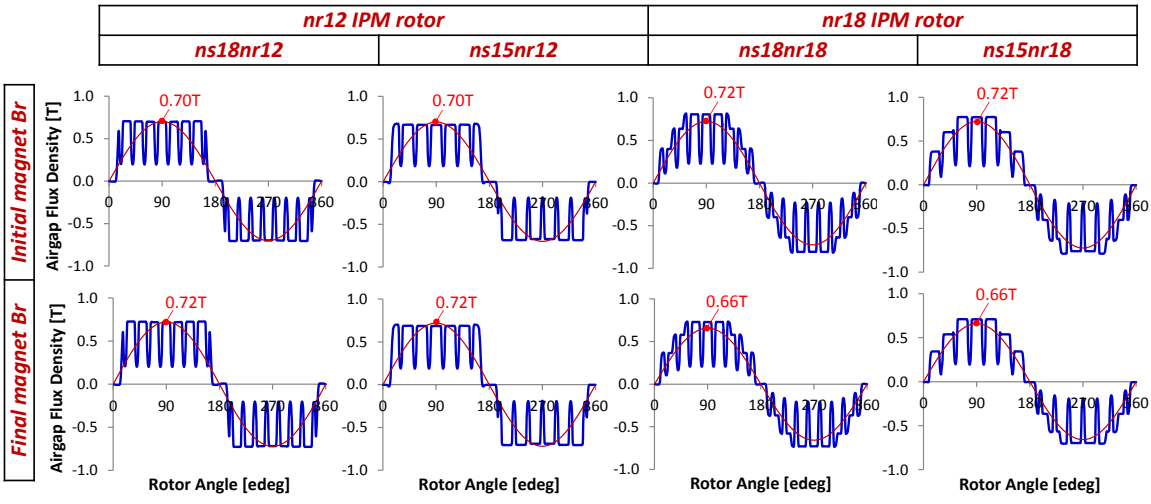

Figure 4-13: The spatial distribution of radial airgap flux density and its synchronous component for IPM machines under open circuit conditions

Figure 4-13 illustrates that machines with the same IPM rotor have the same peak value of synchronous airgap flux density under open circuit as the effective airgap length of these machines are similar.

During the FE optimization with the initial magnet B_r, the nr18 IPM rotor used 9% higher magnet B_r and 30% less magnet volume resulting in a 3% higher synchronous airgap flux density, compared to the nr12 IPM rotor as shown in Figure 4-13. This 3% higher synchronous airgap flux density was intended to compensate for the steeper slope of $\Psi_d(I_d)$ due to the higher L_d of the nr18 IPM rotor, in order to obtain a similar characteristic current to the nr12 IPM rotor.

However, the actual magnet B_r of the nr18 rotor magnet is 8% lower than the initial B_r value in Table 4-3. Accordingly, the synchronous airgap flux density of the actual nr18 IPM rotor is 8% lower than that of the initial magnet B_r as shown in Figure 4-13. As a consequence, the machines with the nr18 IPM rotor have 0.06T (≈8%) less synchronous airgap flux density than the machines with the nr12 IPM rotor. This causes a significant drop in the characteristic current for the machines with the nr18 IPM rotor.

By substituting (4-6) into (3-1), the rms characteristic current I_{ch} can be expressed as,

$$I_{ch} = \frac{\sqrt{2}\hat{B}_{gm1} l_{stk} r_g k_{w1} N_{ph}}{p L_d} \tag{4-7}$$

The lowered B_r of the actual rotor magnet caused a significant decrease of the characteristic current I_{ch} of the machines with the nr18 IPM rotor as shown in Figure 4-14 in comparison to Figure 4-3. The discrepancy in the characteristic current which is caused by the difference in total series turns per phase for the ns15 and ns18 stators with the same rotors is small in Figure 4-14 and can be ignored. Figure 4-15 shows that the magnet torque for the IPM machines is more similar than the initial designs in Figure 4-4. This shows that the proposed ns15nr18 machine still met the rated torque and power specification as the baseline design ns18nr12, even though the magnet B_r of the new design is less than its design value.

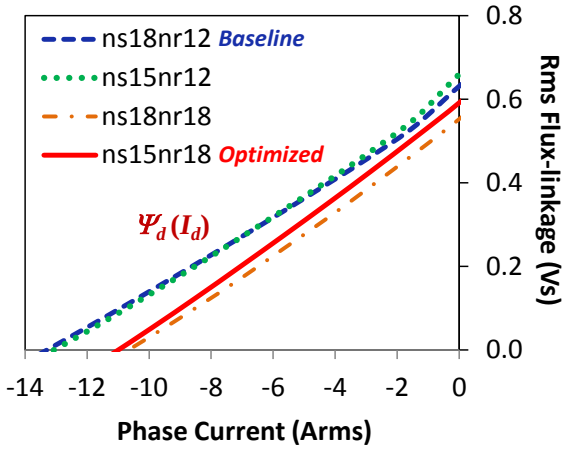

Figure 4-14: FE *d*-axis flux-linkage versus *d*-axis current plot for the IPM machines with the tuned magnet B_r

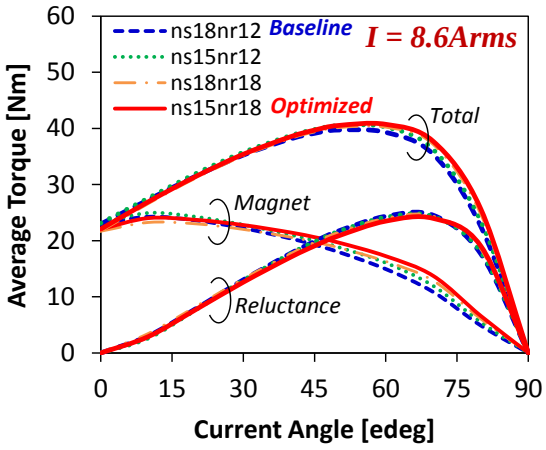

Figure 4-15: FE average torque versus current angle with tuned magnet B_r; current amplitude was kept constant 8.6Arms for all machines

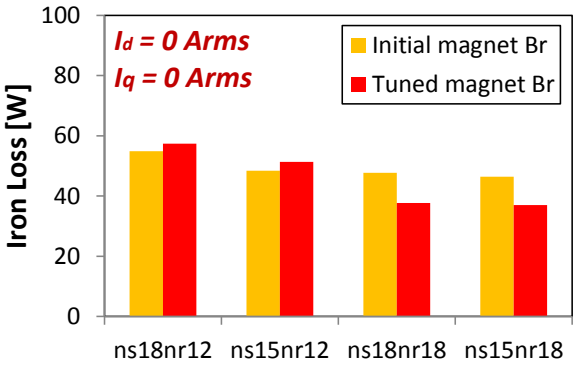

Figure 4-16: FE total iron loss for IPM machines under open circuit comparing results with the initial and tuned magnet B_r

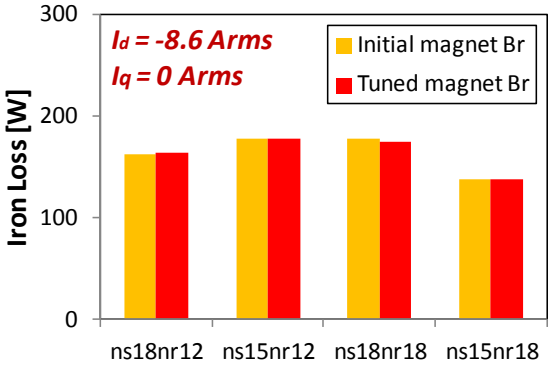

Figure 4-17: FE total iron loss for IPM machines with I_d = -8.6Arms and I_q = 0Arms comparing results with the initial and tuned magnet B_r

The difference between the initial and tuned magnet B_r values results in a significant drop of the characteristic current for the nr18 IPM rotor as shown in Figure 4-14, but it has little effect on the iron loss under the same current as shown in Figure 4-17. This confirms the assumption in Chapter 3 that a machine with/without the magnet have a similar iron loss at a same current under the deep field-weakening condition. In contrast, the difference of magnet B_r has much larger effect on the open-circuit iron loss, especially for the machines with the nr18 IPM rotor as shown in Figure 4-16.

4.2.1.2. Stator End-Winding Inductance L_{end}

The end-winding inductance L_{end} is obtained by subtracting the AC inductance test result with no rotor from the 2-D FEM inductance with no rotor. The FEM models can be

then corrected by adding this external inductance to the three phases to simulate the effect of stator end-winding inductance.

Table 4-5: Estimation of Stator End-Winding Inductance

No-rotor Inductance	ns18 Stator	ns15 Stator
AC inductance test with no-rotor [mH]	21.2	23.0
2-D FEM inductance with no-rotor [mH]	14.3	15.4
Stator end-winding inductance L_{end} [mH]	6.9	7.6

The *d-q* flux linkage Ψ_d (I_d) and Ψ_q(I_d) were measured from the stand-still rotor test with an AC voltage input [37]. During the test, two terminals of the phase B and C windings were shorted together. A variable-magnitude AC voltage was applied to the phase-A and phase-B(C) terminals. The instantaneous terminal voltage and current are recorded. The instantaneous flux linkage was obtained by integrating the internal voltage which equals the terminal voltage after subtracting the voltage drop due to the winding resistance. The flux-linkage versus current characteristic measured from the test included the saturation impact of the *d*- and *q*-axis. The FEM *d-q* flux linkage with the corrected magnet B_r value and including the stator end-winding inductance is compared to the experimental results as shown in Figure 4-18.

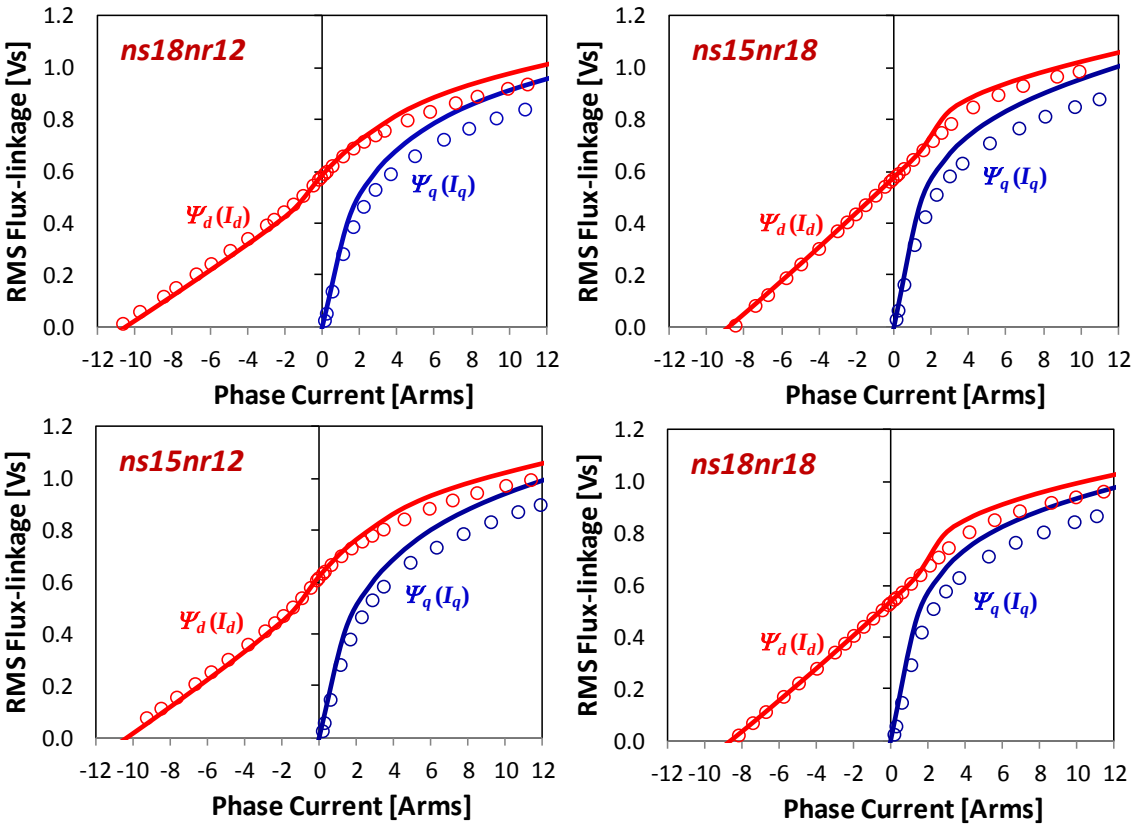

Figure 4-18: Flux linkage versus current for *d*- and *q*-axis for four IPM machines showing the comparison of corrected FEM and experimental measurements

In comparison to Figure 4-14, Figure 4-18 shows that the increased *d*-axis inductance L_d by including the end-winding inductance generally reduces the FEM characteristic current by 2Arms for all machines. The FEM *d*-axis flux linkage $\Psi_d(I_d)$ with the corrected magnet B_r and stator end-winding inductance matches well the experimental measurements as shown in Figure 4-18. The measured magnet flux linkage and characteristic current are summarized in Table 4-6.

Table 4-6: Measured magnet flux linkage and characteristic current for IPM Machines

	ns18nr12	ns15nr12	ns18nr18	ns15nr18
RMS magnet flux linkage, ψ_m [Vs]	0.59	0.63	0.54	0.58
D-axis inductance with $I_d = I_{ch}$, L_d [H]	0.054	0.057	0.062	0.067
Q-axis inductance with $I_q = 0$, L_q [H]	0.24	0.26	0.26	0.28
Characteristic current, I_{ch} [Arms]	10.9	11.0	8.6	8.6

Table 4-6 shows the measured characteristic current of machines with the same rotors are very close. This further proves that the actual magnet flux density being different its

datasheet value is the primary reason for the error in the measured back-EMF as mentioned above.

The total average torque in (4-2) can be also expressed as a function of the *dq*-axis flux linkage Ψ_d and Ψ_q,

$$T_{ave} = 3p[\psi_d I_q - \psi_q I_d] \tag{4-8}$$

where,

$$\begin{cases} \psi_d = \psi_m + L_d I_d \\ \psi_q = L_q I_q \end{cases} \tag{4-9}$$

The average torque can be calculated by using the measured *dq*-axis flux linkage $\Psi_d(I_d)$ and $\Psi_q(I_d)$ in Figure 4-18 and equation (4-8) as shown in Figure 4-19. The cross-coupling effects are neglected. Two cases of current limit are considered in Figure 4-19, firstly that the operating current equals their characteristic current and secondly that a constant value of 8.6Arms is used.

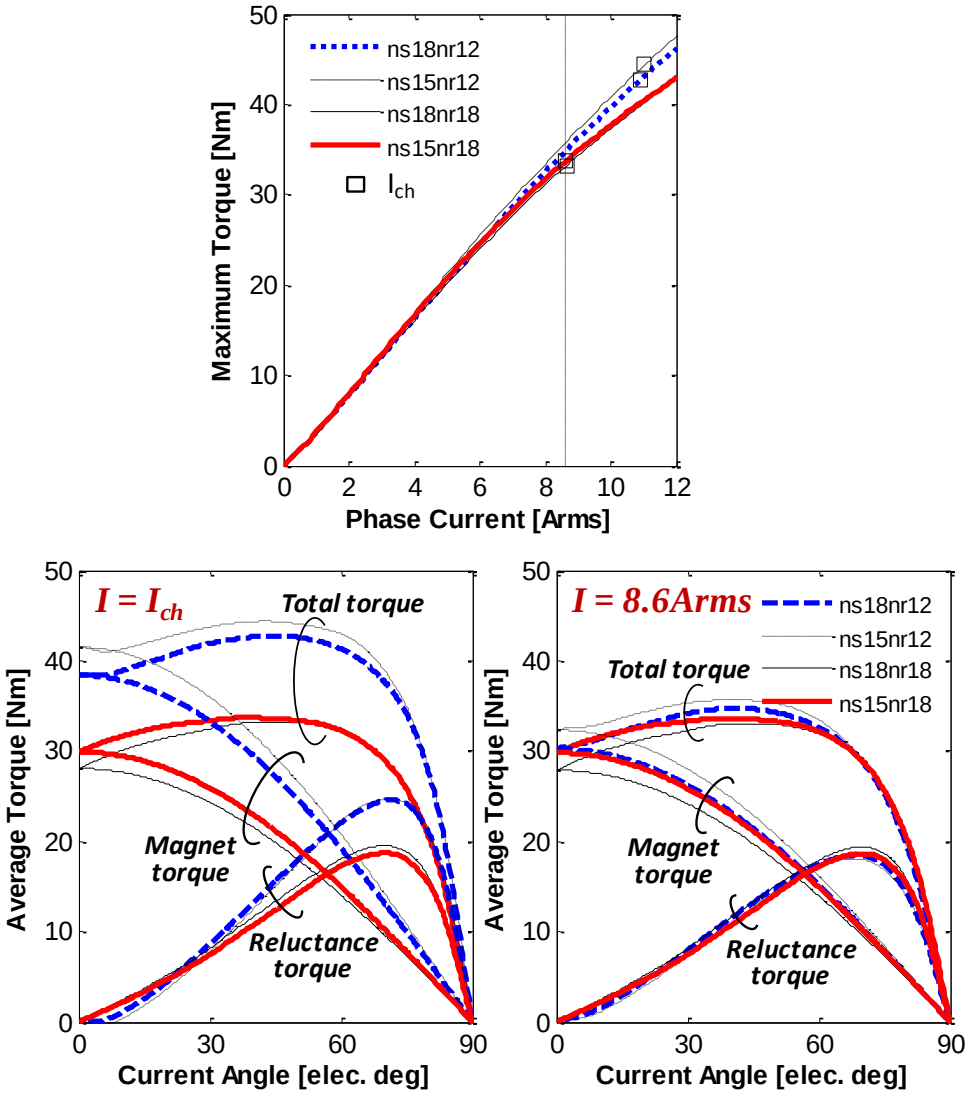

Figure 4-19: The calculated maximum torque as a function of current (left), average torque versus current angle with an operating current equal to characteristic current (middle) and constant 8.6Arms (right), with the tuned values of magnet remanence B_r and including the end-winding inductance for the IPM machines

It can be seen in Figure 4-19 that the maximum average torque increases nearly linearly with the operating current. The characteristic current of the machines with the nr18 IPM rotor is about 20% lower than those with nr12 IPM rotor. The average torque of the machines with nr18 IPM rotor with an operating current equal to the characteristic current is 20% less accordingly. For the case with the constant current of 8.6Arms, the reluctance torque of all the machines is very close and also the baseline (ns18nr12) and optimized (ns15nr18) machine have similar magnet torque and hence total average torque.

4.2.1.3. Field-Weakening and Short-Circuit Performance

The performance of an IPM machine can be predicted using the equivalent circuit in Figure 4-20 by applying the measured nonlinear *dq*-axis inductance (or flux linkage in Figure 4-18) with an iterative procedure. It is worthwhile noting that the *dq*-axis inductance L_d, L_q in Figure 4-20 includes the stator end-winding inductance L_{end}.

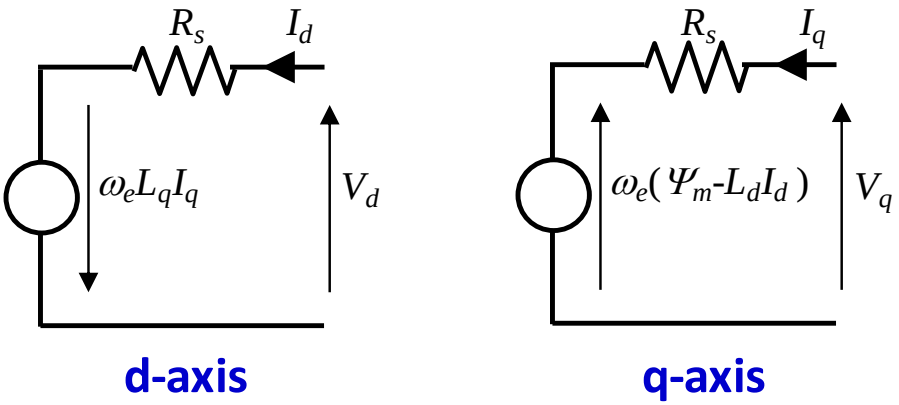

Figure 4-20: *dq*-axis equivalent circuit for an IPM machine

The terminal voltages V_d and V_q in Figure 4-20 are zero under the short circuit condition. Then, the equivalent circuit can be expressed as,

$$\begin{cases} R_s I_q = \omega_e \psi_m - \omega_e L_d I_d \\ R_s I_d = \omega_e L_q I_q \end{cases} \tag{4-10}$$

Substituting I_d and I_q solved from (4-10), the total short-circuit current I_{sc} can be obtained as,

$$I_{sc} = \sqrt{I_d^2 + I_q^2} = \frac{\omega_e \psi_m \sqrt{\omega_e^2 L_q^2 + R_s^2}}{R_s^2 + \omega_e^2 L_d L_q} \xrightarrow{\omega_e \uparrow} \frac{\psi_m}{L_d} = I_{ch} \tag{4-11}$$

From (4-11), the short-circuit current approaches the characteristic current at high speed when the small impact of the stator resistance can be neglected. This can be seen from the short-circuit *dq*-axis current trajectories in Figure 4-21. The field-weakening performance is also shown in Figure 4-21 with a terminal phase voltage of 240V and

operating current equal to the characteristic current in order to obtain infinite speed range under field-weakening.

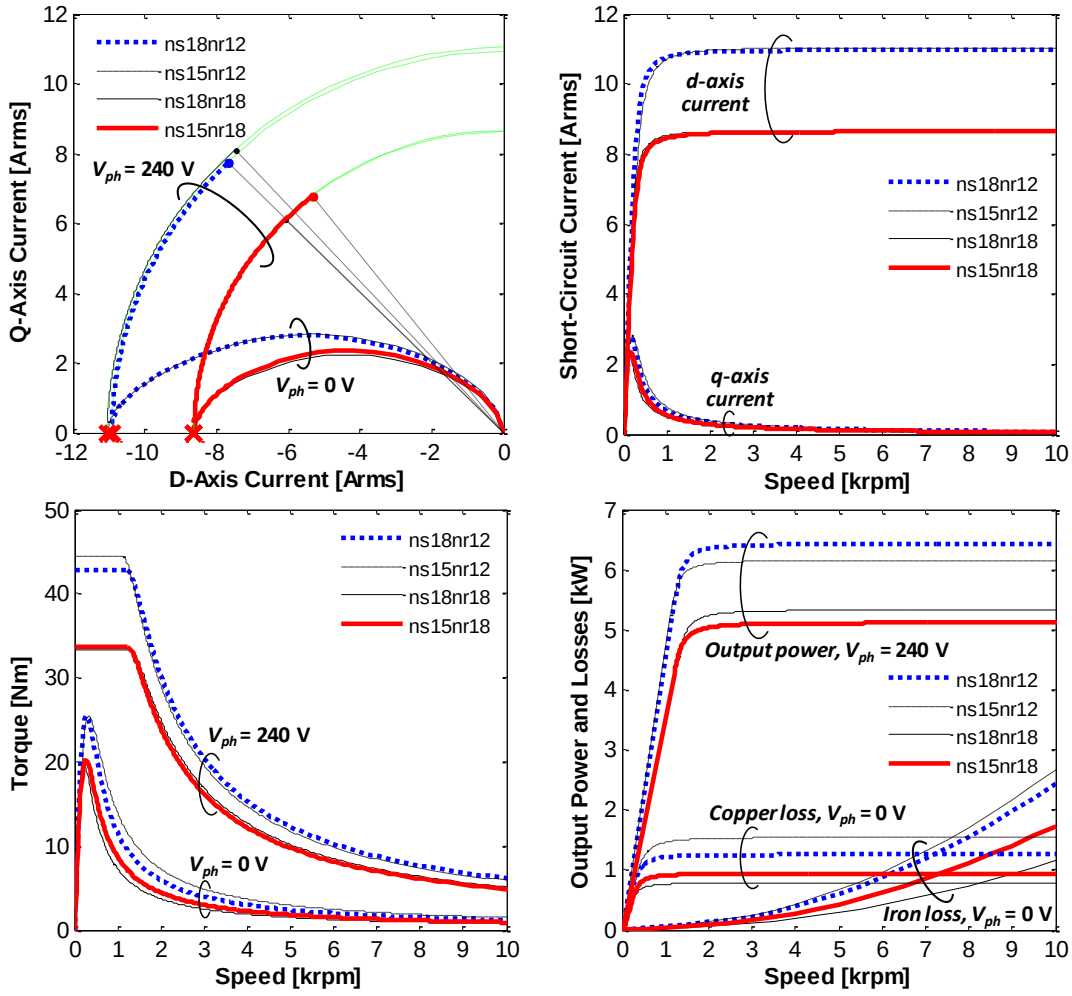

Figure 4-21: Predicted performance of IPM machines operating under short-circuit (V_{ph} =0V) and field-weakening (V_{ph} =240V) conditions showing the *dq*-axis current (top graphs), torque versus speed (bottom left) and power and losses versus speed (bottom right)

Under the short circuit (V_{ph} =0V) condition, the *d*-axis current approaches the characteristic current while the *q*-axis current approaches to zero at high speeds as shown in Figure 4-21. The *dq*-axis current trajectories for short circuit (V_{ph} =0V) and field weakening (V_{ph} =240V) converge towards the point of $I_d = I_{ch}$ and $I_q = 0$ at the high speeds above 1000rpm. The machines with the nr12 IPM rotor produce higher torque and power under field weakening due to their higher characteristic current, in comparison to the machines with the nr18 IPM rotor. With the operating current equal to the characteristic

current, infinite field-weakening speed range (or constant-power-speed-ratio) is obtained which is manifested in the flattened high-speed power versus speed curves.

The copper loss was calculated from the stator current as $3I^2R_s$. The difference in copper loss for the machines with same IPM rotors was caused by the different resistance for the ns18 and ns15 stators (see Table 4-2) while the short-circuit current for them are similar (see Table 4-6).

Under the short-circuit condition, the copper loss stays constant when the short-circuit current approaches the characteristic current above 1,000rpm. In contrast, the iron loss increases approximately with the square of speed because the eddy-current loss is proportional to the square of frequency. When moving along the torque versus speed envelope, the copper loss dominates the iron loss at low speed (< 6,000rpm) while the iron loss becomes larger than the copper loss at high speeds (> 9,000rpm).

4.2.2. Iron Loss Segregation for Open- and Short-Circuit Tests

The windage and friction loss was measured using an induction rotor combined with the ns15 and nr18 stators. The induction rotor has a similar weight as the IPM rotor, and the same bearings were used. The measured windage and friction loss are shown in Figure 4-22. Figure 4-22 shows that the difference in slot number has only a small effect on the windage and friction loss.

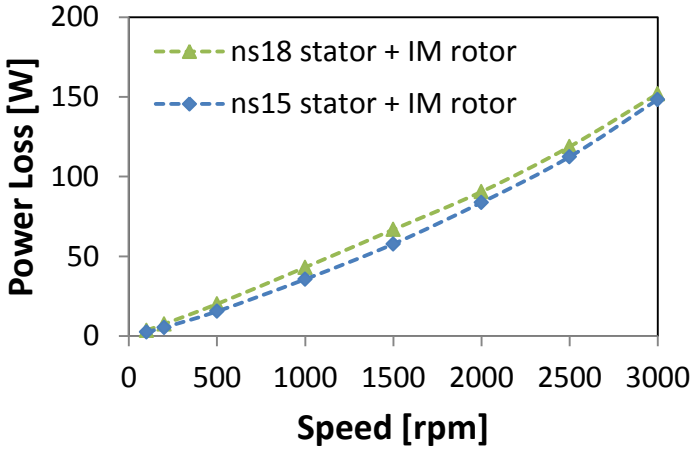

Figure 4-22: The windage and friction losses measured by using an induction rotor of similar weight to the IPM rotors, combined with the ns15 and ns18 stators

The input torque and speed were measured to calculate the input mechanical power. The iron loss is obtained by subtracting the input mechanical power from the measured windage and friction losses, and the copper loss of the stator winding for the short-circuit test [38]. An example segregation of iron loss using the ns18nr12 has been shown in Figure 4-23.

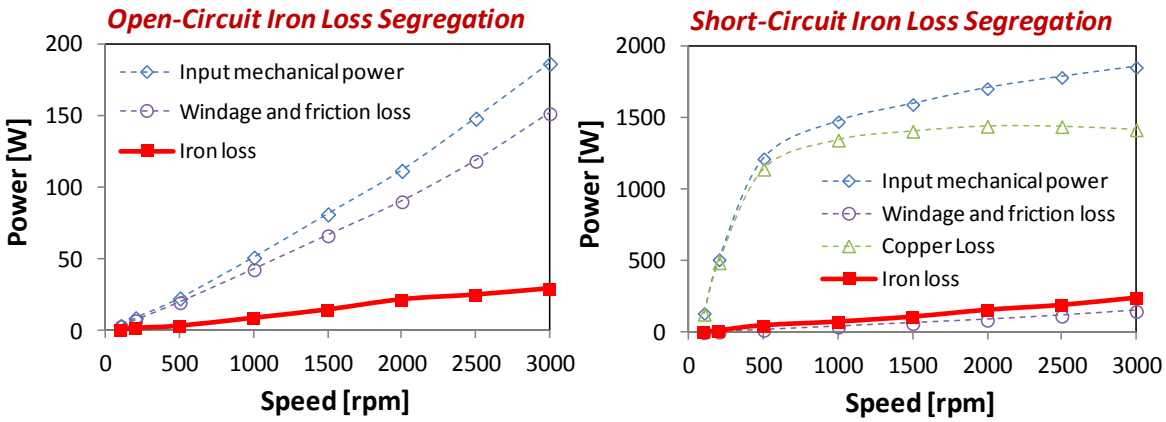

Figure 4-23: Procedure of segregating the iron loss under open- and short-circuit conditions using the example ns18nr12 IPM machine

The following observations can be found in Figure 4-23,

- The windage and friction loss dominates under the open-circuit condition, while the copper loss dominates under short-circuit conditions; the two terms are close to the total input mechanical power under the open- and short-circuit respectively. This means that the measured iron loss is quite sensitive to experimental errors. This is the reason that the segregated iron loss in Figure 4-24 and Figure 4-25 have significant noise levels.
- Under open-circuit condition, the windage and friction loss may vary slightly between bearings, though they are of the same type. This slight change in percentage will possibly lead to a significant variation in the iron loss.
- Under short-circuit operation, the stator temperature rises quickly, which increases the stator resistance, and hence copper loss. A small change in the copper loss could lead to a significant error in the iron loss.

In order to have a better estimation of the stator resistance under short-circuit conditions, a 1A DC current input was used to measure the stator resistance, immediately

before and after the measurement at each speed. The resistance value used to calculate the copper loss is the average of the two.

Figure 4-24 and Figure 4-25 show the measured iron loss results under open- and short-circuit conditions as a function of speed, note the difference in scale between the two graphs.

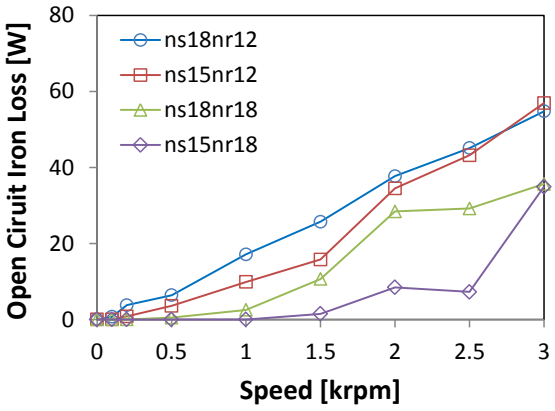

Figure 4-24: Measured iron loss versus speed for the open circuit condition

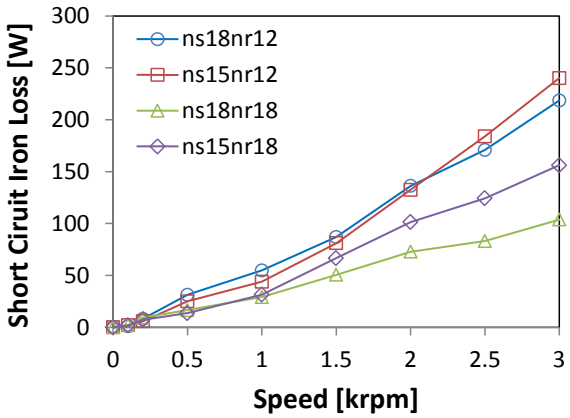

Figure 4-25: Measured iron loss versus speed for the short-circuit condition

As explained earlier, the open circuit loss is dependent on the remanent flux density B_r and volume of the rotor magnet. The corrected magnet B_r for the baseline nr12 and the optimized nr18 IPM rotors are similar as shown in Table 4-3. As the optimized nr18 IPM rotor used 30% less magnet volume, its spatial synchronous component of radial airgap flux density is 8% less than the baseline nr12 IPM rotor as shown in Figure 4-13. This results in the machines with the optimized nr18 IPM rotor having 30% ~ 40% less open-circuit iron loss compared to the baseline nr12 IPM rotor from the test results in Figure 4-24.

Figure 4-25 shows that the highest losses are found with the two designs using the baseline rotor (nr12). This was caused by the combination of two reasons: the high-speed short-circuit current, i.e. characteristic current, for machines with the nr12 IPM rotor is higher for the machines with the nr18 IPM rotor as shown in Table 4-6. Also, the iron loss varies with the n_r/n_s ratio for the same input current under the deep field-weakening as described in Chapter 3. The ns18nr18 IPM machine has the minimum measured iron loss, but this machine also has high torque ripple.

4.2.3. Experimental Verification of Stator-Teeth Flux Density and Iron Loss

The top row in Figure 4-26 shows the open-circuit flux density contours for the IPM machines where the local maximum flux densities of the stator yoke, tooth and rotor channels are indicated. Figure 4-26 also shows the comparisons between the measured and FEM calculated stator tooth flux waveforms (based on search coil tests [39]) and the stator tooth flux density harmonic distribution which generally show a good correspondence. The dominant open-circuit eddy-current loss components in the stator teeth are the low-frequency harmonics (1^{st} and 3^{rd} order), which is similar for the stator yoke. The teeth eddy-current loss are normalized by the corresponding term for the base line ns18nr12 machine.

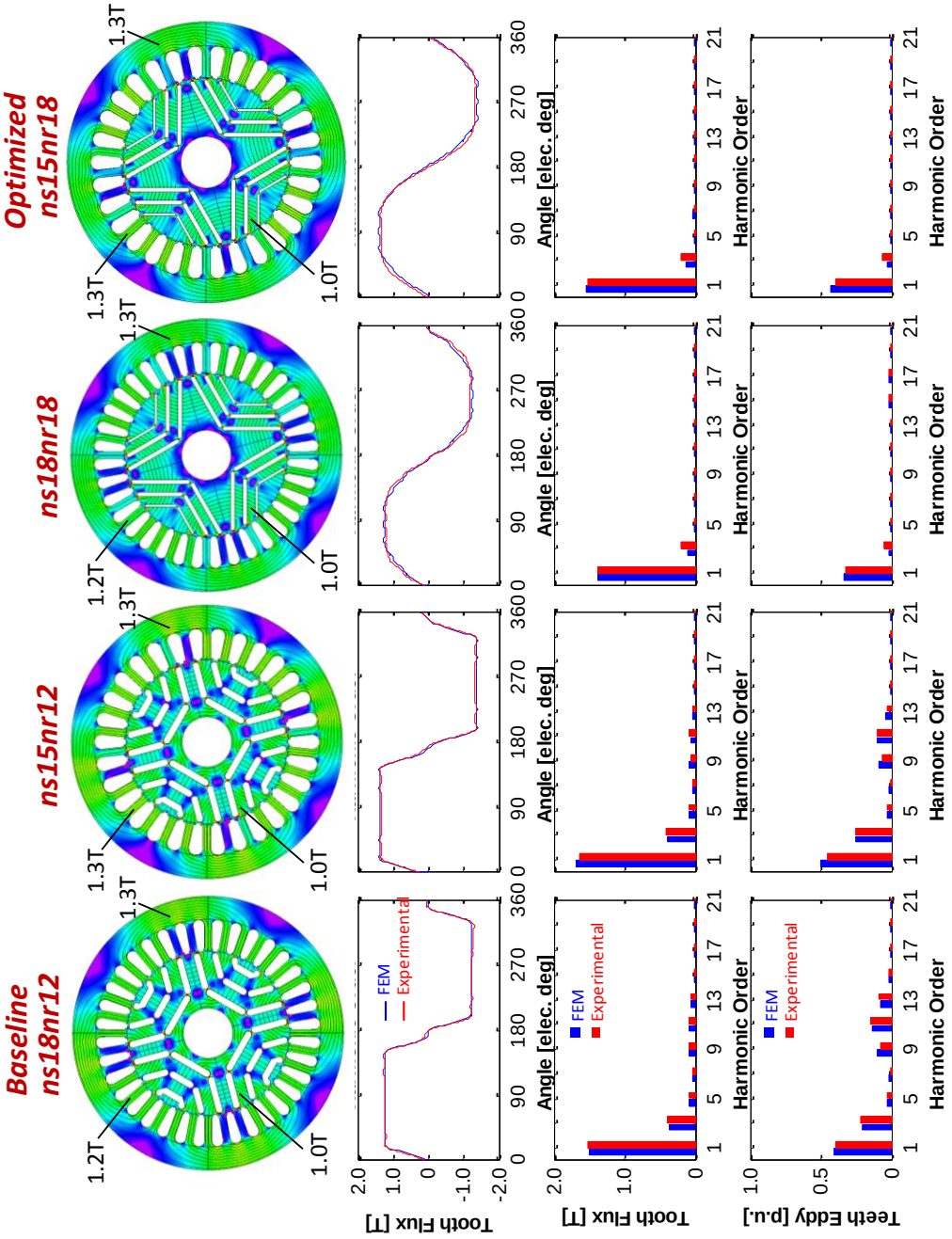

Figure 4-26: The flux density contour plots (top row), experimental and FEM stator tooth flux (2nd row), spectra (3rd row) and eddy-current loss (4th row) under open-circuit operation.

Similarly as Figure 4-26, the top row in Figure 4-27 shows the short-circuit flux density contours for the IPM machines where the local maximum flux densities of the stator yoke, tooth and rotor channels are indicated. Figure 4-27 also shows the comparisons between the measured and FEM calculated stator tooth flux waveforms and harmonic spectra which generally shows a good correspondence. The dominant eddy-current loss components in the stator teeth are the rotor-slot harmonics ($n_r \pm 1$) for the evenly displaced rotor-cavities, such as for the 3-layered nr12 rotor. Note that the 3-layer design corresponds to a full-layered design for the nr12 rotor. Again, the teeth eddy-current loss are normalized by the corresponding term for the base line ns18nr12 machine.

The low-order (3^{rd}, 5^{th} and 7^{th}) loss components in the stator teeth of the ns15nr18 machine are larger than the rotor-slot harmonics (17^{th}, 19^{th}), as the 3-layer design is not a full-layer (or evenly displaced) design for the nr18 rotor.

The FEM analysis predicts that the ns18nr18 machine should have significant eddy-current loss components for the 17^{th} and 19^{th} harmonics in both the stator teeth and yoke. FE analysis was used to show that this is caused by airgap permeance variations rather than the rotor-slot harmonic mmfs, even though these two terms have the same order because $n_s = n_r$. The FEM results also show that these two eddy-current loss components decrease with increasing airgap length for the ns18nr18 machine.

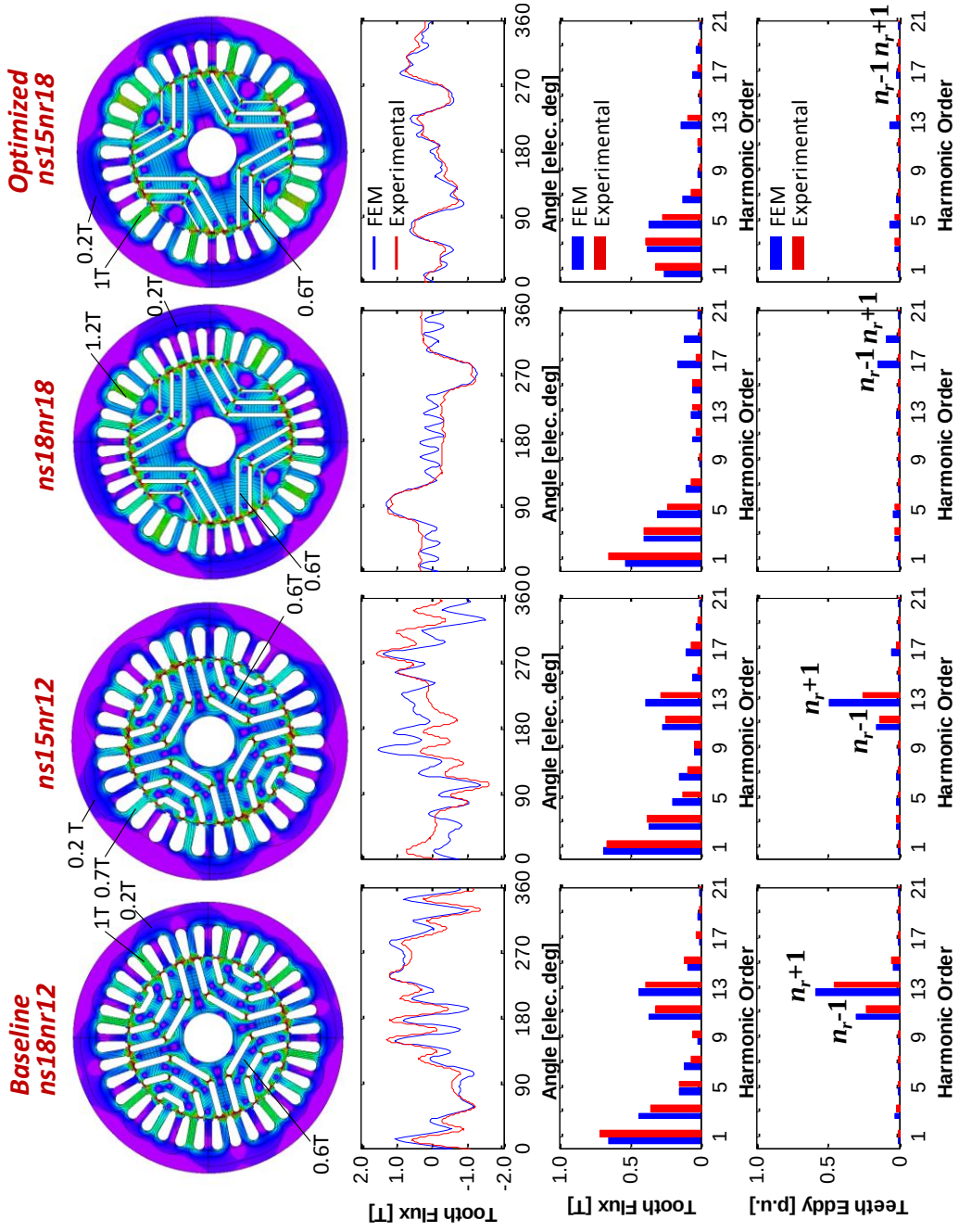

Figure 4-27: The flux density contour plots (top row), experimental and FEM stator tooth flux (2nd row), spectra (3rd row) and eddy-current loss (4th row) under short-circuit operation.

Figure 4-28 shows the open-circuit and short-circuit iron loss with a comparison of the analytical, FEM and experimental results for the four machines. The measured open-circuit iron loss for the machines with the nr18 rotor are generally 35% lower than the machines with the nr12 rotor. The iron loss are reduced in both fundmental and harmonic frequencies as shown in Figure 4-26.

In Figure 4-28, the highest measured short-circuit iron losses are found with the two designs using the baseline rotor (nr12). The optimized design (ns15nr18) reduced the measured iron loss by 30% under deep field-weakening, as is also predicted by the FE results. Unexpectedly, the ns18nr18 IPM machine has the minimum measured iron loss. This is likely due to the reduction in the rotor-slot harmonics in the stator teeth flux as shown in Figure 4-27. The significant discrepancy between the FEM and experimental results for this particular case needs further investigation.

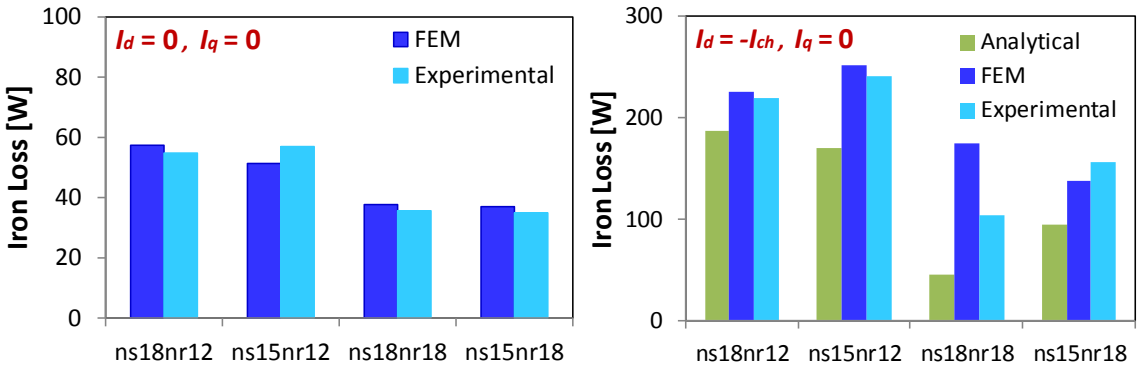

Figure 4-28: Comparison of analytical, FEM and experimental iron loss for open circuit (left) and short circuit (right) for four IPM machines at 3,000rpm.

4.3. Conclusion

This chapter presents the FEM optimization of a baseline ns18nr12 IPM machine. An optimized ns15nr18 IPM machine is proposed with a significant reduction in the torque ripple and iron loss under deep field-weakening. The machine was built and experimental tests were conducted to verify the FEM model in terms of the *dq*-axis flux linkage, back-emf and stator-tooth flux density. The iron loss was measured under open-circuit and short-circuit conditions. The measured iron losses are compared with the calculated results from the FEM models and analytical expressions. The key findings are summarized below,

- The calculated peak-to-peak torque ripple of the optimized ns15nr18 IPM machine is 40% lower compared to the baseline ns18nr12 IPM machine. The ns15nr12 IPM machine has a similar torque ripple as the ns15nr18 IPM machine. The torque ripple of the ns18nr18 IPM machine is significantly higher than the three other IPM machines.
- Based on the back-EMF magnitude, the remanent flux density B_r for the magnets used in the optimized nr18 IPM rotor appears to be 9% lower than the value in the data sheet which was used for the initial FEM optimization. This reduced the characteristic current and short-circuit current correspondingly. In the case that all the machines are driven with the same input current under the deep field-weakening, the lowered magnet B_r has a negligible effect on the iron loss. However, in the case that all the machines are driven with an input current equal to their characteristic current in order to obtain infinite constant-power-speed-ratio, the eddy-current loss will increase proportionally to the square of the input current.
- The end-winding inductance has a significant effect on the prediction of the characteristic current and hence field-weakening performance, and needs to be included into the *dq*-axis inductance calculated by 2-D FEM.
- The measured stator-tooth flux density waveforms match the FEM results, showing that the primary eddy-current loss components in the stator iron are the low-frequency harmonics (1^{st} and 3^{rd} order) under open-circuit; and the high-frequency rotor-slot harmonics ($n_r \pm 1$) under short-circuit conditions which corresponds to deep field-weakening.
- The short-circuit iron losses calculated by the analytical expressions derived in Chapter 3 generally match the FEM and the test results. The optimized ns15nr18 IPM machine was measured to have 30% less iron loss compared to the baseline ns18nr12 IPM machine under the deep field-weakening. The exception was the ns18nr18 IPM machine which shows significantly higher FEM stator iron loss caused by the airgap permeance variation, but this does not show up in its test results.

Chapter 5. Conclusion

This thesis focuses on the electromagnetic design of permanent magnet (PM) machines in terms of the iron loss, torque pulsations and field-weakening performance. It covers the investigation of the effect of stator-slot and rotor-pole number combinations for surface-mounted PM (SPM) machines, and the stator-slot and rotor-effective-slot number combinations for interior permanent magnet (IPM) machines.

The effect of changing the number of slots and poles on the performance of a particular SPM machine design is studied in detail using finite element analysis. This includes examining the back-EMF, the open-circuit/full-load power losses, the cogging/ripple torque, and the field-weakening performance. The simulation results are compared with the expected relationships to provide electric machine designers useful insights on the effect of the number of slots and poles on the performance of SPM machines.

Operation at high speed in traction drives corresponds to deep field-weakening conditions. Due to the high electrical frequencies, the iron loss of IPM machines at high speeds can significantly affect the overall efficiency. This thesis investigates the rotor-cavity positioning and the combination of stator-slot and rotor-effective-slot number on the eddy-current loss for IPM/reluctance machines operating under deep field-weakening

conditions. A new closed-form expression for the stator and rotor eddy-current loss is developed. The optimal barrier-positioning for the minimum total loss and the effect on the eddy-current loss of varying the stator-slot and rotor-effective-slot number are investigated for 1-, 2-, 3- and full-layered rotors.

FEM optimisation and experimental verification of an example IPM machine design are presented. An optimized 30 slot, 4 pole (*SPP* = 2.5) three-layered IPM machine with a significantly reduced iron loss under field-weakening operation is proposed and compared to the baseline 36-slot 4-pole (*SPP* = 3) three-layered IPM machine. The detailed comparison of the optimized and baseline designs using a combination of the analytical, FEM and experimental tests are presented.

5.1. Summary of Key Results

The stator-slot and rotor-pole number combination (*SPP*) is an important parameter for SPM machines, which affects the level of machine power loss, torque pulsations and field-weakening performance. Depending on the value of *SPP*, the stator winding can be either in a distributed configuration for *SPP* ≥1 or a concentrated configuration for *SPP* < 1. The key conclusions are summarized below,

- Power loss for distributed windings: the stator iron loss increases with the number of poles while the copper loss decreases initially. This produces a minimum total loss with about 6 to 12 poles for the stator considered. The magnet and rotor iron losses can usually be neglected.
- Power loss for concentrated windings: low slot number machines (e.g. 12 slots for the stator considered) can have high rotor losses unless segmented or bonded magnets and a laminated rotor are used. Double-layer windings have lower rotor and stator copper losses compared to single-layer windings as they have reduced airgap spatial harmonics and shorter stator end-windings. The rotor losses were found to be proportional to the sum of the squares of the spatial airgap flux density harmonic components produced by the stator current.
- Cogging torque and torque ripple: for distributed windings with integer values of *SPP*, the peak value of the cogging torque and torque ripple increases with the number of poles due to the alignment between the magnet poles and the stator

teeth. Concentrated windings normally have lower cogging torque and torque ripple.

- Field-weakening performance: concentrated windings give better field-weakening performance than distributed windings due to their higher slot leakage inductance.

The rotor-cavity positioning and the combination of stator-slot and rotor-effective-slot number have a first-order effect on the torque pulsation and iron loss for IPM/reluctance machines operating under the deep field-weakening condition. In this thesis, new closed-form analytical expressions of the stator and rotor eddy-current loss are developed for IPM/reluctance machines. By using these analytical iron loss expressions, the optimal rotor cavity positioning for minimum total eddy-current loss is presented for 1-, 2- and 3-layered IPM/reluctance rotors, and the trends of eddy-current loss changes with variations in the stator-slot and rotor-effective-slot number are predicted for 1-, 2-, 3- and full-layered rotors. The key conclusions are summarized below,

- Increasing the number of cavity layers leads to a large drop in stator iron loss but a comparatively smaller rise in rotor iron loss, resulting in a reduced total iron loss in general for 1- to 3-layer rotors.
- For a fixed value of n_r/n_s, reducing the stator-slot number n_s leads to a significant drop in total iron loss for the designs with unevenly displaced rotor cavities, meaning that the minimum iron loss occurs with small stator slot numbers.
- Designs with $1 < n_r/n_s < 2$ were able to keep a low total eddy-current loss in general for all the cavity-layer designs, where the minimum loss occurs at $1 < n_r/n_s \leq 1.2$ and $1.8 < n_r/n_s < 2$. However, designs in this regime have increased rotor iron loss. It is generally more challenging to remove heat from the rotor than from the stator and this may result in increased rotor temperataure and reduced magnet flux.
- Designs with $0.8 \leq n_r/n_s < 1$ have comparable total iron loss as those with $1 < n_r/n_s \leq 1.2$, with a greater proportion of this in the stator iron. This may allow adopting typical stator cooling strategies such as water jackets and blowing air on fins etc.
- Designs with an integer number of n_r/n_s have the minimum total iron loss if the stator slotting effect is neglected. However, the combinations with n_r equal to a multiple of n_s are usually avoided by designers because of their substantial torque ripple components caused by the product of the stator slot ($k \cdot n_s \pm 1$) and rotor slot

($k \cdot n_r \pm 1$) harmonic mmfs when n_r is the multiple of n_s. Despite this intrinsic flaw, possible improved designs for these special combinations may be obtained by applying skewing to the stator and rotor laminations.

FEM optimization was performed on a baseline 36-slot 4-pole three-layered IPM machine with the stator-slot (n_s) and rotor-effective-slot (n_r) number combination of n_s =18 and n_r=12 which can be written as ns18nr12. An optimized ns18nr18 IPM machine is proposed with significant reductions in the calculated torque ripple and iron loss under deep field-weakening. The comparative studies of iron loss and torque ripple was done for the baseline ns18nr12, the optimized ns15nr18 and two other machines obtained by interchanging the stators and rotors of the baseline and optimised machines, i.e. ns15nr12 and ns18nr18. Experimental tests are conducted to verify the FEM model in terms of the *dq*-axis flux linkage, back-emf, stator-tooth flux density and open-circuit/short-circuit iron loss. The key conclusions includes,

- The calculated peak-to-peak torque ripple of the optimized ns15nr18 IPM machine is reduced by more than 40% in comparison to the baseline ns18nr12 IPM machine. The ns15nr12 IPM machine has a similar torque ripple as the ns15nr18 IPM machine. The torque ripple of the ns18nr18 IPM machine is significantly higher than any other combinations of IPM machines.
- Based on a comparison of the measured and FEM calculated back-EMF magnitudes, the remanent flux density B_r of the magnets used in the optimized nr18 IPM rotor appears to be 9% lower than the datasheet value used in the FEM optimization. This reduced the characteristic current and hence the short-circuit current. In the case that all the machines are driven with the same input current under deep field-weakening, the lowered magnet B_r has a negligible effect on the iron loss. However, in the case that all the machines are driven with an input current equal to their characteristic current in order to obtain infinite constant-power-speed-ratio, the eddy-current loss will increase proportionally to the square of the input current.
- The end-winding inductance has a significant effect on the prediction of the characteristic current and hence field-weakening performance, and thus needs to be included into the *dq*-axis inductance calculated by 2-D FEM.

- The measured stator-tooth flux density matches the FEM results, showing that the primary eddy-current loss components in the stator iron are the low-frequency harmonics (1^{st} and 3^{rd} order) under open-circuit conditions and the high-frequency rotor-slot harmonics ($n_r \pm 1$) under deep field-weakening.
- The iron losses calculated by the proposed analytical expressions generally match the FEM and the short-circuit test results. The optimized ns15nr18 IPM machine reduced the iron loss by 30% compared to the baseline ns18nr12 IPM machines under deep field-weakening. The exception was the ns18nr18 IPM machine which shows significantly higher FEM stator iron loss caused by the airgap permeance variation, but this does not appear in its test results.

5.2. Suggestions for Further Research

The study of the stator-slot and rotor-pole number combinations for SPM machines was based on a particular design using FEM analysis. Further work may consider developing a more general analysis in order to gain detailed guidelines for selecting the stator-slot and rotor-pole number combination. Apart from the stator-slot and rotor-pole number combinations, there are also other design strategies, such as the skewing the stator teeth or rotor magnets, which can reduce the torque pulsations.

Future work regarding the analytical modelling of iron losses in IPM machines could be associated with a more detailed investigation of the stator and rotor eddy-current loss changes with factors such as the flux passing through the rotor cavities and the impact of saturation. In addition, IPM machines which have a stator-slot number equal to the rotor-effective-slot number may have a significant iron loss component caused by airgap permeance variations. This could also be further investigated in future research.

Appendix A. Stator and Rotor Filtering Effect

Appendix A presents the analysis of the stator and rotor filtering effect based on the flux and eddy-current loss spectra and the "*filter function*" method. The eddy-current losses for the stator tooth body and yoke are predicted and validated by FEM results. A European Steel (Polycor steel) with an eddy-current loss coefficient k_e = 2.0 W/m^3 is used for calculating eddy-curent loss for both analytical and FEM.

A.1. "Filter Function" Analysis for Flux and Eddy-Current Loss Density Spectra

A simple way of understanding the filtering effect of the stator teeth and yoke is to use the "*filter function*" shown below,

$$\begin{cases} \hat{B}_{tn} = Filter_{teeth} \cdot \hat{B}_{grn} \\ Filter_{teeth} = k_t \cdot \mathrm{sinc}\left(\dfrac{n\pi}{n_s}\right) \end{cases} \tag{A-1}$$

$$\begin{cases} \hat{B}_{yn} = Filter_{yoke} \cdot \hat{B}_{grn} \\ Filter_{yoke} = k_y \cdot \dfrac{1}{n\pi} \end{cases} \tag{A-2}$$

The "eddy-current loss potential" from the airgap flux density is defined as,

$$p_{s\_air} = k_e f_1^2 \sum_{n=1}^{\infty} h^2 \hat{B}_{grn}^2 \tag{A-3}$$

The eddy-current loss density can be obtained from (A-1), (A-2) and (A-3), and expressed as,

$$p_{teeth} = p_{s\_air} \cdot Filter_{teeth}^2 \tag{A-4}$$

$$p_{yoke} = p_{s\_air} \cdot Filter_{yoke}^2 \tag{A-5}$$

(A-4) and (A-5) shows the eddy-current loss density is the product of the eddy-current loss potential and the squared filter functions.

The stator tooth "filter function", $Filter_{teeth}$, is the product of the slot-pitch to teeth-body-width ratio and the *sinc* function. In contrast, the stator yoke filter function, $Filter_{yoke}$, is the product of the ratio of the airgap radius to the yoke width, and the inverse of the number of pole pairs and the harmonic order. The "filter function" only depends on the dimensions of the stator. Thus IPM machine designs with the same stator has the same "filter function". The procedure of predicting the tooth and yoke flux density and their eddy-current loss from the airgap flux density spectrum is shown in Figure A-1, using the example of the ns15nr18 IPM machine under short-circuit conditions.

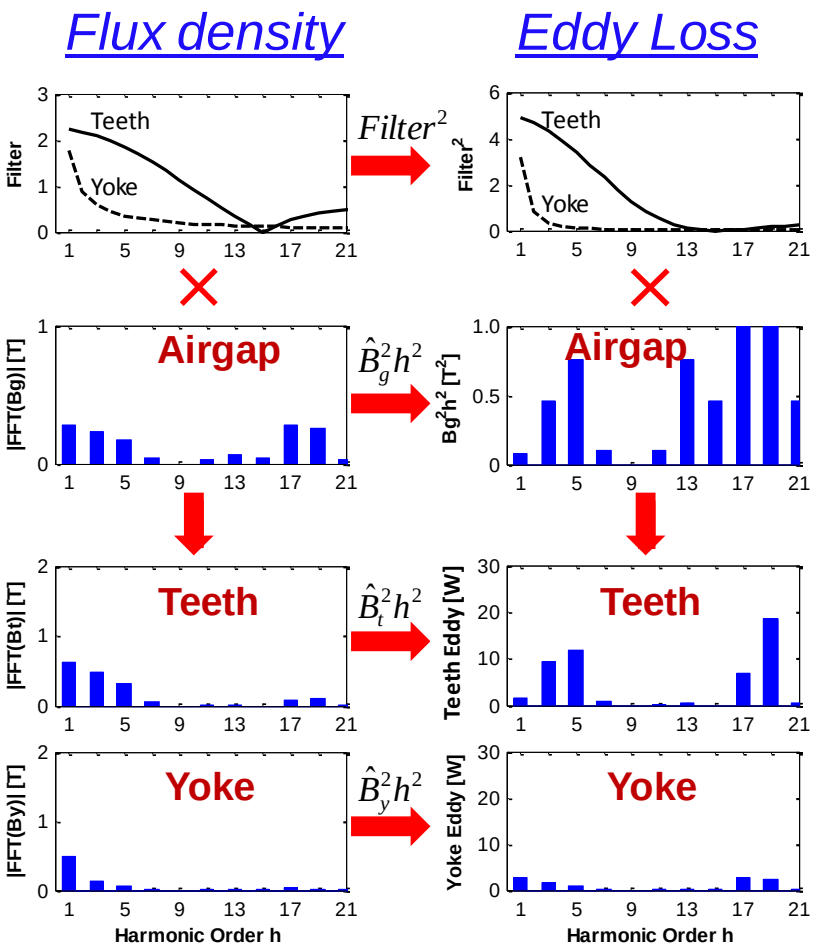

Figure A-1: Spectral analysis procedure to predict the tooth and yoke flux densities and their eddy-current losses from the airgap flux density, using the example ns15nr18 IPM under short-circuit conditions

In Figure A-1, there are two regions or groups of harmonics in the airgap flux spectrum: the first region is located close to the fundamental harmonic (from the fundamental to 1/2 of the number of slots-per-pole-pair, referred to as the low-frequency region. In this region, the eddy-current loss potential is relative low due to the low harmonic order.

The second region lies in the neighbourhood of the number of slots-per-pole-pair (from 1/2 to 3/2 of the number of slots-per-pole-pair), which are referred to as the high-frequency region. The eddy-current loss potential is much higher in this region due to the higher harmonic order.

The analytical predicted stator teeth flux density in Figure A-2 shows less noise compared to the FEM results. This is because of the assumption of the smooth stator with an equivalent airgap length ignoring the airgap slot permeance variations. It was found that

a FEM model with a very small slot opening and increased effective airgap length shows a closer match with the analytical results.

The fundamental stator mmf only reacts with the fundamental rotor mmf, and all higher harmonics in the airgap flux density are derived from the rotor mmf waveform.

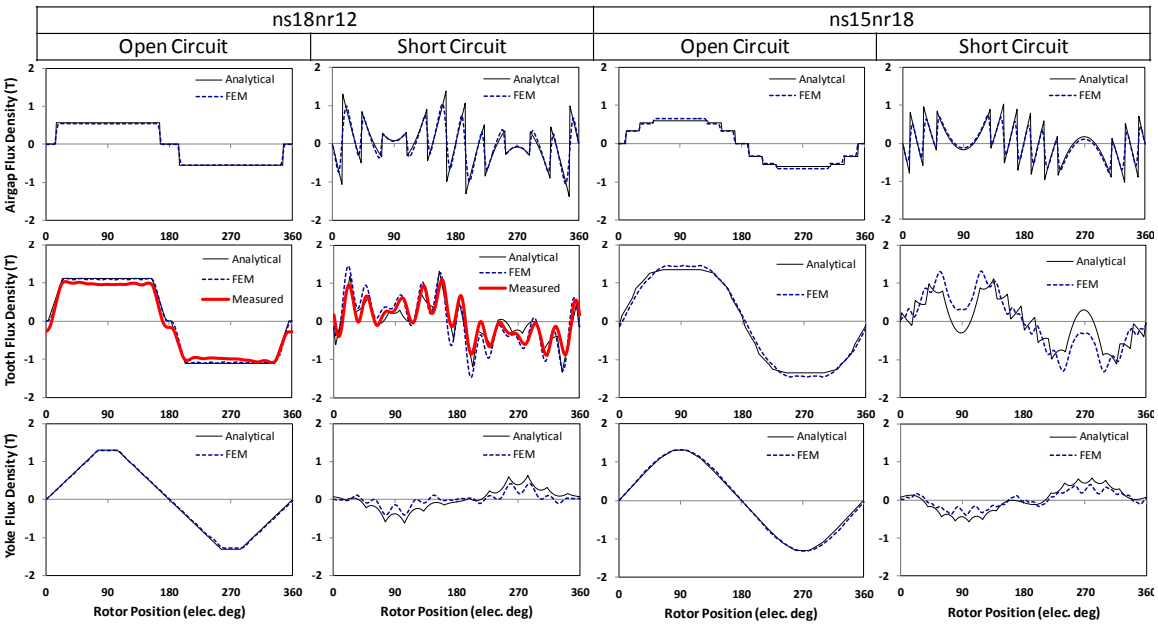

Figure A-2: Airgap radial flux density (top), tooth flux density (middle) and yoke flux density (bottom) for the ns18nr12 and ns15nr18 IPM machines showing the comparison of the analytical prediction and FEM. Measurements are shown for the tooth flux density for the baseline machine.

A.2. Spectral Analysis of Stator Eddy-Current Loss under Open Circuit Conditions

Figure A-3 shows the filter functions in the first row, airgap flux density spectra in the second row, stator teeth flux density spectra in third row and yoke flux desnity spectra in last row, for the open circuit condiction. The same arrangement will be used for the filter function analysis in the following sections.

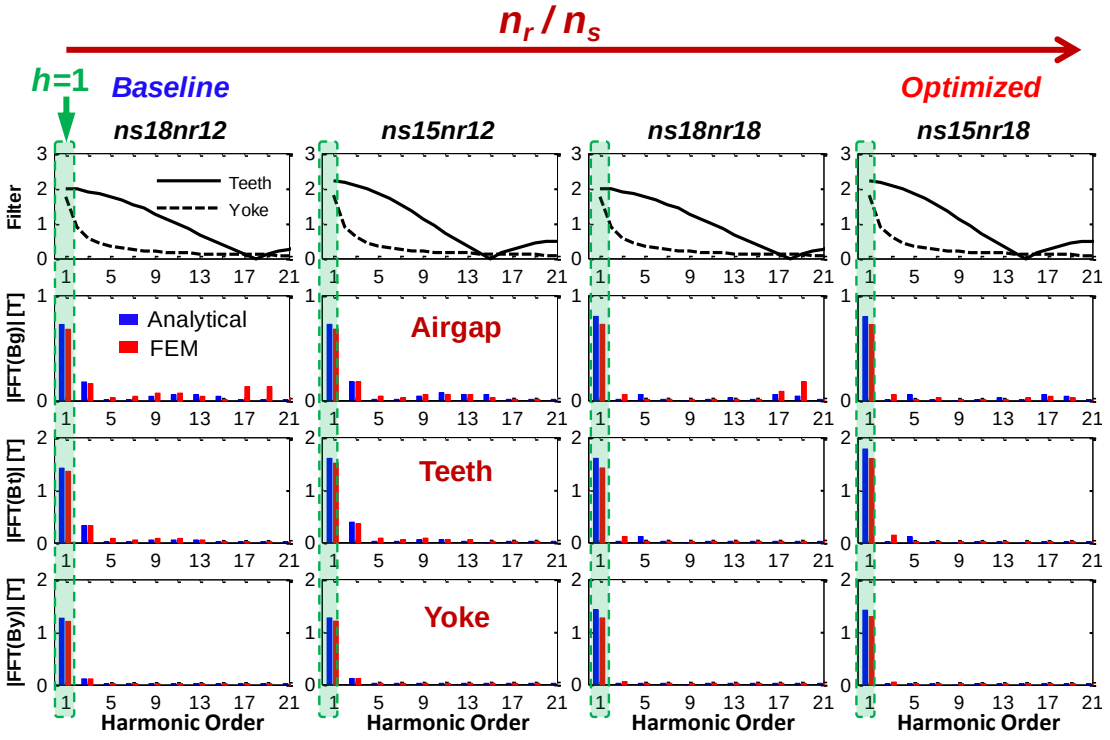

Figure A-3: Open-circuit flux density spectra for the airgap (second row), stator tooth (third row) and yoke (fourth) for the IPM machines showing the analytical prediction and FEM

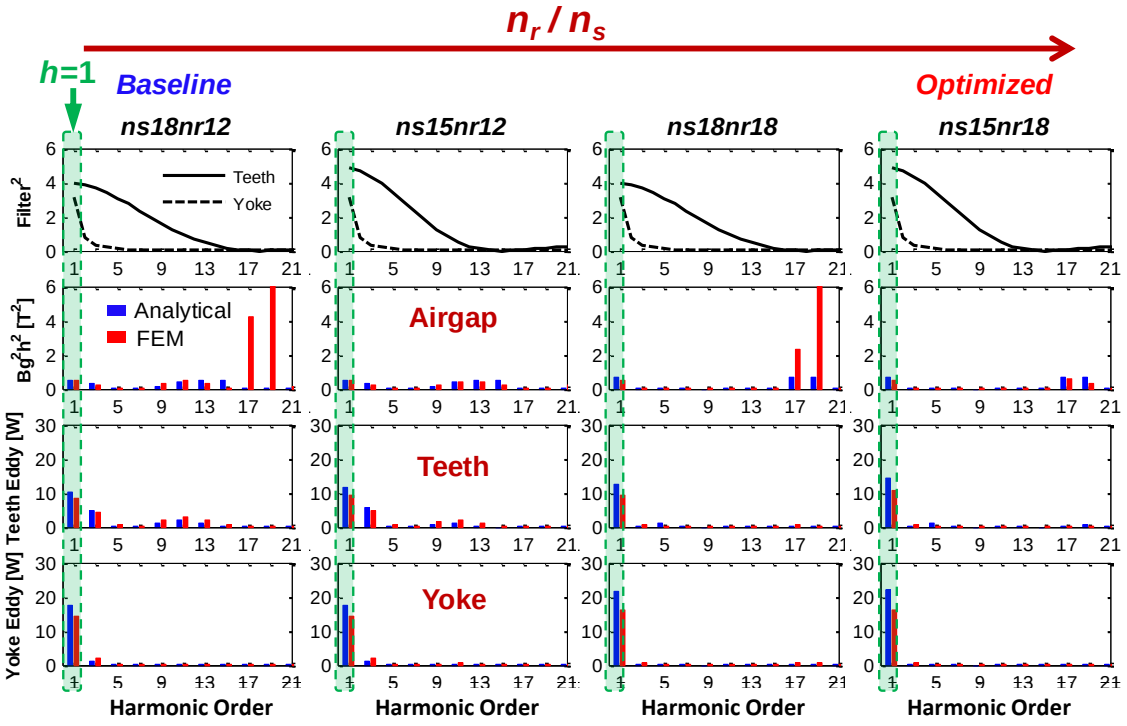

Figure A-4: Open-circuit eddy-current loss spectra for the airgap, stator tooth and yoke for the IPM machines showing the comparison of the analytical prediction and FEM

Though the yoke and teeth eddy-current expressions in (A-4) and (A-5) are of similar form, the yoke filter function $Filter_{yoke}$ effectively filters all the high order airgap flux components with large eddy-current loss potential. In contrast, the teeth filter function has a lower capability to filter out the high order components in the airgap flux density, especially components which are close to the number of slots per pole-pair. This results in the stator teeth eddy-current loss being usually higher than the stator yoke, despite starting from the same eddy-current loss potential (that is, airgap flux density distribution).

The procedure in Figure A-1 is used to analyze the teeth and yoke flux density of the four IPM machines in Figure A-3 and their eddy-current loss in Figure A-5.

Under the open-circuit condition, the largest teeth and yoke flux harmonics lie close to the fundamental, i.e. the low frequency region where the eddy-current loss potential is small. The airgap flux harmonics in the high frequency region are very small. The eddy-current loss of both the teeth and yoke are relatively small. The filtering effects on the teeth and yoke flux and hence eddy-current loss are thus not strong under the open-circuit condition.

A.3. Spectral Analysis of Stator Eddy-Current Loss under Deep Field-Weakening

The situation becomes opposite for the short-circuit case where the teeth and yoke flux harmonics in the high frequency region are significantly increased, resulting in much larger eddy-current loss potential. The largest eddy-current loss harmonics have an order in the neighbourhood of the number of the effective-rotor-slots-per-pole-pair (n_r), e.g. 13^{th} for the ns18nr12 IPM, 17^{th} for the ns18nr18 IPM and 13^{th} again for the ns15nr12 IPM. These frequency components are called “rotor-slot harmonics” and have frequencies of order $k \cdot n_r \pm 1$, where k is an integer. The proposed ns15nr18 IPM does not have any large eddy-current loss harmonics.

For a given stator, the most efficient way to reduce the large eddy-current loss potential in the high frequency region is to select the number of effective-rotor-slots-per-pole-pair (n_r) in order to “push” the rotor mmf harmonics to be greater than the number of the stator-slots-per-pole-pair (n_s). For instance, under short-circuit conditions, the stator eddy-current loss is reduced by incorporating the optimised nr18 IPM rotor with the ns15

and ns18 stators in comparison to combining the nr12 IPM rotor with the same two stators (i.e. the ns18nr18 versus the ns18nr12, and the ns15nr18 versus the ns15nr12).

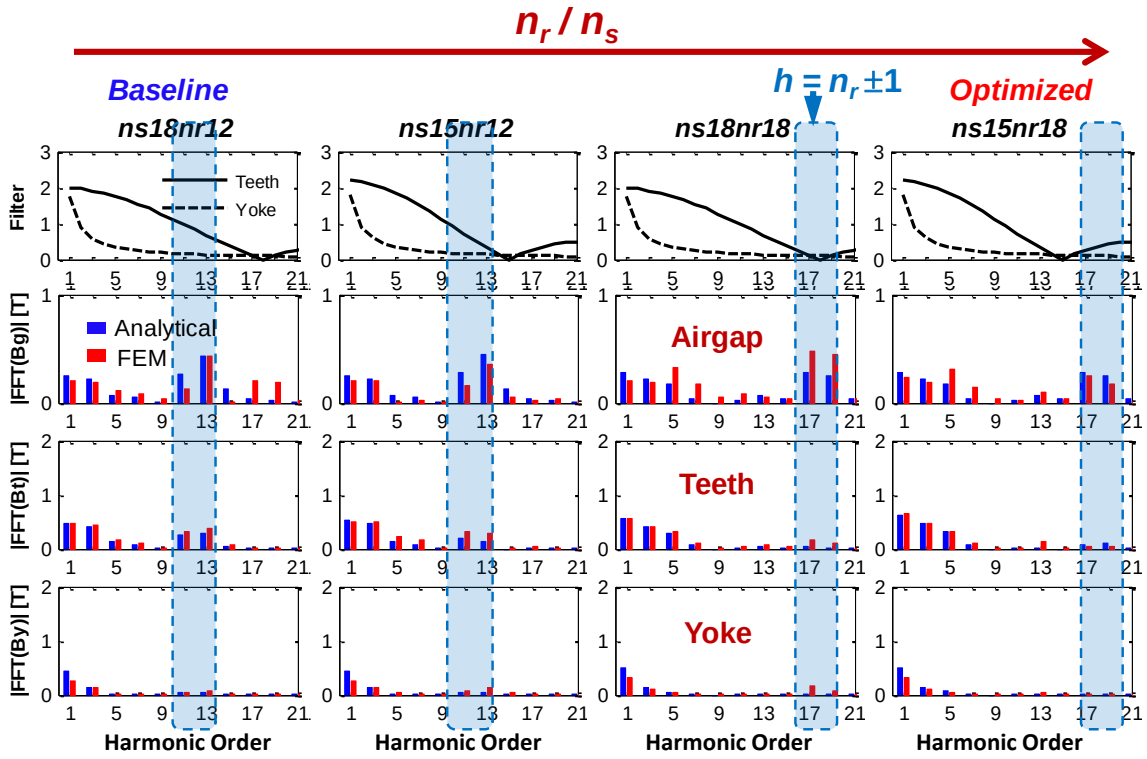

Figure A-5: Short-circuit flux density spectra for the airgap, stator tooth and yoke

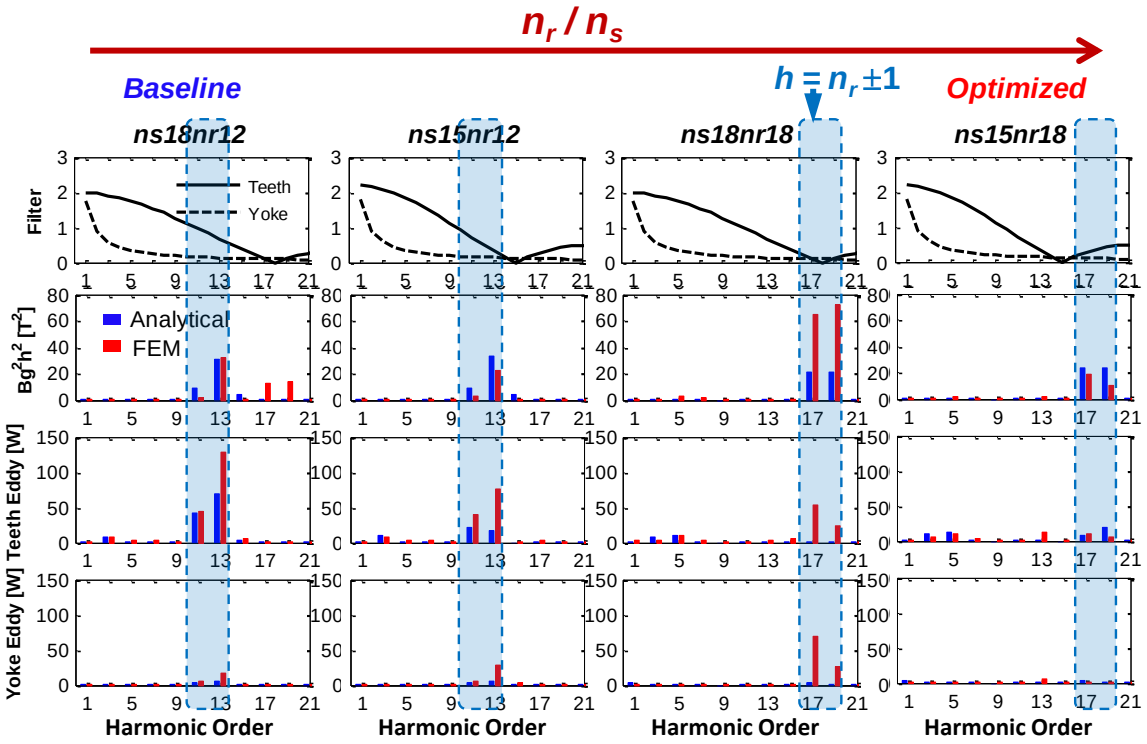

Figure A-6: Short-circuit eddy-current loss spectra for the airgap, stator tooth and yoke

For a given rotor, using a smaller number of stator slots can efficiently reduce the eddy-current loss in the stator by filtering out the harmonics with large eddy-current loss potential. For instance for the nr18 rotor, using the ns15 stator gives lower eddy-current loss compared to the ns18 stator. Similarly, for the nr12 IPM rotor, using the ns15 stator also gives a lower eddy-current loss compared to the ns18 stator.

The ns15nr18 IPM machine effectively applies this rule to obtain the minimum stator iron loss under the short-circuit condition. In contrast, the baseline ns18nr12 IPM machine has the highest stator iron losses. The stator teeth filter function for this machine cannot effectively filter the high amplitude 11^{th} and 13^{th} harmonics produced by the rotor.

The stator yoke filter function can effectively filter the harmonics in the high frequency region, resulting in a much lower short-circuit eddy-current loss in comparison to the stator teeth.

A.4. Summary for Filtering Effect

The predicted stator iron loss is close to the FE results for the open-circuit cases, but has only limited accuracy for the short-circuit cases. The discrepancy mainly arises from the harmonics in the higher frequency region. The flux spectrums in Figure A-3 and Figure A-5 show that the eddy-current loss is sensitive to the flux density in the high frequency region. The rotor-slot harmonics of order $k \cdot n_r \pm 1$ are the primary components in the short-circuit eddy-current loss spectra.

A finite-element model with a small slot opening was used to show that the variation of airgap permeance due to stator slotting has a first-order impact on the prediction of the teeth and yoke flux density in the high frequency region. The stator mmf harmonics have a primary effect on the fundamental teeth and yoke flux density, but much smaller effect on the high frequency region. This is because the stator mmf harmonics rotate at different mechanical speeds which results in a change of the amplitude of the rotor mmf in both the low and high frequency regions. However, as far as the eddy-current losses are concerned, the stator mmf harmonics take a much smaller responsibility for the discrepancy between the analytical and FE eddy-current loss in the high frequency region, in comparison to the airgap permeance variation.

In general, the proposed analytical approach shows a good prediction of the stator iron loss under open-circuit conditions compared to finite-element analysis. It shows a

reasonable accuracy under short-circuit conditions except when the number of stator and effective rotor teeth are comparable. This is due to the substantial errors primarily caused by neglecting the airgap permeance variation in the analysis.

In the analysis of the rotor iron loss, the situation of the rotor channels filtering the airgap flux density is similar to the stator teeth filtering the airgap flux density as described above.

References

[1] C.C. Mi, G.R. Slemon and R. Bonert, "Minimization of Iron Losses of Permanent Magnet Synchronous Machines," *IEEE Trans. Energy Conv.*, vol. 20, no. 1, pp. 121-127, March 2005.

[2] A.M. El-Refaie and T.M. Jahns, "Optimal Flux Weakening in Surface PM Machines Using Fractional-Slot Concentrated Windings," *IEEE Trans. Ind. Appl.*, vol. 41, no. 3, pp. 790- 800, May 2005.

[3] A.M. El-Refaie, T. M. Jahns, P. J. McCleer, and J.W. McKeever, "Experimental verification of optimal flux weakening in surface PM machines using concentrated windings," *IEEE Trans. Ind. Appl.*, vol. 42, no. 2, pp. 443–453, Mar. 2006.

[4] F. Magnussen, P. Thelin and C. Sadarangani, "Performance Evaluation of Permanent Magnet Synchronous Machines with Concentrated and Distributed Windings Including the Effect of Field Weakening," in *Conf. Rec. PEMD'04*, vol. 2, pp. 679-685, 2004.

[5] N. Bianchi, S. Bolognani and E. Fornasiero, “An Overview of Rotor Losses Determination in Three-Phase Fractional-Slot PM Machines,” *IEEE Trans. Ind. Appl.*, vol. 46, no. 6, pp. 2338- 2345, Nov. 2010.

[6] A.M. El-Refaie and T.M. Jahns, “Impact of Winding Layer Number and Magnet Type on Synchronous Surface PM Machines Designed for Wide Constant-Power Speed Range Operation,” *IEEE Trans. Energy Conv.*, vol. 23, no. 1, pp. 53- 60, Mar. 2008.

[7] J.D. Ede, K. Atallah, G.W. Jewell, J.B. Wang and D. Howe, “Effect of Axial Segmentation of Permanent Magnets on Rotor Loss in Modular Permanent-Magnet Brushless Machines,” *IEEE Trans. Ind. Appl.*, vol. 43, no. 5, pp. 1207-1213, Sep. 2007.

[8] K. Atallah, D. Howe, P.H. Mellor and D.A. Stone, “Rotor Loss in Permanent Magnet Brushless AC Machine,” *IEEE Trans. Ind. Appl.*, vol. 36, no. 6, pp. 1612- 1618, Nov. /Dec. 2000.

[9] D. Ishak, Z.Q. Zhu, D. Howe, "Eddy-current loss in the rotor magnets of permanent-magnet brushless machines having a fractional number of slots per pole," *Magnetics, IEEE Trans. Magn.*, vol. 41, no. 9, pp. 2462- 2469, Sept. 2005.

[10] T. Hiroaki, Z. Xia, J.Wang, K. Atallah, and D. Howe, “Rotor eddy-current loss in permanent-magnet brushless machines,” *IEEE Trans. Magn.*, vol. 40, no. 4, pp. 2104–2106, Jul. 2004.

[11] H. Polinder and M. J. Hoeijmaker, “Eddy current losses in segmented surface-mounted magnets of a PM machine,” in *IEE Proc. Elect. Power Appl.*, May 1999, vol. 146, no. 3, pp. 261–266.

[12] K. Yamazaki and Y. Kanou, “Rotor loss analysis of interior permanent magnet motors using combination of 2-D and 3-D finite element method,” *IEEE Trans. Magn.*, vol. 45, no. 3, pp. 1772–1775, Mar. 2009.

[13] M. Andriollo, G. Bettanini, G. Martinelli, A. Morini, and A. Tortella, “PM losses evaluation by harmonic analysis of the magnetic vector potential perturbation,” in *Proc. IEEE Power Energy Society General Meeting - Convers. Delivery Elect. Energy 21st Century*, Pittsburgh, PA, Jul. 20–24, pp. 1–6, 2008.

[14] T. Katsuma and M. Kitoh, “Brushless motor having permanent magnet rotor and salient pole stator,” U.S. Patent 4719378, Aug. 21, 1986.

[15] S. Nishio, “Polyphase direct current motor,” U.S. Patent 5006745, Aug. 3, 1989.

[16] K.F. Konecny, “Compact three-phase permanent magnet rotary machine having low vibration and high performance,” U.S. Patent 4774428, May 15, 1987.

[17] J. Cros and P. Viarouge, “Synthesis of high performance PM machines with concentrated windings,” *IEEE Trans. Energy Conv.* vol. 17, no. 2, pp. 248-253, 2002.

[18] D. Ishak, Z.Q. Zhu, D. Howe, "Permanent-magnet brushless machines with unequal tooth widths and similar slot and pole numbers," *IEEE Trans. Ind. Appl.*, vol. 41, no. 2, pp. 584- 590, Mar. 2005

[19] D. Ishak, Z.Q. Zhu and D. Howe, "Comparison of PM brushless motors, having either all teeth or alternate teeth wound," *IEEE Trans. Energy Conv.*, vol. 21, no. 1, pp. 95- 103, March 2006.

[20] Z.Q. Zhu and D. Howe, “Influence of Design Parameters on Cogging Torque in Permanent Magnet Machines,” *IEEE Trans. Energy Conv.*, vol. 15, no. 4, pp. 407-412, Dec. 2000.

[21] A.M. El-Refaie, “High Speed Operation of Permanent Magnet Machines”, *PhD Thesis*, University of Wisconsin-Madison, pp. 148-149, 2005.

[22] J.R. Hendershot and T.J.E. Miller, "*Design of Brushless Permanent-Magnet Motors*," Magna Physics Publishing and Clarendon Press, 1994.

[23] C.C. Mi, G.R. Slemon and R. Bonert, "Modeling of Iron Losses of Permanent-Magnet Synchronous Motors," *IEEE Trans. Ind. Appl.*, vol. 39, no. 3, pp. 734- 742, May, 2003

[24] M. Kamiya, "Development of Traction Drive Motors for the Toyota Hybrid System," *IEEJ Transactions on Ind. Appl.*, v126, n4, 2006

[25] S.-H. Han, W.L. Soong, T.M. Jahns, M.K. Guven, and M.S. Illindala, "Reducing harmonic eddy-current losses in the stator teeth of interior permanent magnet synchronous machines during flux weakening," *IEEE Trans. Energy Convers*., v25, n2, pp 441–449, Jun. 2010.

[26] M. Barcaro, N. Bianchi, and F. Magnussen, "Rotor flux-barrier geometry design to reduce stator iron losses in synchronous IPM motors under FW operations," *IEEE Trans. Ind. Appl*., v46, n5, pp 1950–1958, Sep./Oct. 2010.

[27] G. Pellegrino, P. Guglielmi, A. Vagati, and F. Villata, "Core losses and torque ripple in IPM machines: Dedicated modeling and design tradeoff," *IEEE Trans. Ind. Appl*., v46, n6, pp2381–2391, Nov. 2010.

[28] S.-H. Han, T.M. Jahns and Z.Q. Zhu, "Analysis of Rotor Core Eddy-Current Losses in Interior Permanent-Magnet Synchronous Machines," *IEEE Trans. Ind. Appl*., v46, n 1, pp. 196–205, Jan. 2010.

[29] A. Vagati, M. Pastorelli, G. Franceschini and S.C. Petrache, "Design of Low-Torque-Ripple Synchronous Reluctance Motors," *IEEE Trans. Ind. Appl.*, v34, n4, pp758–765, Jul. 1998.

[30] A. Vagati, “Synchronous Reluctance Electrical Motor Having a Low Torque-Ripple Design,” U.S. Patent Application 08/671/653-06/28/96

[31] C. Tang, W.L. Soong, G.S. Liew, N. Ertugrul and T.M. Jahns, “Analysis of Stator Iron Loss in Interior PM Machines under Open and Short-Circuit Conditions,” *2013 IEEE Energy Conversion Congress and Exposition (ECCE)*, pp1227-1234, Sep. 2013

[32] T. A. Lipo, *Introduction to AC Machine Design*. University of Wisconsin, 2004, pp. 539–542.

[33] R.F. Schiferl and T.A. Lipo, “Power Capability of Salient Pole Permanent Magnet Synchronous Motors in Vriable Speed drive Applications,” *IEEE Trans. Ind. Appl.*, v26, n1, pp115–123, Jan.1990.

[34] S.-H. Han, W.L. Soong, and T.M. Jahns, "An Analytical Design Approach for Reducing Stator Iron Losses in Interior PM Synchronous Machines During Flux-Weakening Operation", *Conference Record of the 2007 IEEE Industry Applications Conference Annual Meeting*, pp 103-110, LA, Sept 2007.

[35] S. H. Han, T. M. Jahns, W. L. Soong, M. K. Guven, and M. S. Illindala, “Torque ripple reduction in interior permanent magnet synchronous machines using stators with odd number of slots per pole pair,” *IEEE Trans. Energy Convers.*, vol. 25, no. 1, pp. 118–127, Mar. 2010.

[36] D. A. Staton, W. L. Soong, and T. J. E. Miller, “Unified theory of torque production in switched reluctance and synchronous reluctance motors,” *IEEE Trans. Ind. Appl.*, vol. 31, no. 2, pp. 329–337, Mar./Apr. 1995.

[37] W. L. Soong, “Inductance Measurements for Sychronous Machines,” PEBN #2, May 2008, available at http://www.eleceng.adelaide.edu.au/research/power/pebn/

[38] W. L. Soong, "Parameter Measurement and Performance Prediction," PEBN #7, May 2008, available at http://www.eleceng.adelaide.edu.au/research/power/pebn/

[39] V. Zivotic-Kukolj, W.L. Soong and N. Ertugrul, "Iron Loss Reduction in an Interior PM Automotive Alternator," *IEEE Trans. Ind. Appl.*, vol. 42, issue 6, pp. 1478 – 1486, Nov./Dec. 2006.

[40] R. Schiferl and T. A. Lipo, "Core loss in buried magnet permanent magnet synchronous motors," *IEEE Trans. EnergyConvers.*, vol. 4, no. 2, pp. 279–284, Jun. 1989.

[41] W. L. Soong and N. Ertugrul, "Field-weakening performance of interior permanent-magnet motors," *IEEE Trans. Ind. Appl.*, vol. 38, no. 5, pp. 1251–1258, Sep./Oct. 2002.

[42] W. Soong and T. Miller, "Field-weakening performance of brushless synchronous ac motor drives," *Proc. Inst. Elect. Eng.—Electric Power Application*, vol. 141, no. 6, Nov. 1994.

[43] G. Pellegrino, A. Vagati, and P. Guglielmi, "Design tradeoffs between constant power speed range, uncontrolled generator operation, and rated current of IPM motor drives," *IEEE Trans. Ind. Appl.*, vol. 47, no. 5, pp. 1995–2003, Sep./Oct. 2011.

[44] G. Pellegrino, A. Vagati, P. Guglielmi, and B. Boazzo, "Performance comparison between surface mounted and interior PM motor drives for electric vehicle application," *IEEE Trans. Ind. Electron.*, vol. 59, no. 2, pp. 803–811, Feb. 2012.

[45] N. Bianchi and E. Fornasiero, "Impact of MMF space harmonics on rotor losses in fractional-slot permanent-magnet machines," *IEEE Trans. Energy Convers.*, vol. 24, no. 2, pp. 323–328, Jun. 2009.

[46] P. B. Reddy, A. M. EL-Refaie, Huh Kum-Kang, J. K. Tangudu, and T. M. Jahns, "Comparison of Interior and Surface PM Machines Equipped With Fractional-Slot Concentrated Windings for Hybrid Traction Applications," *IEEE Trans. Energy Convers*, vol.27, no.3, pp.593-602, Sept. 2012

[47] J. K. Tangudu, and T.M. Jahns, "Comparison of interior PM machines with concentrated and distributed stator windings for traction applications," *IEEE Vehicle Power and Propulsion Conference (VPPC),* pp.1-8, Sep. 2011

[48] L. Alberti, M. Barcaro, and N. Bianchi, "Design of a Low Torque Ripple Fractional-slot Interior Permanent Magnet Motor," *IEEE Trans. Ind. Appl*., vol.50, no.3, pp.1801-1808, May-June 2014

[49] M. Barcaro and N. Bianchi, "Torque ripple reduction in fractional-slot interior PM machines optimizing the flux-barrier geometries," in *Proc. ICEM*, pp. 1496–1502, Sep. 2012

[50] T. M. Jahns and W. L. Soong, "Pulsating torque minimization techniques for permanent magnet ac motor drives—A review," *IEEE Trans. Ind. Electron.,* vol. 43, no. 2, pp. 321–330, Apr. 1996

[51] N. Bianchi, S. Bolognani, D. Bon, and M. Dai Pre, "Rotor flux-barrier design for torque ripple reduction in synchronous reluctance and PMassisted synchronous reluctance motors," *IEEE Trans. Ind. Appl*., vol. 45, no. 3, pp. 921–928, May/Jun. 2009

[52] M. Sanada, K. Hiramoto, S. Morimoto, and Y. Takeda, "Torque ripple improvement for synchronous reluctance motor using an asymmetric flux barrier arrangement," *IEEE Trans. Ind. Appl.*, vol. 40, no. 4, pp. 1076–1082, Jul./Aug. 2004

[53] C. Bianchini, F. Immovilli, E. Lorenzani, A. Bellini, and M. Davoli, "Review of Design Solutions for Internal Permanent-Magnet Machines Cogging Torque Reduction", *IEEE Trans. Magn*., pp. 2685 – 2693, vol. 48, issue. 10, Oct. 2012

[54] D. Wang, X. Wang, Y. Yang and R. Zhang, "Optimization of magnetic pole shifting to reduce cogging torque in solid-rotor permanentmagnet synchronous motors," *IEEE Trans. Magn.*, vol. 46, no. 5, pp. 1228–1234, May 2010.

[55] S. Ooi, S. Morimoto, M. Sanada and Y. Inoue, "Performance Evaluation of a High-Power-Density PMASynRM With Ferrite Magnets", *IEEE Trans. Ind. Appl.*, pp. 1308 – 1315, vol. 49, issue. 3, May-June 2013

[56] J.R. Hendershot and T. J. E. Miller, Design of Brushless Permanent-Magnet Motors, (1994), Oxford Magna Physics.